MANY-BODY EFFECTS IN SELECTED TWO-DIMENSIONAL SYSTEMS

A THESIS
SUBMITTED TO THE DEPARTMENT OF PHYSICS
AND THE INSTITUTE OF ENGINEERING AND SCIENCE
OF BILKENT UNIVERSITY
IN PARTIAL FULFILLMENT OF THE REQUIREMENTS
FOR THE DEGREE OF
DOCTOR OF PHILOSOPHY

By

A. Levent Subaşı

August 2009

I certify that I have read this thesis and that in my opinion it is fully adequate, in scope and in quality, as a dissertation for the degree of doctor of philosophy.

Prof. Bilal Tanatar (Supervisor)

I certify that I have read this thesis and that in my opinion it is fully adequate, in scope and in quality, as a dissertation for the degree of doctor of philosophy.

Assoc. Prof. M. Özgür Oktel

I certify that I have read this thesis and that in my opinion it is fully adequate, in scope and in quality, as a dissertation for the degree of doctor of philosophy.

Assoc. Prof. Hatice Kökten

I certify that I have read this thesis and that in my opinion it is fully adequate, in scope and in quality, as a dissertation for the degree of doctor of philosophy.

Asst. Prof. Pierbiagio Pieri

I certify that I have read this thesis and that in my opinion it is fully adequate, in scope and in quality, as a dissertation for the degree of doctor of philosophy.

Assoc. Prof. Azer Kerimov

Approved for the Institute of Engineering and Science:

Prof. Mehmet Baray,
Director of Institute of Engineering and Science

Abstract

MANY-BODY EFFECTS IN SELECTED TWO-DIMENSIONAL SYSTEMS

A. Levent Subaşı
PhD in Physics
Supervisor: Prof. Bilal Tanatar
August 2009

In this thesis we study many-body effects in three distinct two-dimensional systems. The two dimensional electron gas is a model system yielding to basic analytical and computational theoretical ideas of many-body physics and at the same time allows faithful experimental realizations. In connection to the recently observed metal-insulator transition in this system, the spin susceptibility is a relevant observable. The behavior of the spin polarization in a parallel magnetic field is studied using a parametrized ground-state energy expression from accurate quantum Monte Carlo simulations and compared with approximate theories. The critical field to fully polarize the system is calculated. A qualitative difference for the ferromagnetic transition is found for an interval of density values. Next, we consider exciton condensation in an electron-hole bilayer system with density imbalance. Electrons and holes attracting via Coulomb interaction pair up to form spatially separated excitons and condense at low temperatures. Using mean-field theory we establish the phase diagram at zero temperature for different electron and hole densities by comparing the energy of the normal phase with that of the condensed phase. In the last chapter, the two-dimensional Bose-Fermi

atomic gas mixture which is composed of a condensed boson component and a spin polarized Fermi component at zero temperature is studied. Confinement in the third direction affects the density profiles and can induce collapse of the mixture and spatial separation of components.

Keywords: Two-dimensional electron gas, spin polarization, electron-hole bilayer, exciton condensation, population imbalance, two dimensional Bose-Fermi mixture, collapse, demixing

Özet

İKİ BOYUTLU SEÇİLMİŞ SİSTEMLERDE ÇOK PARÇACIK ETKİLERİ

A. Levent Subaşı
Fizik Doktora
Tez Yöneticisi: Prof. Bilal Tanatar
Ağustos 2009

Bu tezde iki boyutlu üç değişik sistemde çok parçacık etkileri incelenmiştir. Hem kuramsal çok parçacık fiziği çalışmaları hem de deneysel uygulamalar açısından iki boyutlu elektron gazı halen yoğun ilgi gören bir model sistemdir. Yakın zamanda gözlemlenen metal-yalıtkan faz geçişi spin duygunluğu ile bağlantılıdır. Giriş bölümünden sonra paralel manyetik alan altında spin polarizasyonu incelendi. Sistemi polarize etmek için gerekli kritik manyetik alan hesaplandı. Yaklaşık teorilerden farklı olarak kuvantum Monte Carlo simulasyonu sonucu elde edilen temel durum enerjisini kullanarak ferromanyetik duruma geçişin bazı yoğunluk dereceleri için ikinci dereceden olduğu gözlendi. İkinci olarak elektron ve deşik katmanlarında, elekron ve deşik yoğunluklarının farklı olduğu durumlarda, egziton yoğuşması çalışıldı. Ortalama alan teorisi kullanarak egziton yoğuşmasının sıfır sıcaklıkta temel durum olduğu elektron ve deşik yoğunlukları hesaplandı. Yoğunluk düzlemindeki faz diyagramı oluşturuldu. Son kısımda ultra-soğuk atomik gaz sistemlerinde iki boyutlu Bose-Fermi atomik gaz karışımları incelendi. Ortalama alan teorisi kullanılarak üçüncü

boyuttaki sıkıştırmanın boson ve fermiyon bileşenlerin yoğunluk dağılımı çalışıldı, etkileşimlere bağlı olarak karışımda ayrışma ve çöküş gözlendi.

Anahtar sözcükler: İki boyutlu elektron gazı, spin polarizasyonu, elektron-deşik çift-katmanı, egziton yoğuşması, yoğunluk farkı, iki boyutlu Bose-Fermi karışımı, çöküş, ayrışma

Acknowledgement

My time as a graduate student at Bilkent University Physics Deparment has been a period of inanition and eventual isolation. I thank everyone who tried to make a difference.

Contents

List of Figures

List of Tables

Chapter 1

Introduction

The homogeneous electron gas [1] is a model system often used in condensed matter physics to study the behavior of delocalized electrons. At zero temperature, the system is characterized by the electron density. This basic model has been extensively studied over the years to understand the correlated motion of electrons. It widely serves as an input to density functional theory based calculations within the local density approximation. The two-dimensional electron gas plays an important role in modeling confined electron and hole systems realized at interfaces of semiconductor based hetero-structures and has served as a theoretical model for understanding the many-body nature of this system [2]. These systems still attract a lot of theoretical and experimental interest. More recently, graphene, a single sheet of graphite, has become a major area of research and is another realization for the application of the two-dimensional models.

In a perpendicular magnetic field, the two-dimensional electron gas enters the quantum Hall regime, which is an immense research field by itself [3–5]. Another problem which has attracted a great deal of experimental and theoretical interest is the metal-insulator transition in the two-dimensional electron system which was observed through recent technological developments allowing to realize low density and high mobility samples [6, 7]. Exciton condensation in electron systems provides another area of interesting physics research [8]. In

particular, bilayer systems are promising candidates to observe effects of exciton condensation [9–11].

In this thesis we study two problems connected to the two points mentioned above related to the two dimensional electron gas. The third chapter is related to condensates in two-dimensions as realized in ultra-cold gas systems. The plan of the thesis is as follows.

In Chapter 2 we study the magnetic behavior and in particular the spin magnetization of an interacting two-dimensional electron gas (2DEG) in an in-plane magnetic field. The ground-state energy of the system is constructed using the accurate correlation energy based on the recent quantum Monte Carlo (QMC) simulations as a function of density, spin polarization, and applied magnetic field. The critical magnetic field B_c required to fully spin polarize the system is obtained as a function of the electron density. The spin polarization as a function of the applied field (less than the critical field) for various densities are calculated. When the QMC parametrization is employed, we find that the two-dimensional electron system undergoes a first order phase transition to a ferromagnetic state in the regions $0 < r_s < 7$ and $20 < r_s < 25$, where r_s is the usual density parameter. For $7 < r_s < 20$ our calculations indicate a second order transition unlike approximate theories. We calculate the susceptibility at finite applied field in comparison with the zero-field linear susceptibility which is a quantity of both theoretical and experimental interest in relation to the metal-insulator transition. As another measurable quantity, we calculate the thermodynamic compressibility of a two-dimensional electron system in the presence of the in-plane magnetic field. Inverse compressibility as a function of density shows a kink or jump like behavior (depending on the nature of the transition) in the presence of an applied magnetic field which can be identified as B_c. Our calculations suggest an alternative approach to transport measurements of determining full spin polarization. The contents of this chapter have been partially published in Refs. [12, 13].

We turn our attention to exciton condensation in electron-hole bilayer systems in Chapter 3. Disregarding spin degrees of freedom we study the pairing effects

between a two dimensional electron system separated from a two dimensional hole system by a distance. Each layer density is assumed to be controlled individually. Within mean-field theory we compare energy of the normal state, which is composed of two-dimensional uniform Fermi gas of electrons and holes, with that of the condensed phase where electron and holes are paired or bound in excitons with s-wave pairing. We find that in the case of density imbalance or unequal electron and hole populations, the condensed phases with s-wave pairing, called Sarma phases, have lower energy than the normal phase and are locally stable with bare Coulomb interactions. We discuss the effect of intra-layer interactions on the phase diagram in the density and population polarization plane. Using a simple model of screening we show that certain regions of the phase space become unstable towards an Fulde-Ferrell-Larkin-Ovchinikov (FFLO) type state signalled by a negative superfluid mass density. Together with intra-plane interactions this results in a rich phase diagram in the crossover region between a weakly interacting high density regime and a strongly interacting low density regime. This is a density driven Bardeen-Cooper-Schrieffer (BCS) - Bose-Einstein condensation (BEC) crossover for this system.

In the last chapter we direct our attention to another condensed system of boson-fermion mixture in two-dimensional ultra-cold gas systems. Ultra-cold atomic systems have enjoyed increasing attention after the realization of BEC in 1995. Currently, experimental situation has advanced to control system parameters from trapping to interactions. Such control has made the study of various condensed matter theories, for example through the realization of rotating traps to mimic charged particles in a magnetic fields and optical lattices to create controlled lattice potentials as in crystal materials. At low temperatures quantum properties of these tunable many-body system become observable. Using anisotropic traps or optical lattices, two dimensional systems can be realized. In the last chapter we study the equilibrium properties of boson-fermion mixtures confined in a harmonic pancake-shaped trap at zero temperature using mean-field theory. When the modulus of the s-wave scattering lengths characterizing boson-boson and boson-fermion interactions are comparable to

the mixture thickness, two-dimensional scattering events introduce a logarithmic dependence on density in the coupling constants, greatly modifying the density profiles themselves. We show that for the case of a negative boson-fermion three-dimensional s-wave scattering length, the dimensional crossover stabilizes the mixture against collapse and drives it towards spatial demixing. The main results of this chapter have recently been published in Ref. [14].

Chapter 2

Magnetization of an Interacting Two-Dimensional Electron Gas

2.1 Introduction

The ground-state properties of the two-dimensional electron gas (2DEG) model are important not only for their technological implications but also from the point of view of many-body physics [1, 2]. In the last decade there has been a huge amount of activity on the transport and thermodynamic properties of low density 2DEG systems largely motivated by the observed metal-insulator transition [6, 7]. In these investigations, mostly transport measurements are performed on low density, high quality samples where the electron-electron interaction effects are dominant. In a complementary way, there are a few thermodynamic measurements on the ground state properties of 2D electron systems such as magnetization (or spin susceptibility) and compressibility. It is of importance to have a consistent picture emerging from these measurements of different nature.

The spin susceptibility of a 2DEG is of interest and many experimental studies are reported[15–24] on Si-MOSFET and GaAs based 2D electron systems.

Experiments with in-plane magnetic field have focused on the spin susceptibility, Landé g-factor, and effective mass of the 2D electron systems present

in Si-MOSFETS and GaAs quantum-well structures [15, 17, 19–21, 25–27]. Thermodynamic measurements of magnetization of a dilute 2D electron system were reported by Prus *et al.*[26], Shashkin *et al.*[27], and Kravchenko *et al.*[28] While the measurements of Prus *et al.*[26] have not found any indication toward a ferromagnetic instability, Shashkin *et al.*[27] observed diverging behavior in spin susceptibility χ_s at a critical density coinciding with the metal-insulator transition determined from transport measurements. Irrespective of the material details the spin susceptibility is found to be enhanced with decreasing carrier density [29].

In a recent paper Zhang and Das Sarma[30] challenged the interpretation of most spin susceptibility measurements by studying the spin polarization effects in a 2DEG in the presence of an applied magnetic field. The paramagnetic to ferromagnetic transition in electron systems has long been of interest[31–35] and the recent experiments have revived further theoretical activity[30, 36–40] including a study on Dirac fermions in graphene [41, 42]. Effects of an in plane magnetic field in graphene showing a second order transition to fully spin polarized state have also been considered recently [43].

Another thermodynamic quantity, the compressibility κ, has also been measured[44–47] using the capacitance technique originated by Eisenstein *et al.* [48]. The initial results[44, 45] suggested that $1/\kappa$ has a minimum at the metal-insulator transition density. More recent measurements[47] revealed the importance of the role played by charged impurities in leading to a minimum in $1/\kappa$.

On the theoretical side, the ground-state energy of the 2DEG is most reliably assessed from quantum Monte Carlo (QMC) simulations [49, 50]. In particular, the recent simulations predict a paramagnetic to ferromagnetic transition before the eventual crystallization of electrons and provide an accurate correlation energy in parametrized form. This allows the calculation of other thermodynamic quantities of interest without resorting to perturbation theory approaches. Experimental observation of spontaneous spin polarization of a 2DEG has been reported by Ghosh *et al.*[51] and Winkler *et al.*[52]. Recent spectroscopic

measurements on the spin polarization in dilute semimagnetic quantum wells also shed some light on the exchange-correlation effects in 2D electron systems [53].

Motivated by the recent experiments on 2DEG systems with an in-plane magnetic field and the associated measurements of thermodynamic quantities, we revisit the calculation of spin polarization effects taking advantage of the recent QMC simulation results[50] which provide an accurate correlation energy with density and spin polarization dependence. As the QMC simulations are performed for a strictly 2DEG system at zero temperature, $T = 0$, we consider a similar system ignoring the finite width of quantum well structure. Thus, coupling of the magnetic field to the orbital motion does not enter the picture. Because we do not include any valley degeneracy effects, our calculations should be more appropriate for GaAs based electron and hole systems. The effects of finite width and disorder, treated perturbatively, on the spin susceptibility of a 2DEG have recently been considered by De Palo *et al.* [54].

In particular, we calculate the spin polarization and the compressibility of a clean 2D electron gas in the presence of an in-plane magnetic field. Our calculations making use of the accurate exchange-correlation energy provided by QMC simulations suggest that the thermodynamic compressibility will exhibit a distinguishing signature of the full spin polarization. Comparing our results with those of previous perturbation theory based calculations we find qualitative as well as quantitative differences for spin susceptibility. We propose that compressibility measurements may allow to discern the critical field and density at which the full spin polarization occurs. Such experiments should be amenable with current technology and could offer an independent way of probing magnetic properties of 2D systems.

The rest of this chapter is organized as follows. First we provide the ground-state energy expression as a function of electron density, spin-polarization parameter, and applied magnetic field, and outline our calculation of the critical field at full spin polarization. Then we present our numerical results of spin polarization and compare them with other theoretical approaches. Finally, we discuss the behavior of the compressibility in the presence of the parallel magnetic

field and the effect of the onset of full spin polarization.

2.2 Model and Theory

We consider a 2D electron gas interacting via the $1/r$ Coulomb potential, embedded in a neutralizing background. This is the two dimensional jellium model. At zero temperature the system is characterized by two dimensionless quantities, The Wigner-Seitz radius r_s and spin polarization ζ.

The Wigner-Seitz radius r_s is defined in terms of the density n and the effective Bohr radius a_B^* by

$$n = \frac{1}{\pi(a_B^* r_s)^2} \tag{2.1}$$

gives the average distance between the electrons in units of a_B^* (Bohr radius includes the band mass of electrons and the background dielectric constant of the host semiconducting material).

The spin polarization is the ratio of the number of excess electron spins to the total number of electrons given by

$$\zeta = \frac{|n_\uparrow - n_\downarrow|}{n} \tag{2.2}$$

and can take values between zero and one, $0 \leq \xi \leq 1$. In the former case the system is said to be unpolarized and one talks about a paramagnetic state whereas in the latter case, the system is fully polarized and is called ferromagnetic.

The system is described by the following Hamiltonian

$$H = \sum_{i=1}^{N} \frac{\hat{\mathbf{p}}_i^2}{2m} + \frac{1}{2} \sum_{i \neq j} \frac{e^2}{\epsilon |\mathbf{r}_i - \mathbf{r}_j|} \tag{2.3}$$

The ratio of the average interaction energy V and the average kinetic energy K is proportional to r_s as easily seen from the following estimates.

$$K \sim E_F \sim k_F^2 \sim n \sim 1/r_s^2$$

$$V \sim e^2/a \sim e^2\sqrt{n} \sim 1/r_s$$

where E_F is the Fermi energy and a is the average distance between electrons. Thus small r_s values characterize high density and weakly interacting systems and large r_s values characterize low density and strongly interacting systems. The parameter r_s is also called the coupling constant.

The total energy per particle in the absence of any external potential and fields can be written in terms of the parameters r_s and ζ as

$$\frac{E_{tot}}{N} = E = E_k(r_s, \zeta) + E_x(r_s, \zeta) + E_c(r_s, \zeta) \tag{2.4}$$

where

$$E_k(r_s, \zeta) = \frac{1 + \zeta^2}{r_s^2} \tag{2.5}$$

is the kinetic energy per particle,

$$E_x(r_s, \zeta) = -\frac{4\sqrt{2}}{3\pi r_s}\left[(1+\zeta)^{3/2} + (1-\zeta)^{3/2}\right] \tag{2.6}$$

is the exchange energy in units of effective Rydberg. (i.e. $\mathrm{Ryd}^* = \hbar^2/(2m^* {a_B^*}^2) = e^2/2\varepsilon a_B^* = E_F r_s^2/2$ where E_F is the Fermi energy of the unpolarized system). These two terms constitute the Hartree-Fock (HF) approximation. The remaining part of the total energy is called the correlation energy E_c which has been the subject of many theoretical calculations. The most accurate results for $E_c(r_s, \zeta)$ are provided by QMC simulations [50, 55, 56].

2.3 2DEG in Parallel B-field

When an in-plane magnetic field is applied to the 2DEG system, the interaction of the magnetic field with the spin of the electrons gives rise to Zeeman energy

$$E_Z(\zeta, B) = -\frac{g}{2}\mu_B \zeta B \tag{2.7}$$

(per particle) where g is the effective band g-factor and μ_B is the effective Bohr magneton and B is the magnetic field strength. The application of an external field therefore changes the magnetic properties of the system. Incidentally, as the magnetic field strength is increased, the system becomes fully spin polarized at a certain value of the magnetic field.

2.4 Non-Interacting System

Let us first report the behavior of compressibility and magnetization for the non-interacting electron system which is obtained by disregarding the Coulomb interaction. The Hamiltonian of the non-interacting system is the kinetic energy term plus the Zeeman term when there is an external field. The ground state of non-interacting electrons in the absence on an external field consists of two equal Fermi seas of spin-up and spin-down electrons. Thus the non-interacting system at zero field is unpolarized.

We are interested in two response functions which are measurable quantities. For purposes of comparison and later convenience we report the non-interacting values of the compressibility (fractional change in volume with pressure) and magnetic susceptibility (derivative of magnetization with respect to magnetic field).

The chemical potential of the unpolarized system is equal to the Fermi energy which is proportional to the density in two dimensions. Therefore the inverse compressibility

$$\frac{1}{\kappa} = -V\frac{\partial P}{\partial V} = n^2\frac{\partial \mu}{\partial n} \tag{2.8}$$

is proportional to the square of the density for the unpolarized non-interacting system. In units of effective Rydberg

$$\frac{1}{\kappa_0} = 2\pi n^2 a_B^2. \tag{2.9}$$

When an in-plane magnetic field is applied, in addition to the kinetic energy there is also the Zeeman energy due to the coupling of the electron spin to the magnetic field and the total energy per particle becomes now a function of r_s, ζ and the applied field strength B.

$$E_0(r_s, \zeta, B) = \frac{1+\zeta^2}{r_s^2} - \frac{g\mu_B}{2}B\zeta \tag{2.10}$$

The total energy for a non-interacting system with respect to the spin polarization ζ is a parabola, the minimum of which is a local minimum for small B (less than

the critical field) and occurs at ζ_0^*

$$\frac{2\zeta_0^*}{r_s^2} = \frac{g\mu_B}{2}B. \tag{2.11}$$

The *critical field* B_{0c}, at which the system becomes fully spin polarized, for a non-interacting system is found by setting $\zeta^* = 1$ above

$$B_{0c} = \frac{4}{g\mu_B r_s^2} = \frac{2}{g}\frac{E_F}{\mu_B} \tag{2.12}$$

at which the local minimum occurs at $\xi^* = 1$. For higher fields the minimum is always at $\xi^* = 1$. The total energy of the noninteracting system is illustrated in Fig. 2.1 at a density corresponding to $r_s = 5$ for various values of the magnetic field. As the magnetic field is increased the minimum of the energy moves continuously from zero to unity. The qualitative behavior of the energy is independent of the density. Unlike the interacting case there is no transition to a partially or fully polarized state as the density is changed.

From the dependence of spin polarization ζ^* on the magnetic field B, we can obtain the response of the system, i.e. the rate of change of polarization with the applied field. The magnetic susceptibility (which is only due to spin here) of the system is defined as

$$\chi = \frac{\partial M}{\partial B} = n\frac{g\mu_B}{2}\frac{\partial \zeta^*}{\partial B} \tag{2.13}$$

where $M = (g\mu_B/2)n\zeta$ is the magnetization and ζ^* is the optimum value of spin polarization which minimizes the energy at given applied field B and density n. Since ζ^* depends linearly on B, the susceptibility of the non-interacting system depends only on density

$$\chi_0 = \frac{(g\mu_B/2)^2}{\epsilon_F}n \tag{2.14}$$

The magnetization of the non-interacting electron gas is called Pauli paramagnetism and the value of the resulting susceptibility is called the Pauli susceptibility.

It is common to look at susceptibility and compressibility normalized by their values for the non-interacting system. In this way the explicit density dependence cancels when the ratio of interacting to non-interacting value is formed. The ratio

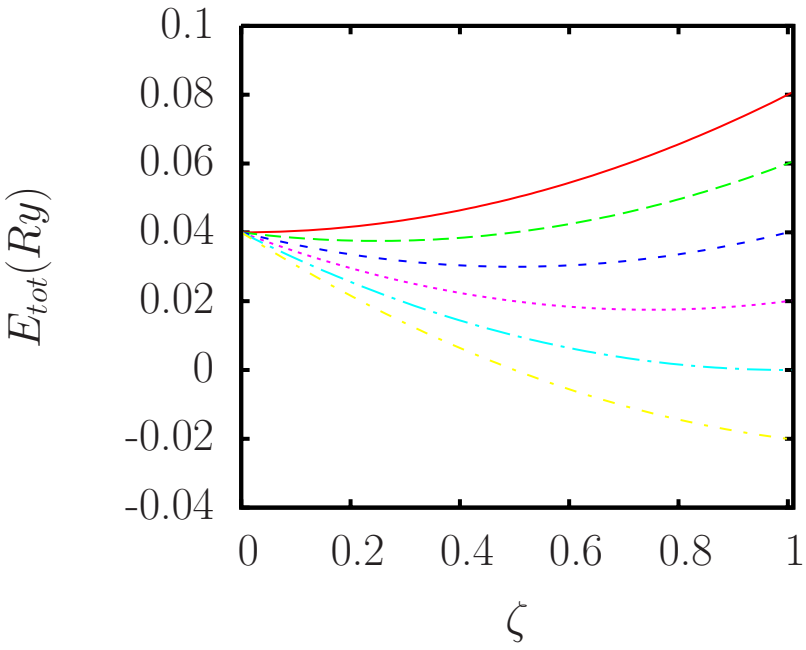

Figure 2.1: (color online) Non-interacting ground-state energy as a function of spin polarization ζ at $r_s = 5$ for various applied magnetic field values (from top to bottom, $B = 0$, $0.25\,B_{0c}$, $0.5\,B_{0c}$, $0.75\,B_{0c}$, B_{0c}, and $1.25\,B_{0c}$).

of the magnetic susceptibility of the interacting to non-interacting system is equal to the ratio of the spin susceptibilities.

2.5 Interacting System

The total energy per particle in the presence of an in-plane applied magnetic field B can be written in terms of the variables r_s, ζ, and B as

$$E(r_s, \zeta, B) = E_k(r_s, \zeta) + E_x(r_s, \zeta) + E_c(r_s, \zeta) + E_Z(\zeta, B) \tag{2.15}$$

For the correlation energy E_c we use two models. The first one is given by the following parametrized expression from QMC calculations of Attaccalite *et al.*[50]

$$E_c(r_s, \zeta) = (e^{-\beta r_s} - 1)\epsilon_x^{(6)}(r_s, \zeta) + \alpha_0(r_s) + \alpha_1(r_s)\zeta^2 + \alpha_2(r_s)\zeta^4\,, \tag{2.16}$$

where

$$\epsilon_x^{(6)}(r_s,\zeta) = E_x(r_s,\zeta) - \left(1 + \frac{3}{8}\zeta^2 + \frac{3}{128}\zeta^4\right) E_x(r_s,0)\,, \tag{2.17}$$

and

$$\alpha_i(r_s) = A_i + (B_i r_s + C_i r_s^2 + D_i r_s^3)\,\ln\left(1 + \frac{1}{E_i r_s + F_i r_s^{3/2} + G_i r_s^2 + H_i r_s^3}\right)\,. \tag{2.18}$$

The constants $A_i, .., H_i$ in the functions α_i $(i = 0, 1, 2)$ are given in tabulated form by Attaccalite *et al* [50] which we reproduce here for completeness.

	$i=0$	$i=1$	$i=2$
A_i	-0.1925^*	0.117331^*	0.0234188^*
B_i	0.0863136^*	-3.394×10^{-2}	-0.037093^*
C_i	0.0572384	$-7.66765\times10^{-3*}$	0.0163618^*
D_i	$-A_0\,H_0$	$-A_1\,H_1$	$-A_2\,H_2$
E_i	1.0022	0.4133	1.424301
F_i	-0.02069	0^*	0^*
G_i	0.33997	6.68467×10^{-2}	0^*
H_i	1.747×10^{-2}	7.799×10^{-4}	1.163099
β	1.3386		

Table 2.1: Optimal fit parameters for the correlation energy, as parametrized in Eqs. (2.16) and (2.18). Values labelled with * are obtained from exact conditions. Table reproduced from Gori-Giorgi *et al* [57].

As a second model for the correlation energy we use the "polarization function"

$$p(r_s,\zeta) = \frac{E_c(r_s,\zeta) - E_c(r_s,0)}{E_c(r_s,1) - E_c(r_s,0)} = \frac{\zeta_+^{\alpha(r_s)} - \zeta_-^{\alpha(r_s)} - 2}{2^{\alpha(r_s)} - 2} \tag{2.19}$$

introduced by Perrot and Dharma-wardana [36] within the classical-map hypernetted-chain (CHNC) approximation calculations. Here $\zeta_\pm = 1 \pm \zeta$, $\alpha(r_s) = C_1 - C_2/r_s + C_3/r_s^{2/3} - C_4/r_s^{1/3}$ is a fitting function and the coefficients C_i $(i = 1, 4)$ are 1.54039, 0.0305441, 0.296208, and 0.239047, respectively [36]. We use the above polarization function expression imposing the $E_c(r_s, 0)$ and $E_c(r_s, 1)$ values

from Attaccalite *et al.*[50] simulations. This may appear somewhat *ad hoc*, but it allows us to perform calculations in the r_s range of interest providing qualitatively different results than the QMC parametrization.

Finally, the last term is the Zeeman energy where g is the Landé g-factor and μ_B is the Bohr magneton. In the numerical calculations material parameters (e.g. appropriate for GaAs semiconductor structures) are absorbed in the effective Bohr radius and the energy unit of effective Rydberg. Therefore the only input is r_s, ζ and the magnetic field B which can be calculated either in terms of the critical value B_{0c} or the corresponding energy in terms of effective Rydberg. In the absence of an external magnetic field ($B = 0$) the recent QMC simulations predict spontaneous transition from a paramagnetic state to ferromagnetic state around $r_s \approx 25$. Unlike the situation[58] in 3D, to the accuracy of simulation results there is no partially polarized phase for the entire range of densities. However, when an external magnetic field is applied it becomes possible to polarize the system partially, and as the magnetic field strength is further increased, the system becomes fully polarized at a critical value of the magnetic field. In the case of interacting particles, assuming the energy has only one local minimum as a function of ζ, we proceed in the same way as for the non-interacting system to find the critical field. The optimum polarization ζ^* is again found by minimizing the total energy. The resulting polarization $\zeta^*(r_s, B)$ now a function of r_s and applied magnetic field, when set equal to unity yields the critical field B_c which can be written as

$$\frac{B_c}{B_{0c}} = 1 - \frac{2}{\pi} r_s + \frac{9\sqrt{2} - 8}{\pi} \left(e^{-\beta r_s} - 1\right) r_s + (\alpha_1 + 2\alpha_2) r_s^2 \,. \tag{2.20}$$

In the above expression the first two terms on the right hand side give the Hartree-Fock approximation (HFA) for the critical field, and the remaining terms follow from the parametrized form of the correlation energy E_c from the QMC simulation. A similar expression for B_c is obtained when we use the parametrization from CHNC calculations

$$\frac{B_c}{B_{0c}} = 1 - \frac{2}{\pi} r_s + \frac{r_s}{2} \frac{\alpha(r_s) 2^{\alpha(r_s)-1}}{2^{\alpha(r_s)} - 2} [E_c(r_s, 1) - E_c(r_s, 0)] \,. \tag{2.21}$$

The above calculation assumes that a local minimum of total energy at the critical field B_c occurs at $\zeta^* = 1$. However, this is not always the case as a number of previous works based on the random-phase approximation (RPA) have already shown [30–32, 39]. If the minimum occurs at $\zeta^* = 1$ the above formulas are valid and spin polarization approaches unity continuously yielding a second order transition to the fully polarized state. As will be discussed in detail later, for some values of r_s the form of the energy curve is fundamentally different from that of the non-interacting case. At the critical field B_c, the total energy as a function of polarization has two minima. One of them is at $\zeta^* = 1$ and the other one is at $0 < \zeta^* < 1$. Since just beyond the critical field the global minimum occurs at $\zeta^* = 1$, there is a discrete jump in the spin polarization and the transition is first order.

2.6 Critical Magnetic Field B_c

We now present our results based on the above constructed ground-state energy of a 2DEG with an in-plane magnetic field. We have calculated the minimum of the ground-state energy with respect to spin polarization for various values of r_s and B. The search for the critical field employed here is purely numerical and is an incremental search. The magnetic field is increased until the minimum of the energy occurs at $\zeta = 1$.

To find the spin polarization of the 2D electron system $\zeta^*(r_s, B)$ at a given magnetic field and density, we minimize the total energy $E(r_s, \zeta, B)$ in Eq. (1), with respect to ζ. Setting $\zeta^* = 1$ allows us to determine the critical magnetic field $B_c(r_s)$ necessary to fully spin polarize the system.

In Fig. 2.2 we show the critical magnetic field B_c in units of B_{c0} as a function of r_s for various theoretical models. $B_{c0} = 2E_F/g\mu_B$ is the critical field for a non-interacting system. When the QMC correlation energy is used in the total ground state energy expression, B_c vanishes around $r_s \approx 25$ indicating the fact that the system spontaneously magnetizes at this density according to the QMC results [50]. When the CHNC form for the correlation energy is employed

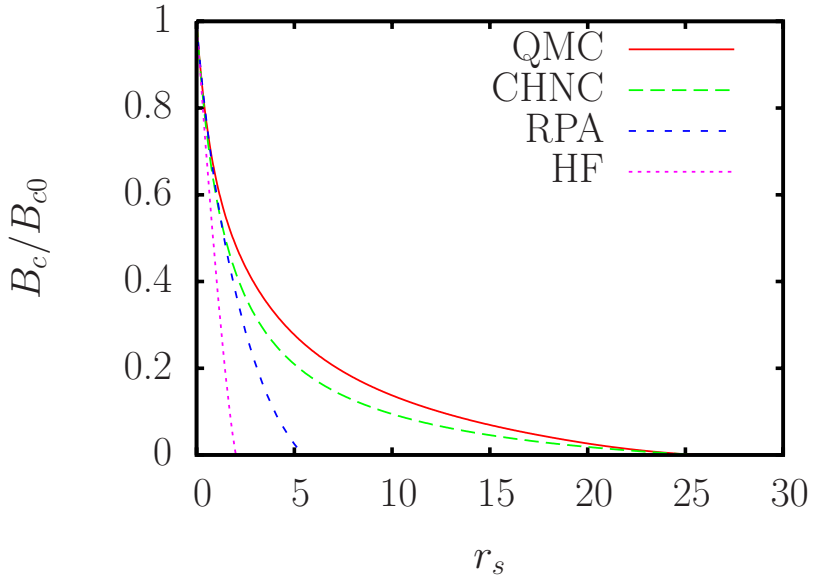

Figure 2.2: (color online) The critical field B_c to fully polarize the 2DEG as a function of r_s in various approximations, Hartree-Fock (dotted line), RPA (dashed line), correlation energy from CHNC approximation (long dashed line), and QMC correlation energy (solid line).

we obtain a similar $B_c(r_s)$ curve with some deviations in the intermediate r_s region. Other theoretical approaches such as Hartree-Fock (HF) and random-phase approximation (RPA) yield qualitatively similar but quantitatively very different results. For instance, B_c vanishes around $r_s \approx 2$ and $r_s \approx 5.5$ in HF and RPA, respectively [30]. At points above each curve in the r_s-B plane the system is fully polarized in the corresponding model.

The total energy curves at increasing magnetic field as a function of the spin polarization at three representative values of r_s are illustrated in Fig. 2.3. In this figure, the left panel displays the results using QMC correlation energy of Attaccalite *et al.* [50]. At zero field the minimum of the total energy is at $\zeta = 0$ for $r_s \lesssim 25.5$. As the magnetic field is increased the minimum shifts to nonzero values of ζ. For instance, at $r_s = 2$ and $r_s = 25$ the total energy has two minima when the field reaches the critical value B_c at the corresponding density

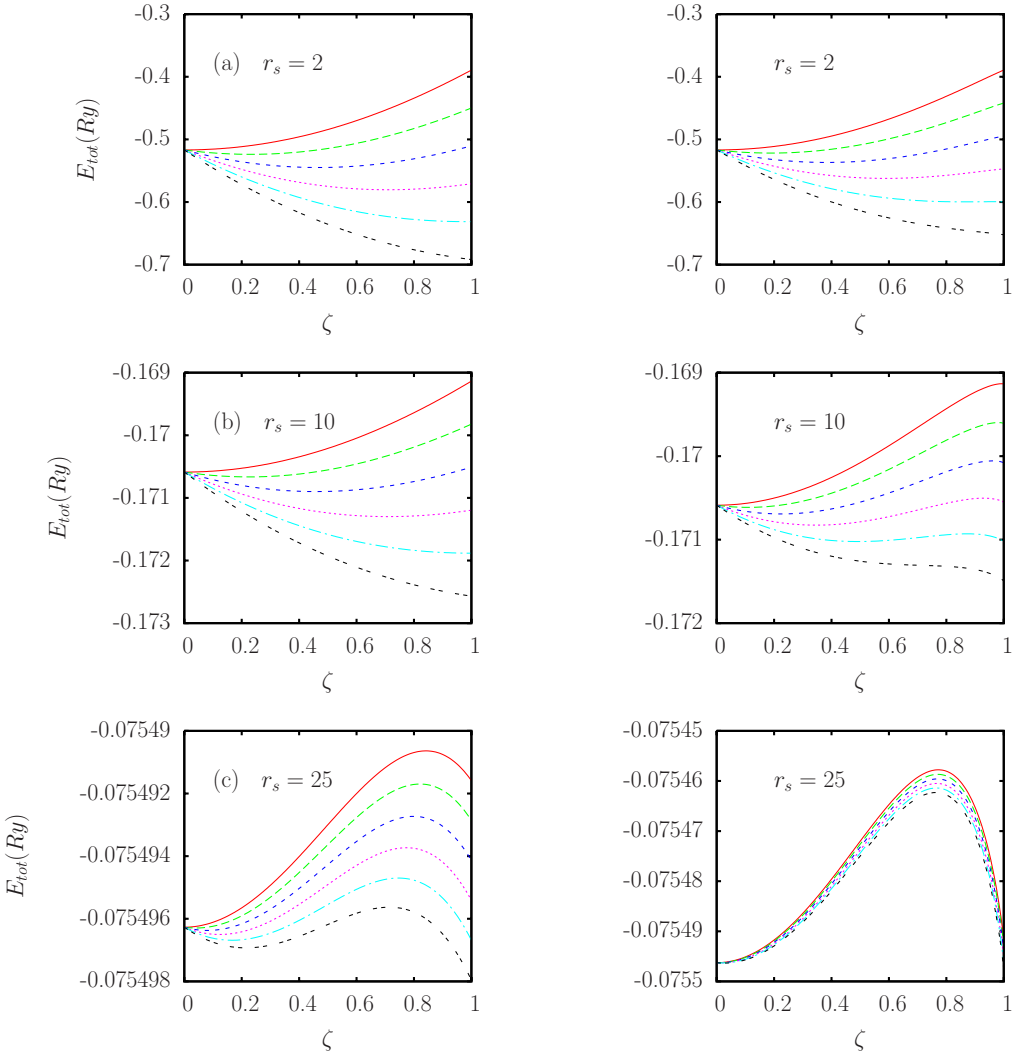

Figure 2.3: (color online) Ground-state energy as a function of spin polarization ζ at $r_s = 2$, 10, and 25, for various applied magnetic field values (from top to bottom, $B = 0$, $0.25\,B_c$, $0.5\,B_c$, $0.75\,B_c$, B_c, and $1.25\,B_c$). Left panel uses QMC based correlation energy, right panel shows correlation energy from CHNC approximation.

(for $r_s = 2$ the local minimum and the minimum at $\zeta = 1$ are very close and not visible on this scale). Above B_c the energy has one minimum at the end point $\zeta = 1$, there is an abrupt change in ζ at B_c. For $r_s = 10$, on the other hand, we find that the local minimum moves to the right as the field increases but continuously goes to $\zeta = 1$ at B_c. In the right panel, the results using the CHNC approach are shown. In this case, we always have two minima at B_c.

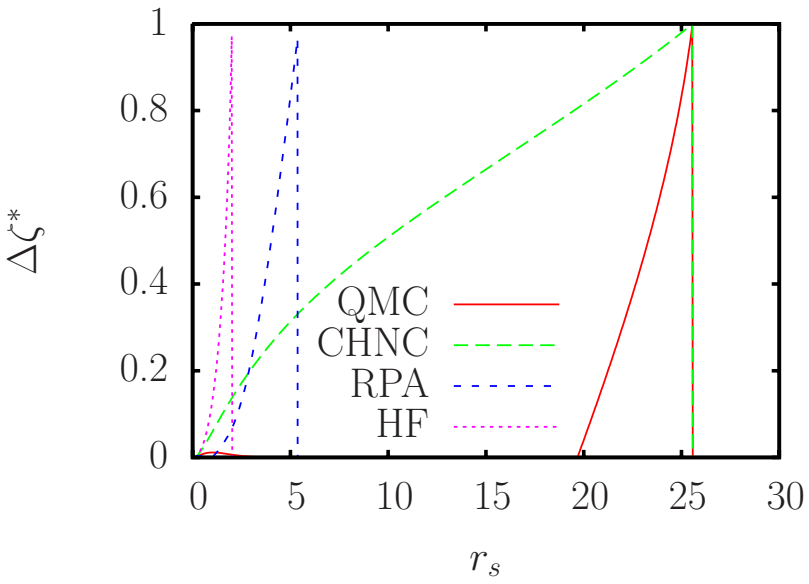

Figure 2.4: (color online) The discontinuous jump in spin polarization $\Delta\zeta^*$ at B_c as a function of r_s. Dotted, dashed, long dashed and solid lines represent HFA, RPA, CHNC, and QMC correlation energy, respectively.

The jump in the spin polarization at the critical field B_c denoted by $\Delta\zeta^*$ describes the nature of the transition to the fully polarized state and is shown in Fig. 2.4. For the QMC correlation energy in the ranges $0 < r_s < 7$ and $20 < r_s < 25$ we find that there is a finite jump in polarization which is equal to the distance between the two minima of energy. The transition to the polarized state is first order when $\Delta\zeta^* \neq 0$. Such a phase transition is known as Bloch ferromagnetism. For intermediate values of r_s we find that the

polarization becomes unity continuously as the magnetic field is increased. In this region the phase transition to the ferromagnetic state using the QMC correlation energy appears to be of Stoner type (i.e., second order). In contrast, approximate theories such as HFA and RPA yield a finite $\Delta\zeta^*$ in the whole range of r_s regions of their applicability.

The qualitatively different behavior found for $7 < r_s < 20$ implying a continuous phase transition to the ferromagnetic state is a direct result of our use of the parametrized QMC correlation energy. It is known that the energy differences between the polarized states are diminishingly small. Thus, the results of our calculations are limited by the accuracy of the parametrized QMC expression. The small jump in polarization for $0 < r_s < 7$ is intriguing. To further check the robustness of this prediction we have calculated $\Delta\zeta^*$ within the CHNC correlation energy and we have also used the correlation energy expression recently proposed by Chesi and Giuliani [59]. Input from the CHNC correlation energy yields $\Delta\zeta^*$ which is qualitatively similar to that found in HFA and RPA. In the work of Chesi and Giuliani differences from QMC results in spin polarized energies are reported. Although the Gell-Mann-Bruckner type calculation of Chesi and Giuliani[59] is only valid for $r_s \to 0$, we have found that a small nonzero $\Delta\zeta^*$ up to $r_s \approx 1$. Thus, it appears that for small r_s there is a weak first order transition to the ferromagnetic state.

2.7 Susceptibility and Compressibility

In the following we use the QMC correlation energy to calculate various physical quantities. The spin polarization ζ^* that minimizes the ground-state energy is shown in Fig. 2.5 as a function of B-field at fixed density and as a function of r_s at constant B. In Fig. 2.5(a), when ζ^* becomes unity at B_c with a jump, $\Delta\zeta^* > 0$ is consistent with the results presented in Fig. 2.4. As $\Delta\zeta^* = 0$ for $7 < r_s < 20$, we find that $\zeta^*(B)$ curves approach unity smoothly in this region. In Fig. 2.5(b) we show ζ^* as a function of r_s at the constant magnetic field values of $B_c(r_s = 5)$, $B_c(r_s = 15)$, and $B_c(r_s = 23)$ which are the critical field strengths

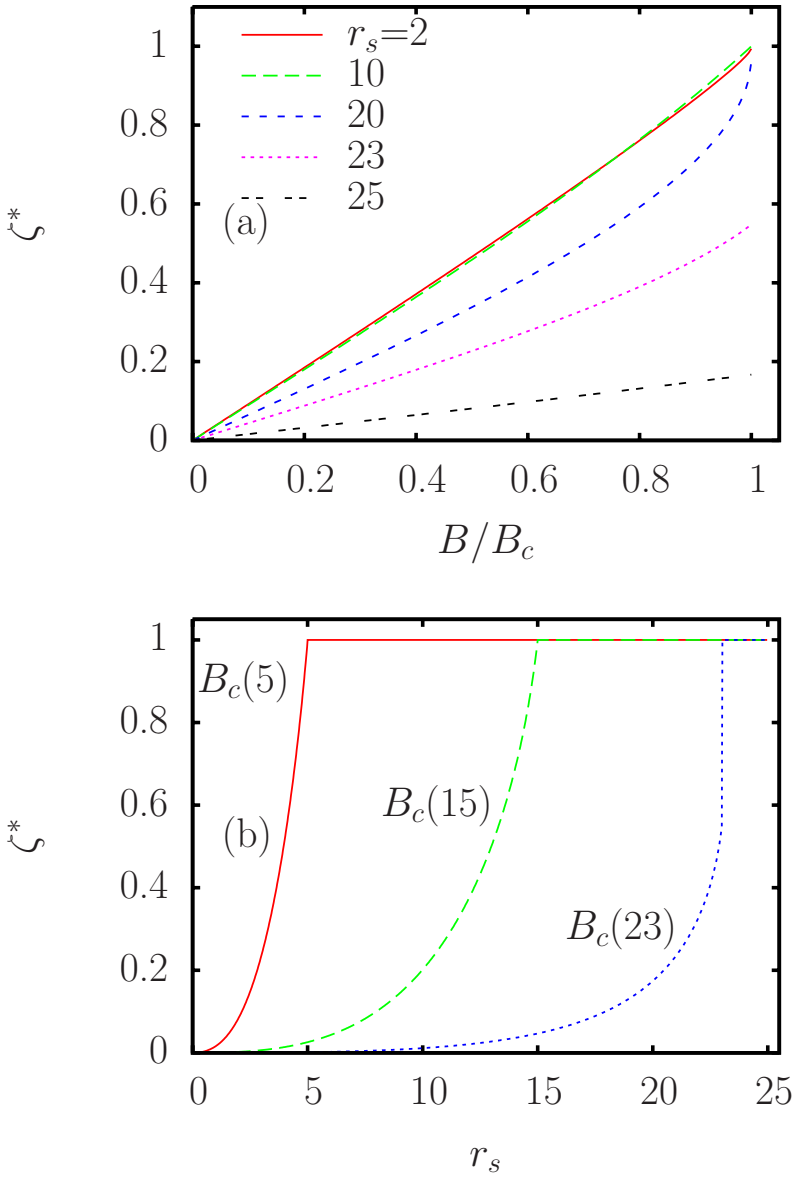

Figure 2.5: (color online) Spin polarization ζ^* (the value of ζ which minimizes the ground-state energy at a given magnetic field) as a function of (a) the B-field for several r_s values and (b) as a function of r_s for several B-field values. Solid, dashed, and dotted lines indicate $B = B_c(r_s = 5)$, $B = B_c(r_s = 10)$, and $B = B_c(r_s = 20)$, respectively.

fully polarization the system at $r_s = 5, 15$ and 23, respectively. Thus the plotted curves exhibit the onset of full spin polarization as the density is decreased. Note also that nonzero values of $\Delta\zeta^*$ consistent with those shown in Fig. 2.4 are clearly visible. The behavior of ζ^* found with CHNC correlation is qualitatively similar to the HF and RPA results.

Another quantity of interest which can be accessed experimentally is the magnetic susceptibility of the system defined as $\chi = n(g\mu_B/2)\partial\zeta^*/\partial B$. It is common practice to look at the susceptibility normalized by its value χ_0 for the non-interacting system (Pauli susceptibility), i.e. $\chi_0 = n\mu_B^2/\epsilon_F$, so that the ratio $\chi/\chi_0 = (g\epsilon_F/2\mu_B)\,\partial\zeta^*/\partial B$ is formed. Using the analytic expressions for the various terms of the ground-state energy, we find

$$\frac{\chi}{\chi_0} = \frac{2}{r_s^2}\left[\frac{2}{r_s^2} - \frac{\sqrt{2}}{\pi r_s}\left[(1+\zeta^*)^{-1/2} + (1-\zeta^*)^{-1/2}\right] + \left.\frac{\partial^2 E_c}{\partial\zeta^2}\right|_{\zeta^*}\right]^{-1}. \qquad (2.22)$$

Hence the spin polarization $\zeta^*(r_s, B)$ for a given density and magnetic field can be related to the spin susceptibility. Thus, once having obtained ζ^* numerically, we can readily calculate the susceptibility. This is shown in Fig 2.6(a) and Fig 2.6(b) at five different values of density. The values for small field indicate the enhancement of the susceptibility over the non-interacting value as density is lowered. The deviation from a horizontal line is a measure of the deviance from the linear behavior which is more significant for large r_s and near full polarization.

The zero-field (linear) susceptibility has been calculated by Attaccalite *et al.* [50]. On the other hand, the spin-susceptibility at finite B (nonlinear susceptibility) should be quantitatively different from calculations based on perturbation theory (HFA, RPA). The strong dependence on r_s at finite fields is already evident in the magnetization curves of $\zeta^*(B)$ shown in Fig 2.5.

Zhang and Das Sarma[30] pointed out that spin-susceptibility measured by magnetoresistance experiments[15–20, 22, 23] through the polarization field B_c does not coincide either with the linear or the nonlinear spin-susceptibility, casting some doubt on the interpretation of experiments. The spin-susceptibility is extracted from the measured B_c that is related to a model dependence of $\zeta^*(B)$

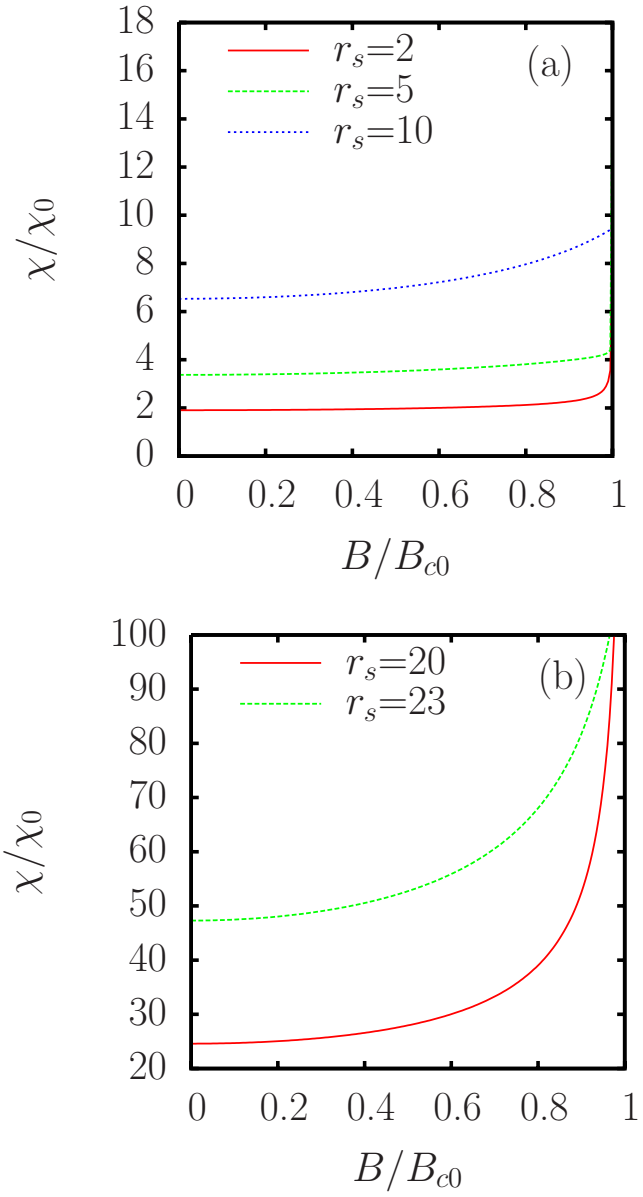

Figure 2.6: Spin susceptibility normalized by its non-interacting value χ/χ_0 for several r_s values as a function of the magnetic field B.

which is typically linear. If the QMC parametrization gives a correct description with $\Delta\zeta^* \approx 0$ for a range of r_s values, the assumption about the slope of ζ^* vs. B appears to be reasonable. This coincides with the region $0 < r_s < 20$. In fact, since most experiments[19–24] are performed at $r_s \lesssim 10$ experimental procedure seems to be valid. However, when $\Delta\zeta^* > 0$ as in the case large r_s region or as in the case of CHNC description, then the experimental error would be considerable.

We also mention the recently reported thermodynamic measurements by Kravchenko *et al.*[28] of the magnetization in a 2DEG. Spin-susceptibility obtained by such measurements should provide an independent check of the same quantity from transport measurements.

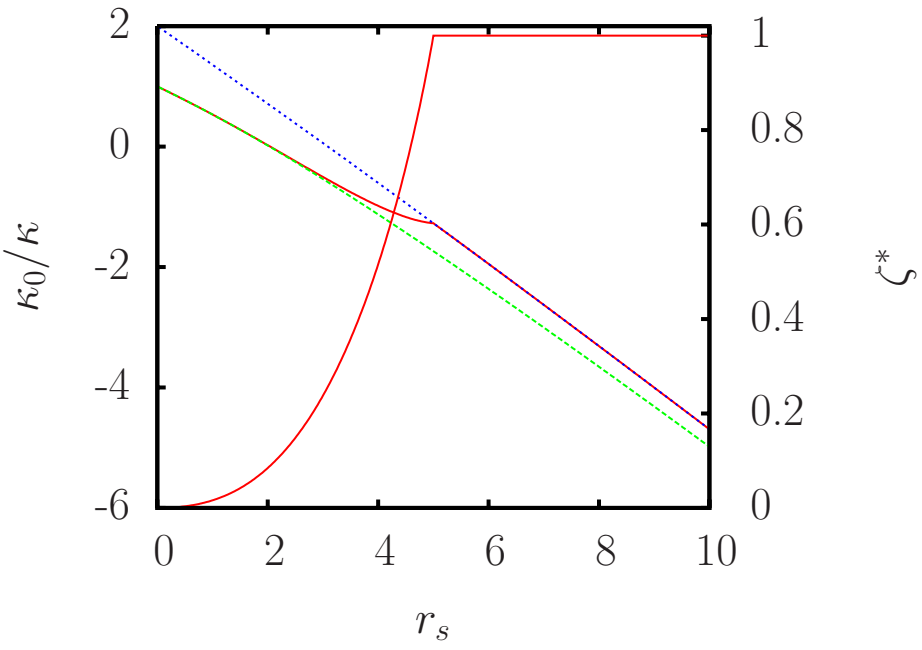

Figure 2.7: The scaled inverse compressibility κ_0/κ as a function of r_s. The upper and lower dotted lines indicate unpolarized and fully polarized results, respectively, in the absence of magnetic field. The intermediate result is at $B = B_c(r_s = 5)$. In this figure, the QMC correlation energy is used. The onset of full polarization is marked by the kink in the inverse compressibility curve.

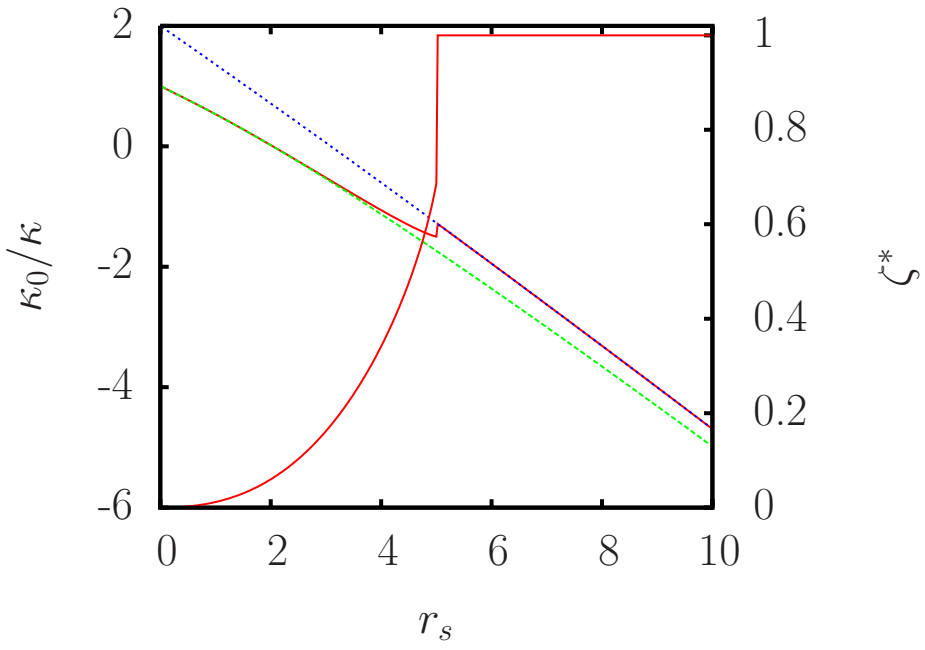

Figure 2.8: The scaled inverse compressibility κ_0/κ as a function of r_s. The upper and lower dotted lines indicate unpolarized and fully polarized results, respectively, in the absence of magnetic field. The intermediate result is at $B = B_c(r_s = 5)$. In this figure, the CHNC correlation energy is used. The onset of full polarization is marked by the jump in the inverse compressibility curve.

A related quantity of interest, thermodynamic compressibility, also yields interesting features when the 2DEG is subjected to an in-plane magnetic field and whose magnetic field dependence attracted less attention. Using the QMC and CHNC ground state energy we calculate the density dependence of thermodynamic compressibility

$$\frac{1}{\kappa} = -\frac{nr_s}{4}\left[\frac{\partial E}{\partial r_s} - r_s\frac{\partial^2 E}{\partial r_s^2}\right], \tag{2.23}$$

which is shown in Fig. 2.7. More specifically, we plot the inverse compressibility scaled by the non-interacting value of the unpolarized system, κ_0/κ, as a function of r_s, for a 2D electron system under an in-plane magnetic field. The inverse compressibility for the non-interacting system is given by $1/\kappa_0 = 2n/r_s^2$. We

chose the external field to be equal to $B_c(r_s = 5)$, namely the critical field to fully spin polarize the system at $r_s = 5$. We observe that the inverse compressibility at a constant magnetic field switches to its fully polarized system value with a kink like behavior. This suggests that in the compressibility measurements similar to those performed recently[44–47] the effects of polarizing magnetic field could be discernible. Thus, an alternative thermodynamic method to the transport measurements of determining B_c may be provided by compressibility measurements with in-plane magnetic field. Interestingly, the kink-like behavior in compressibility is more visible at smaller r_s, since the difference between the ground-state energies of the polarized and unpolarized phases decrease with increasing r_s. On the other hand, for larger r_s where our model predicts a strong first order transition, the signature of the onset of full spin polarization could, in principle, become stronger. The kink behavior is replaced by a discontinuity in compressibility due to the sudden jump in polarization. The jump in compressibility has also been discussed within the Fermi liquid theory description for a 2DEG near the point of full polarization [60]. However, since the energy differences get very small at larger r_s the jump and even the crossover becomes less visible. The CHNC approximation has this effect visible at $r_s = 5$ which is shown in Fig 2.8. It would be interesting to perform experiments similar to those reported by Dultz and Jiang[45], Rahimi *et al.*[46] and Allison *et al.*[47] in parallel magnetic fields to observe the predicted signature of full spin polarization.

Another quantity of interest indicating the full spin polarization is provided by the thermodynamic relation $\partial M/\partial n = -\partial\mu/\partial B$. Integrating over the electron density n allows for the calculation of spin-susceptibility. We show in Fig. 2.9 $\partial\mu/\partial B$ as a function of r_s at three different magnetic field values. The onset of full spin polarization is readily identified as a sharp peak at the critical r_s value for respective magnetic fields. This quantity has already been measured by Kravchenko *et al.*[28] for Si-MOSFETs. Our calculations which are more appropriate for single-valley systems such GaAs suggest that qualitatively similar results should follow.

We remark that the inverse compressibility exhibits a minimum and an upturn

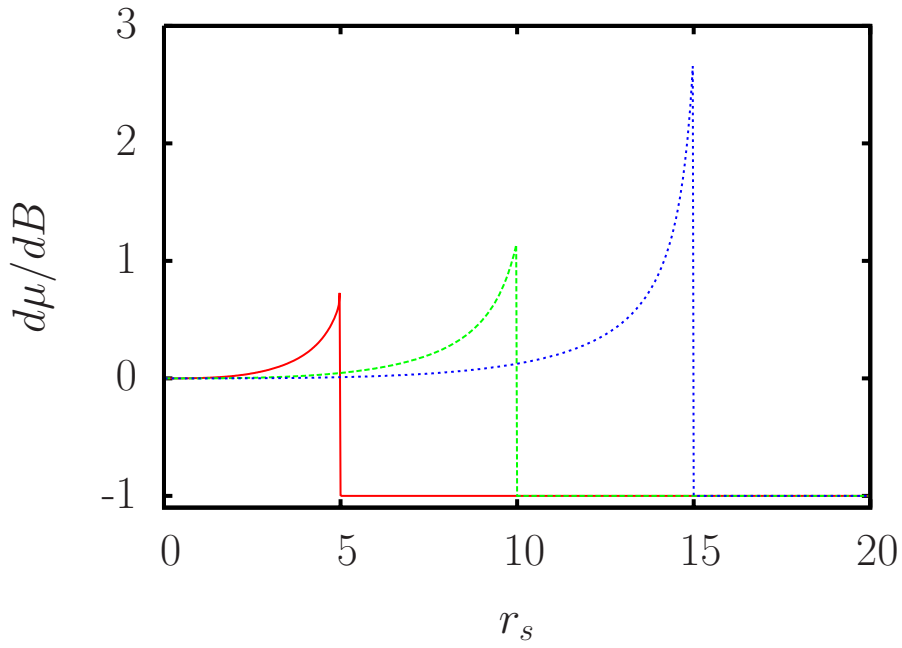

Figure 2.9: $\partial\mu/\partial B$ in units of $g\mu_B/2$ as a function of r_s. The three curves from left to right are for the magnetic field values, $B_c(r_s = 5)$, $B_c(r_s = 10)$, and $B_c(r_s = 15)$, respectively.

at a larger r_s value due to electron-impurity interactions [45, 47]. Therefore the kink-like behavior in κ_0/κ predicted by our calculations could be smeared depending on the level of disorder present in the experimental samples. The experimental samples are of quasi-two-dimensional character, so that for realistic comparison with experiments, the finite width of the quantum wells should be taken into account.

2.8 Summary and Concluding Remarks

We have considered the effect of in-plane magnetic field on the ground-state energy and magnetic properties of a 2DEG for a wide range of densities. To this purpose we have used the recently available QMC simulation based

correlation energy as a function of r_s and ζ. Thus, our calculations should provide quantitatively more accurate results compared to the previously employed approximate methods. Interestingly, from the QMC correlation energy calculations we find that under an externally applied magnetic field the 2D electron system undergoes a first order phase transition to a ferromagnetic state in the range $0 < r_s < 7$ and $20 < r_s < 25$. That is, as the magnetic field is increased from just below B_c to above B_c, the polarization minimizing the total energy ζ^* jumps from a finite intermediate value to unity abruptly. On the other hand, in the range $7 < r_s < 20$, ζ^* reaches unity continuously which suggests a second order phase transition. These findings are in qualitative difference with the predictions of HFA and RPA based calculations[30] which yield a first order phase transition to the ferromagnetic state in the whole range of densities corresponding to $0 < r_s \lesssim 5.5$.

We have provided a simple calculation of in-plane magnetic field dependence of compressibility of a strongly interacting 2D electron gas. The inverse compressibility as a function of r_s exhibits a crossover from the partially polarized to fully polarized state, which should be identifiable experimentally.

There are several directions with which our calculations can be extended. To make better contact with experiments it would be useful to take the finite quantum well width effects into account. This would require a reliable calculation of the exchange and correlation energies as a function of r_s, ζ, and parameters describing the finite width of electron layer, which presently are not available from QMC simulations. Furthermore, disorder effects are also likely to significantly affect the spin-susceptibility and compressibility. It would be interesting to include the disorder effects in a realistic way when a direct comparison to the experiments are made.

Appendix

In the following sections we provide some details of the susceptibility and compressibility calculations. The last section gives order of magnitude estimates for the critical field in GaAs based semiconductor structures.

2.9 Notes on Susceptibility

2.9.1 Non-Interacting Case: Pauli Paramagnetism

The ground state of the non-interacting system is easily found by equating the Fermi levels of spin-up and spin-down electrons since this will minimize the energy.

From the following identities

$$n = 2\frac{\pi k_F^2}{(2\pi)^2} = 2\frac{2m\pi}{(2\pi)^2\hbar^2}\epsilon_F \qquad \text{and} \qquad n_{\uparrow,\downarrow} = \frac{1}{2}(1 \pm \zeta)n \tag{2.24}$$

we have (take $g = 2$ for now)

$$n_{\uparrow,\downarrow} = \frac{1}{4\pi\hbar^2}\left[2m(\epsilon_F \pm \mu_B B)\right]. \tag{2.25}$$

The magnetization when there is an applied field B can be easily calculated as

$$\begin{aligned} M = \mu_B(n_\uparrow - n_\downarrow) &= \frac{2m}{4\pi\hbar^2}\mu_B\left[(\epsilon_F + \mu_B B) - (\epsilon_F - \mu_B B)\right] \\ &= \frac{2m}{4\pi\hbar^2}2\mu_B^2 B = \frac{\mu_B^2}{\epsilon_F}nB \end{aligned} \tag{2.26}$$

and the susceptibility becomes independent of the applied field B

$$\chi_0 = \frac{\partial M}{\partial B} = \lim_{B\to 0}\frac{\partial M}{\partial B} = \lim_{B\to 0}\frac{M}{B} = \frac{\mu_B^2}{\epsilon_F}n \tag{2.27}$$

but depends on density. Note that this can also be derived from the non-interacting energy expression which was stated in Sec. 2.4.

$$\zeta_0^* = \frac{r_s^2}{2Ryd}\mu_B B = \frac{r_s^2}{2}\frac{2ma_B^2}{\hbar^2}\mu_B B = \frac{r_s^2(k_F a_B)^2}{2}\frac{\mu_B}{\epsilon_F}B \tag{2.28}$$

and the susceptibility is found as

$$\chi_0 = \frac{M}{B} = \frac{\mu_B n \zeta_0^*}{B} = \frac{\mu_B^2}{\epsilon_F} n \tag{2.29}$$

as before.

2.9.2 Interacting System

In the case of interacting particles, the optimum polarization ζ^* is again found by setting the derivative of the total energy equal to zero.

$$\left.\frac{\partial E}{\partial \zeta}\right|_{\zeta^*} = 0 \qquad \Rightarrow \qquad \zeta^* = \zeta^*(r_s, B) \tag{2.30}$$

Put $\zeta^* = 1$ above to obtain the critical field as a function of density.

$$\zeta^*(r_s, B) = 1 \qquad \Rightarrow \qquad B_c = B_c(r_s) \tag{2.31}$$

We would like to write down an expression for the critical field. Differentiating the total energy

$$E = E_k + E_x + E_c + E_Z \tag{2.32}$$

with respect to ζ and assuming that the derivative vanishes at the minimum for which the polarization is denoted by ζ^* we have,

$$\left.\frac{\partial E}{\partial \zeta}\right|_{\zeta^*} = 0 = \frac{2}{r_s^2} - \frac{4\sqrt{2}}{3\pi r_s}\frac{3}{2}\left[(1+\zeta)^{1/2} - (1-\zeta)^{1/2}\right] + \left.\frac{\partial E_c}{\partial \zeta}\right|_{\zeta^*} - \frac{g\mu_B}{2}B. \tag{2.33}$$

When $\zeta^* = 1$, $B = B_c$, thus

$$\frac{B_c}{B_{0c}} = 1 - \frac{2}{\pi} r_s + \frac{r_s^2}{2} \left.\frac{\partial E_c}{\partial \zeta}\right|_{\zeta=1}. \tag{2.34}$$

Finally, we need the following derivatives to obtain the expression for the critical field.

$$\frac{\partial E_c}{\partial \zeta} = \left(e^{-\beta r_s} - 1\right) \frac{\partial \epsilon_x^{(6)}}{\partial \zeta} + 2\alpha_1 \zeta + 4\alpha_2 \zeta^3 \tag{2.35}$$

$$\frac{\partial \epsilon_x^{(6)}}{\partial \zeta} = -\frac{4\sqrt{2}}{3\pi r_s}\frac{3}{2}\left(\sqrt{1+\zeta} - \sqrt{1-\zeta}\right) + \frac{4\sqrt{2}}{3\pi r_s}\left(\frac{3}{2}\zeta + \frac{3}{16}\zeta^3\right) \tag{2.36}$$

The above expression evaluated at $\zeta = 1$ becomes

$$\left.\frac{\partial E_c}{\partial \zeta}\right|_{\zeta=1} = \left(e^{-\beta r_s} - 1\right) \frac{-4\sqrt{2}}{3\pi r_s} \left(\frac{3\sqrt{2}}{2} + \frac{3}{2} + \frac{3}{16}\right) + 2\alpha_1 + 4\alpha_2 \tag{2.37}$$

and we have

$$\frac{B_c}{B_{0c}} = 1 - \frac{2}{\pi} r_s + \frac{9\sqrt{2} - 8}{\pi} \left(e^{-\beta r_s} - 1\right) r_s + (\alpha_1 + 2\alpha_2) r_s^2 \tag{2.38}$$

This method assumes that the minimum of energy is a local minimum and the derivative at the minimum vanishes.

From the definition of magnetic susceptibility

$$\chi = \frac{\partial M}{\partial B} = \mu_B n \frac{\partial \zeta^*}{\partial B} \tag{2.39}$$

and its value for the non-interacting system at the same density

$$\chi_0 = \frac{\mu_B^2}{\epsilon_F} n \tag{2.40}$$

we form the ratio

$$\frac{\chi}{\chi_0} = \frac{\epsilon_F}{\mu_B} \frac{\partial \zeta^*}{\partial B} \tag{2.41}$$

which does not depend on density explicitly. Now, we scale the magnetic field B by its corresponding critical value at a given density to obtain

$$\frac{\chi}{\chi_0} = \frac{\epsilon_F}{\mu_B B_{0c}} \frac{\partial \zeta^*}{\partial (B/B_{0c})} = \frac{\partial \zeta^*}{\partial \widetilde{B}} \tag{2.42}$$

where $\widetilde{B} = B/B_{0c}$. This expression is suitable for numerical calculation.

The spin susceptibility is only meaningful when the applied magnetic field B is less than the critical field B_c. But for $B < B_c$, we know that the minimum of the energy as a function of polarization ζ is a local minimum, and then it is justified to find the optimum value ζ^* which minimizes the energy by setting the derivative equal to zero.

$$\left.\frac{\partial E}{\partial \zeta}\right|_{\zeta^*} = 0 \qquad \Rightarrow \qquad \zeta^* = \zeta^*(r_s, B) \tag{2.43}$$

$$\left.\frac{\partial E}{\partial \zeta}\right|_{\zeta^*} = 0 = \frac{2\zeta^*}{r_s^2} - \frac{2\sqrt{2}}{\pi r_s}\left[(1+\zeta^*)^{1/2} - (1-\zeta^*)^{1/2}\right] + \left.\frac{\partial E_c}{\partial \zeta}\right|_{\zeta^*} - \frac{\mu_B B}{(e^2/2a_B)} \quad (2.44)$$

Differentiating the last equation with respect to B

$$0 = \frac{2}{r_s^2}\frac{\partial \zeta^*}{\partial B} - \frac{\sqrt{2}}{\pi r_s}\left[(1+\zeta^*)^{-1/2} + (1-\zeta^*)^{-1/2}\right]\frac{\partial \zeta^*}{\partial B} + \left.\frac{\partial^2 E_c}{\partial \zeta^2}\right|_{\zeta^*}\frac{\partial \zeta^*}{\partial B} - \frac{\mu_B}{(e^2/2a_B)} \quad (2.45)$$

which after solving for $\partial\zeta^*/\partial B$ becomes

$$\frac{\partial \zeta^*}{\partial B} = \frac{\mu_B}{(e^2/2a_B)}\left[\frac{2}{r_s^2} - \frac{\sqrt{2}}{\pi r_s}\left[(1+\zeta^*)^{-1/2} + (1-\zeta^*)^{-1/2}\right]\left.\frac{\partial^2 E_c}{\partial \zeta^2}\right|_{\zeta^*}\right]^{-1} \quad (2.46)$$

and we find

$$\begin{aligned}\frac{\chi}{\chi_0} &= \frac{\epsilon_F}{(e^2/2a_B)}\left[\frac{2}{r_s^2} - \frac{\sqrt{2}}{\pi r_s}\left[(1+\zeta^*)^{-1/2} + (1-\zeta^*)^{-1/2}\right] + \left.\frac{\partial^2 E_c}{\partial \zeta^2}\right|_{\zeta^*}\right]^{-1} \\ &= 2/r_s^2\left[\frac{2}{r_s^2} - \frac{\sqrt{2}}{\pi r_s}\left[(1+\zeta^*)^{-1/2} + (1-\zeta^*)^{-1/2}\right] + \left.\frac{\partial^2 E_c}{\partial \zeta^2}\right|_{\zeta^*}\right]^{-1}\end{aligned} \quad (2.47)$$

Thus once having obtained ζ^* numerically, we have an analytical expression for the normalized susceptibilty.

2.9.3 Onset of Full Spin Polarization

Kravchenko *et al.* recently report measurements of the quantity $d\mu/dB$ [28]. This quantity is related to dM/dn by a Maxwell relation. The free energy F as a function of the particle number N and magnetic field B at fixed chemical potential μ, volume V and magnetization M obeys

$$dF = \mu dN - VMdB \quad (2.48)$$

and equating mixed partial derivatives with respect to N and B, one finds

$$\begin{aligned}\frac{\partial^2 F}{\partial B \partial N} &= \frac{\partial^2 F}{\partial N \partial B} \\ \frac{\partial \mu}{\partial B} &= -V\frac{\partial M}{\partial N} \\ -\frac{\partial \mu}{\partial B} &= \frac{\partial M}{\partial n}.\end{aligned} \quad (2.49)$$

Hence, upon integration magnetization M can be obtained. The magnetization obtained in this way is given in [28]. The onset of full polarization corresponds to the flat part of this quantity vs. density parameter r_s plot as shown in Fig. 2.9.

The magnetization curves at fixed magnetic field B as a function of density to compare general behavior with the recent experiment which is shown in Fig. 2.5(b). As the density is decreased the system becomes fully polarized. This is another way of looking at the critical field vs. r_s curve in Fig. 2.2, namely as a plot of critical density characterized by the onset of full spin polarization as a function of magnetic field.

The onset of full spin polarization at finite external field B as the density decreases manifests itself in the compressibilty curve as a function of density with a kink or a discontinuity depending on the correlation energy involved. (see Fig. 2.7 and Fig. 2.8) This can provide another experimental way to determine the critical field B_c.

2.10 Notes on Compressibility

The compressibility is another measurable property of the system defined as

$$\kappa = -\frac{1}{V}\frac{\partial V}{\partial P} \tag{2.50}$$

in term of the area V and pressure P. Consider the differential free energy

$$dF = -S\mathrm{d}T - P\mathrm{d}V + \mu\mathrm{d}N \tag{2.51}$$

as a function of the thermodynamic quantities temperature T, area V and number of particles N. S, P and μ denote the entropy, the pressure and the chemical potential, respectively. From second mixed derivatives we obtain the following Maxwell relation

$$\begin{aligned} \frac{\partial}{\partial N}\frac{\partial F}{\partial V} &= \frac{\partial}{\partial V}\frac{\partial F}{\partial N} \\ -\frac{\partial P}{\partial N} &= \frac{\partial \mu}{\partial V} \end{aligned} \tag{2.52}$$

which can be written as

$$\begin{aligned} -\frac{\partial P}{\partial N} &= \frac{\partial \mu}{\partial V} \\ -\frac{\partial P}{\partial V}\frac{\partial V}{\partial N} &= \frac{\partial \mu}{\partial N}\frac{\partial N}{\partial V} \\ -V\frac{\partial P}{\partial V} &= V\left(\frac{\partial N}{\partial V}\right)^2\frac{\partial \mu}{\partial N} \\ -V\frac{\partial P}{\partial V} &= \frac{N^2}{V}\frac{\partial \mu}{\partial N} \end{aligned} \tag{2.53}$$

where we used the relation $N = nV$ and V represents the area in a two dimensional system. The inverse compressibility can then be calculated as

$$\frac{1}{\kappa} = \frac{N^2}{V}\frac{\partial \mu}{\partial N} \tag{2.54}$$

and $\partial\mu/\partial n$ is related to the derivatives of the total energy with respect to the density n or the parameter r_s.

The compressibilty of the interacting system can be plotted using its non-interacting value as the unit which is calculated below.

$$\mu = \frac{\partial E_{tot}}{\partial N} = \frac{\partial}{\partial n}(nE) = E + n\frac{\partial r_s}{\partial n}\frac{\partial E}{\partial r_s} \tag{2.55}$$

and

$$\frac{\partial \mu}{\partial n} = \frac{\partial r_s}{\partial n}\left[\frac{\partial E}{\partial r_s} - \frac{1}{2}\frac{\partial}{\partial r_s}\left(r_s\frac{\partial E}{\partial r_s}\right)\right] = -\frac{1}{4}(\pi a_B^2)r_s^3\left[\frac{\partial E}{\partial r_s} - r_s\frac{\partial^2 E}{\partial r_s^2}\right] \tag{2.56}$$

For the non-interacting system this quantity is calculated using

$$E = \frac{1}{r_s^2} \qquad \frac{\partial E}{\partial r_s} = -\frac{2}{r_s^3} \quad \frac{\partial^2 E}{\partial r_s^2} = \frac{6}{r_s^4} \tag{2.57}$$

to be

$$\frac{\partial \mu_0}{\partial n} = 2\pi a_B^2. \tag{2.58}$$

We find the following relations.

$$\frac{\kappa_0}{\kappa} = \frac{1}{2\pi a_B^2}\frac{\partial \mu}{\partial n} \qquad \text{and} \qquad \frac{\kappa}{\kappa_0} = \frac{2\pi a_B^2}{\partial \mu/\partial n}. \tag{2.59}$$

2.11 Estimates

Here we estimate some physical quantities for GaAs based samples in terms of order of magnitude. In this section we use SI units.

The Bohr radius of the electron is found from

$$\frac{\hbar^2}{2ma_B^2} = \frac{1}{2}e^2 4\pi\varepsilon_0 a_B \Rightarrow a_B = \frac{4\pi\varepsilon_0\hbar^2}{me^2} \approx 0.53\,\text{Å} \tag{2.60}$$

which is given for vacuum. In a material, we replace the bare mass m with an effective carrier mass m^* and use permittivity ε of the specific material instead of the permittivity of vacuum ε_0.

$$a_B^* = \frac{4\pi\varepsilon\hbar^2}{m^*e^2} = \frac{\kappa}{\widetilde{m^*}}a_B \tag{2.61}$$

where $\kappa = \varepsilon/\varepsilon_0$ is the dielectric constant and $\widetilde{m^*} = m^*/m$ is the effective mass in terms of the bare mass.

Using the material parameters the Wigner-Seitz radius r_s can be calculated as

$$\begin{aligned} r_s &= \left(\frac{1}{\pi(a_B^*)^2 n}\right)^{1/2} \\ &= \left(\frac{\widetilde{m^*}^2}{\pi\kappa^2 a_B^2 n}\right)^{1/2} \\ &\approx \frac{\widetilde{m^*}}{\kappa}\left(\frac{1}{\pi(0.53\times 10^{-8}\text{cm})^2 n}\right)^{1/2} \\ r_s &\approx \frac{\widetilde{m^*}}{\kappa}\frac{10^3}{\sqrt{n}} \end{aligned} \tag{2.62}$$

where n is given in $10^{-10}\,\text{cm}^{-2}$. For GaAs, $\widetilde{m^*} = 0.07$ and $\kappa = 13$. So, given the density n we can use the following formula to estimate r_s

$$r_s \sim \frac{6}{\sqrt{n}} \tag{2.63}$$

Thus, the density range $n = 1.0 - 4.0 \times 10^{-10}\,\text{cm}^{-2}$ roughly corresponds to $3 \leq r_s \leq 6$ in GaAs.

Observe that the effective Bohr radius in the GaAs becomes approximately $\kappa/\widetilde{m^*} = 13/0.07 \sim 200$ times larger than the Bohr radius corresponding to ~ 100 Å.

Similary the effective Rydberg gets multiplied by a factor $\widetilde{m^*}/\kappa^2$.

Next, we estimate the critical field B_c to fully polarize a system at a given density. Since the critical field has the same order of magnitude with its non-interacting value B_{c0} at the same density, we will look at rough estimates of B_{c0} which is given by

$$\begin{aligned} B_{c0} &= \frac{\epsilon_F^*}{g\mu_B/2} = \frac{2}{g\mu_B}\frac{\hbar^2 k_F^2}{2m^*}\frac{2m^* a_B^{*2}}{\hbar^2}\,\mathrm{Ryd}^* \\ &= \frac{2}{g\mu_B}(k_F a_B^*)^2\,\mathrm{Ryd}^* = \frac{2}{g\mu_B}\frac{2}{r_s^2}\,\mathrm{Ryd}^* \end{aligned} \tag{2.64}$$

where the effective Bohr magneton μ_B equals

$$\mu_B = \frac{e\hbar}{2m^*} = 9.274 \times 10^{-24}\,\mathrm{J/T}. \tag{2.65}$$

Using the conversion

$$1\mathrm{J} = 4.59 \times 10^{17}\,\mathrm{Ryd} \tag{2.66}$$

we obtain

$$\begin{aligned} B_{c0} &= \frac{2}{r_s^2}\frac{2}{g}\frac{1}{9.274 \times 10^{-24}\,\mathrm{J/T} \times 4.59 \times 10^{17}\,\mathrm{Ryd/J}}\frac{\widetilde{m^*}}{\kappa^2}\,\mathrm{Ryd} \\ &\approx \frac{4}{r_s^2}\frac{\widetilde{m^*}}{g\kappa^2} 2 \times 10^5\,(\mathrm{T}) \end{aligned} \tag{2.67}$$

For GaAs $g_b = 0.44$ and $g \sim 4g_b$ at $r_s \sim 3$ and we estimate B_c as

$$B_c \sim 10\mathrm{T} \tag{2.68}$$

Chapter 3

Excitonic Condensation in Electron-Hole Bilayers with Density Imbalance

3.1 Introduction

Quantum phenomena become observable on a macroscopic scale for condensed quantum phases. A system of two fermion species displays a crossover behavior between two limits of a condensed phase as the inter-species interaction is varied. When the interactions are strongly attractive the particles can form tightly bound pairs which are bosonic in nature and can thus Bose condense at low temperature. On the other hand when the interaction is weak the fermions can form a Bardeen-Cooper-Schriefer (BCS) state where pairs are weakly bound. The BCS theory, [61] originally developed to explain conventional superconductivity, considers a many-body state of electrons where a spin up electron with momentum $\hbar\mathbf{k}$ is paired with a spin down electron with opposite momentum. It is established that these two limits can be described by the same state. The so called BCS-BEC crossover, which has been suggested 30 years ago [62–64], is of recent experimental and theoretical interest. Pairing of fermions plays the key role in understanding

strongly correlated phenomena and the physics of superfluidity in ultracold atoms, metals, nuclei and neutron stars [65].

Developments in ultra-cold atomic gas experiments with trapped fermionic atoms provides the possibility to study the crossover physics in a system with great experimental control [66–68]. In these systems the interaction, which at the low density and temperatures is essentially a contact interaction, can generally be characterized by the s-wave scattering length. The interaction can be varied using Feshbach resonances via the application of a magnetic field. Recently experiments with population imbalance have also been performed [69–73]. Theoretical studies have shown the possibility to observe exotic quantum states such as Sarma and Fulde-Ferrell-Larkin-Ovchinikov (FFLO) phases in these systems [74–78]. In the Sarma phase pairs have zero center of mass momentum, whereas in the FFLO states pairs carry a net center of mass momentum resulting in a spatially modulated energy gap function.

Electron systems in semiconductor devices provide another possible physical realization where BCS-BEC crossover physics can be observed. Electrons and holes can form bound states called excitons due to the attractive Coulomb interaction between them. Excitons are the composite bosons in this system. The interaction strength can be changed relatively by varying the density. In contrast to ultra-cold atom systems, the Coulomb interaction between the fermions is long-ranged.

Exciton condensation in electron-hole (e-h) systems was predicted more than 40 years ago [79]. Also known as the excitonic insulator [80–82] with gapped charged excitations exciton condensation is a candidate for the BCS-BEC crossover [83, 84]. The electron-hole recombination in the bulk causes small exciton lifetimes and this lead to the proposal of spatially separated electron-hole systems with a thin barrier preventing recombination [85, 86]. The bilayer quantum-well systems realized in semiconductor hetero-structures are thus particularly promising [87–93]. Using electrical and optical techniques exciton condensation has been observed in several different systems. Quantum Hall experiments at half-filling investigate BEC in electron-electron and hole-hole

bilayers [91, 92, 94]. Optically generated bilayer excitons also show evidence for condensation [87, 95]. Recently, excitons coupled to photons to form polaritons with even smaller mass leading to higher condensation temperatures have been studied theoretically [96] and experimentally [97, 98]. Finally electrically generated 2D electron and 2D hole bilayer system provides independent control of the layer densities. Such systems where the interlayer separation is reduced down to one effective Bohr radius have been produced very recently [9–11]. In these systems evidence for increasing electron-hole coupling has been seen in Coulomb drag measurements. These systems where the electron and hole densities can be controlled individually with small enough separation at low enough temperatures (below 1 K) should also be able to see the exotic phases which are studied in this chapter. The case of equal electron and hole densities leading to full pairing has been extensively studied theoretically using the mean-field approach in bilayer systems [99–101].

Recently Pieri *et al.* [102] studied the BCS-BEC crossover with unequal electron and hole densities in an e-h bilayer system neglecting the in-plane Coulomb interactions. The electron and hole densities are controlled independently to create the population imbalance. This is the analog of the situation of superconductor in a magnetic field, which is assumed to couple only to electron spins, and was first studied by Sarma [103]. In that case the spin-up and spin-down electrons are the Fermi species and the magnetic field takes the role of chemical potential difference in the semiconductor system. Here we extend the same mean field approach to include the in-plane interactions. We find that the effect of intra-layer Fock energy quantitatively changes the phase diagram moving the normal-condensed phase boundary to lower densities. We study the effect of screening with a simple model which cures a logarithmic divergence due to the simultaneous presence of the singularity in the Coulomb potential and the presence of a Fermi surface at zero temperature. The local stability of isotropic translationally invariant gapless superfluid states at $T = 0$, which was not seen previously by Pieri *et al.* [102] due to small but finite temperature used in the calculation, is demonstrated. We calculate the energy of the condensed

phase and compare it with that of the normal phase which is the Hartree-Fock energy. In this way we map out the phase diagram in the average density - population polarization plane. We check the local stability of the condensed phase by calculating the superfluid mass density and identify a negative superfluid phase density with an instability towards an FFLO phase. Finally, we study the effect of screening using a simple model based on ground plane screening [104]. The intra-layer interactions and screening effects give rise to a rich phase diagram in the crossover region between the BCS-like high density state and the BEC of low density excitons showing a possibility to observe the phases discussed as the population polarization is changed.

More recently, exciton condensation has been considered theoretically for graphene bilayer. In this system the electrons have linear dispersion at the so called Dirac points of their spectrum. It is being debated whether exciton condensation can be observed in this system [105–108]. It would be interesting to study the effects of pairing in the graphene bilayer system with a linear (instead of quadratic) dispersion relation.

A further motivation for this study is to obtain a wave function which can be used as a starting point in a more sophisticated quantum Monte Carlo simulation. Quantum Monte Carlo simulations provide in principle very accurate ground state energies and have been applied to exciton condensation [109–112] and BCS-BEC crossover problem to provide benchmark results [113–116].

The plan of the chapter is as follows. In the next two sections we give the description of the bilayer system and the mean field approach to study the effects of pairing. The resulting energy gap equations with and without the intra-plane interactions being present are presented next. In Sec. 3.4.2 we discuss the screening model used. Numerical solutions of the gap equations are illustrated for different cases at representative densities in Sec. 3.5. The stability of the solutions is assessed by the superfluid mass density which is given in Sec. 3.8. The ensuing phase diagrams are presented at the end and we conclude with a summary. The details of the derivation of the gap equations, their numerical solution and the analysis of the logarithmic divergence of the derivative of the gap function at the

zero-crossings of the excitation spectrum are discussed in detail in the Sec. 3.11.

3.2 Electron-Hole Bilayer System

The Hamiltonian describing fermions of two different type interacting with a two-body potential can be written in the second quantized form in the following way

$$\begin{aligned}\hat{H} = &\sum_{\mathbf{k}}(\epsilon^a_{\mathbf{k}} a^\dagger_{\mathbf{k}} a_{\mathbf{k}} + \epsilon^b_{\mathbf{k}} b^\dagger_{\mathbf{k}} b_{\mathbf{k}}) + \frac{1}{2V}\sum_{\mathbf{k_1 k_2 q}} U^{aa}_{\mathbf{q}} a^\dagger_{\mathbf{k}_1+\mathbf{q}} a^\dagger_{\mathbf{k}_2-\mathbf{q}} a_{\mathbf{k}_2} a_{\mathbf{k}_1} \\ &+ \frac{1}{2V}\sum_{\mathbf{k_1 k_2 q}} U^{bb}_{\mathbf{q}} b^\dagger_{\mathbf{k}_1+\mathbf{q}} b^\dagger_{\mathbf{k}_2-\mathbf{q}} b_{\mathbf{k}_2} b_{\mathbf{k}_1} + \frac{1}{V}\sum_{\mathbf{k_1 k_2 q}} U^{ab}_{\mathbf{q}} a^\dagger_{\mathbf{k}_1+\mathbf{q}} b^\dagger_{\mathbf{k}_2-\mathbf{q}} b_{\mathbf{k}_2} a_{\mathbf{k}_1}\end{aligned} \tag{3.1}$$

Here, as is common to do for uniform electron gas systems, the basis states chosen for electrons and holes are plane wave states labeled by wave vectors $\mathbf{k}$

$$|\mathbf{k}\rangle = \frac{1}{\sqrt{V}} e^{i\mathbf{k}\cdot\mathbf{r}} \tag{3.2}$$

The operators $a_{\mathbf{k}}/a^\dagger_{\mathbf{k}}$ ($b_{\mathbf{k}}/b^\dagger_{\mathbf{k}}$) are creation/annihilation operators for electrons (holes) respectively. The single particle energies are denoted by $\epsilon^a_{\mathbf{k}}, \epsilon^b_{\mathbf{k}}$ and the matrix element $U_{\mathbf{q}}$ with respect to plane wave states becomes the Fourier transform of the corresponding two body interaction $U(\mathbf{r})$

$$U_{\mathbf{q}} = \int d\mathbf{r} e^{-i\mathbf{q}\cdot\mathbf{r}} U(\mathbf{r}) \tag{3.3}$$

Above U^{aa}, U^{bb} and U^{ab} denote the electron-electron, hole-hole and electron-hole Coulomb interactions, respectively. Finally V, which stands for the volume in general, denotes the area in a two-dimensional system. The explicit form of the Coulomb potentials are

$$U^{aa}_{\mathbf{q}} = \frac{2\pi e^2}{\varepsilon q}\,, \qquad\qquad U^{ab}_{\mathbf{q}} = \frac{2\pi e^2}{\varepsilon q}\mathrm{e}^{-qd}\,. \tag{3.4}$$

Here we consider an electron-hole bilayer system where the electron layer is separated by a distance d from the hole layer both of which have area denoted

by V. This geometry models the realization of 2DEG systems in conventional semiconductor heterostructures.The wave vectors $\mathbf{k}$ are two-dimensional vectors in the plane. We consider that each layer has a uniform neutralizing background, in general separated by a distance from the layer. This results in the cancellation of Hartree terms in the above Hamiltonian. There are no $\mathbf{q} = 0$ terms.[1] Finally we neglect the spin degrees of freedom and consider spinless electrons and holes.

3.3 Mean-Field Description

We study the above Hamiltonian in the mean-field approximation and reduce it to a single particle problem. This can be done replacing $a_{\mathbf{k}}b_{-\mathbf{k}}$ by its ground state expectation value and defining the gap function $\Delta_{\mathbf{k}} = -\sum_{\mathbf{k}'} U^{ab}_{\mathbf{k}\mathbf{k}'} \langle a_{\mathbf{k}'}b_{-\mathbf{k}'}\rangle$ which becomes the order parameter. We obtain the reduced Hamiltonian

$$\hat{H} = \sum_{\mathbf{k}} \epsilon^a_{\mathbf{k}} a^\dagger_{\mathbf{k}} a_{\mathbf{k}} + \epsilon^b_{\mathbf{k}} b^\dagger_{\mathbf{k}} b_{\mathbf{k}} - \sum_{\mathbf{k}} \Delta_{\mathbf{k}} a^\dagger_{\mathbf{k}} b^\dagger_{-\mathbf{k}} + \Delta^*_{\mathbf{k}} b_{-\mathbf{k}} a_{\mathbf{k}} \tag{3.5}$$

This Hamiltonian can be diagonalized by a unitary transformation which is reproduced in Sec. 3.11.

Equivalently we can start with the full Hamiltonian and the following BCS type wave function to capture the same kind of $\mathbf{k}, -\mathbf{k}$ pairing with excess electrons or holes. Bogoluibov operators $\alpha^\dagger_{\mathbf{k}}$ and $\beta^\dagger_{-\mathbf{k}}$ which are linear combinations of electron/hole creation/annihilation operators defined by

$$\alpha_{\mathbf{k}} = u_{\mathbf{k}} a_{\mathbf{k}} - v_{\mathbf{k}} b^\dagger_{-\mathbf{k}} \qquad \beta_{-\mathbf{k}} = u_{\mathbf{k}} b_{-\mathbf{k}} + v_{\mathbf{k}} a^\dagger_{\mathbf{k}} \tag{3.6}$$

$$\alpha^\dagger_{\mathbf{k}} = u^*_{\mathbf{k}} a^\dagger_{\mathbf{k}} - v^*_{\mathbf{k}} b_{-\mathbf{k}} \qquad \beta^\dagger_{-\mathbf{k}} = u^*_{\mathbf{k}} b^\dagger_{-\mathbf{k}} + v^*_{\mathbf{k}} a_{\mathbf{k}} \tag{3.7}$$

create/annihilate properly normalized states with excess quasi-particles orthogonal to $|\Psi\rangle_{BCS}$, which has equal number of electrons and holes. The excited states of BCS theory are states with excess (unpaired) electrons/holes or excited pairs [117]. For example, a state one electron at $\mathbf{q}$ state instead of a ground pair

[1] We neglect remaining field energy of uniformly charged plates which depends on the geometry but gives a constant shift to the energy at fixed densities.

can be written as

$$|\Psi\rangle = \alpha^\dagger_{\mathbf{q}} |\Psi_{BCS}\rangle \tag{3.8}$$

$$= a^\dagger_{\mathbf{q}} \prod_{\mathbf{k}\neq\mathbf{q}} (u_{\mathbf{k}} + v_{\mathbf{k}} a^\dagger_{\mathbf{k}} b^\dagger_{-\mathbf{k}}) |0\rangle \ . \tag{3.9}$$

The form of this wave function is given by the above mean field solution [118, 119]. Generalizing this to a variational form we have

$$|\Psi\rangle = \prod_{\mathbf{k}} (u^p_{\mathbf{k}} + v^+_{\mathbf{k}} \alpha^\dagger_{\mathbf{k}} + v^-_{\mathbf{k}} \beta^\dagger_{-\mathbf{k}})(u_{\mathbf{k}} + v_{\mathbf{k}} a^\dagger_{\mathbf{k}} b^\dagger_{-\mathbf{k}}) |0\rangle \tag{3.10}$$

$$= \prod_{\mathbf{k}} (u^p_{\mathbf{k}} + v^+_{\mathbf{k}} \alpha^\dagger_{\mathbf{k}} + v^-_{\mathbf{k}} \beta^\dagger_{-\mathbf{k}}) |\Psi_{BCS}\rangle \, .$$

We can ensure normalization by choosing $|u_{\mathbf{k}}|^2 + |v_{\mathbf{k}}|^2 = 1$ and $|u^p_{\mathbf{k}}|^2 + |v^+_{\mathbf{k}}|^2 + |v^-_{\mathbf{k}}|^2 = 1$.

We can use this variational wave function as an ansatz for the variational principle with the full Hamiltonian subject to particle number constraints.

The amplitudes squared $|u^p v_{\mathbf{k}}|^2 = |v_{\mathbf{k}}|^2(1 - f^+_{\mathbf{k}} - f^-_{\mathbf{k}})$, $|v^+_{\mathbf{k}}|^2 = f^+_{\mathbf{k}}$, $|v^-_{\mathbf{k}}|^2 = f^-_{\mathbf{k}}$ and $|u^p u_{\mathbf{k}}|^2 = |u_{\mathbf{k}}|^2(1 - f^+_{\mathbf{k}} - f^-_{\mathbf{k}})$ correspond to probabilities of having a pair, a type a particle, a b particle and no particle in the $\mathbf{k}$ quantum state.

This formalism is identical to the finite temperature BCS theory where $f^\pm_{\mathbf{k}}$ are the occupation numbers of quasi-particles. The excited states of BCS theory are involved here to create the population imbalance since the excited states have excess electrons or holes. The lower energy of these states at zero temperature is achieved by lowering the corresponding chemical potential so that the energy of this state becomes lower than the ground pair [117].

The number of particles is not fixed, the average number of a and b particles are controlled by the chemical potentials μ_a and μ_b respectively. The ground state of non-interacting fermions with excess a particles corresponding to two filled Fermi spheres, for example, is obtained by setting $u^p_{\mathbf{k}} v_{\mathbf{k}} = 1$ for $|\mathbf{k}| \leq k_{Fb}$, $v^a_{\mathbf{k}} = 1$ for $k_{Fb} < |\mathbf{k}| \leq k_{Fa}$ and $u^p_{\mathbf{k}} u_{\mathbf{k}} = 1$ otherwise.

In the case of equal populations the above variational function is able to capture the physics of weakly interacting limit as well as the strongly interacting regime and can provide a picture for the crossover physics [63].

3.4 Gap Equations

The solution of the mean-field Hamiltonian is provided by the following coupled integral equations which are commonly known as the energy gap equations. (Sec. 3.11) At zero temperature, $T = 0$, they are

$$\Delta_{\mathbf{k}} = -\frac{1}{V}\sum_{\mathbf{k}'}{}'U^{ab}_{\mathbf{k}\mathbf{k}'}\frac{\Delta_{\mathbf{k}'}}{2E_{\mathbf{k}'}}(1-f^+_{\mathbf{k}'}-f^-_{\mathbf{k}'}) \tag{3.11}$$

$$\xi_{\mathbf{k}} = \epsilon_{\mathbf{k}}-\mu-\frac{1}{2V}\sum_{\mathbf{k}'}{}'U^{aa}_{\mathbf{k}\mathbf{k}'}\left[(1-\xi_{\mathbf{k}'}/E_{\mathbf{k}'})(1-f^+_{\mathbf{k}'}-f^-_{\mathbf{k}'})+f^+_{\mathbf{k}'}+f^-_{\mathbf{k}'}\right] \tag{3.12}$$

$$E^2_{\mathbf{k}} = \xi^2_{\mathbf{k}}+\Delta^2_{\mathbf{k}} \tag{3.13}$$

$$f^{\pm}_{\mathbf{k}} = \begin{cases} 1 \text{ if } E^{\pm}_{\mathbf{k}}<0 & E^{\pm}_{\mathbf{k}} = E_{\mathbf{k}} \pm \Delta E_{\mathbf{k}} \\ 0 \text{ if } E^{\pm}_{\mathbf{k}}>0 & \Delta E_{\mathbf{k}} = \Delta\xi_{\mathbf{k}} + \frac{1}{2V}\sum_{\mathbf{k}'}{}'U^{aa}_{\mathbf{k}\mathbf{k}'}(f^-_{\mathbf{k}'}-f^+_{\mathbf{k}'}) \end{cases} \tag{3.14}$$

where the average and diffence of the single particle energies and chemical potentials are given by

$$\epsilon_{\mathbf{k}} = \frac{1}{2}(\epsilon^a_{\mathbf{k}}+\epsilon^b_{\mathbf{k}}) \qquad \text{and} \qquad \mu = \frac{1}{2}(\mu_a+\mu_b) \tag{3.15}$$

$$\Delta\epsilon_{\mathbf{k}} = \frac{1}{2}(\epsilon^a_{\mathbf{k}}-\epsilon^b_{\mathbf{k}}) \qquad \text{and} \qquad h = \frac{1}{2}(\mu_a-\mu_b) \tag{3.16}$$

$$\Delta\xi_{\mathbf{k}} = \frac{1}{2}(\epsilon^a_{\mathbf{k}}-\mu_a-\epsilon^b_{\mathbf{k}}+\mu_b) = \Delta\epsilon_{\mathbf{k}}-h \tag{3.17}$$

with $\epsilon^i_{\mathbf{k}} = \hbar^2k^2/2m_i$, $i = a, b$. $U^{aa}_{\mathbf{k}}, U^{ab}_{\mathbf{k}}$ are the Fourier transforms of the intra- and inter-layer interactions, respectively. At finite temperature, the occupation functions $f^{\pm}_{\mathbf{k}}$ go from the step function to the Fermi-Dirac distribution.

Given the electron and hole chemical potentails μ_a and μ_b, we solve these equations numerically to obtain the unknown functions $\Delta_{\mathbf{k}}, \xi_{\mathbf{k}}$ and $\Delta E_{\mathbf{k}}$ which is described in detail in Sec. 3.11.

For fixed number of particles the chemical potential values have to be adjusted according to the number equations

$$n_a = \frac{1}{2V}\sum_{\mathbf{k}}\left[\left(1+\frac{\xi_{\mathbf{k}}}{E_{\mathbf{k}}}\right)f^+_{\mathbf{k}}+\left(1-\frac{\xi_{\mathbf{k}}}{E_{\mathbf{k}}}\right)(1-f^-_{\mathbf{k}})\right] \tag{3.18}$$

$$n_b = \frac{1}{2V}\sum_{\mathbf{k}}\left[\left(1+\frac{\xi_{\mathbf{k}}}{E_{\mathbf{k}}}\right)f^-_{\mathbf{k}}+\left(1-\frac{\xi_{\mathbf{k}}}{E_{\mathbf{k}}}\right)(1-f^+_{\mathbf{k}})\right] \tag{3.19}$$

3.4.1 Absence of Intra-Plane Interactions

When electron-electron and hole-hole interactions are neglected, the gap equations simplify [102]

$$\Delta_{\mathbf{k}} = -\frac{1}{V}\sum_{\mathbf{k}'}{}' U^{ab}_{\mathbf{k}\mathbf{k}'}\frac{\Delta_{\mathbf{k}'}}{2E_{\mathbf{k}'}}(1-f^{+}_{\mathbf{k}'}-f^{-}_{\mathbf{k}'}) \tag{3.20}$$

$$\xi_{\mathbf{k}} = \epsilon_{\mathbf{k}}-\mu \tag{3.21}$$

$$E^2_{\mathbf{k}} = \xi^2_{\mathbf{k}}+\Delta^2_{\mathbf{k}} \tag{3.22}$$

$$f^{\pm}_{\mathbf{k}} = \begin{cases} 1 \text{ if } E^{\pm}_{\mathbf{k}}<0 & E^{\pm}_{\mathbf{k}} = E_{\mathbf{k}} \pm \Delta E_{\mathbf{k}} \\ 0 \text{ if } E^{\pm}_{\mathbf{k}}>0 & \Delta E_{\mathbf{k}} = \Delta\xi_{\mathbf{k}} \end{cases} \tag{3.23}$$

Here the unknowns are the gap function $\Delta_{\mathbf{k}}$ and the chemical potential values μ_a and μ_b that give the desired number of electrons and hole densities.

3.4.2 Screening

The screening of the Coulomb potential due to interactions has not been studied in e-h bilayer for the condensed phase. The 2D screening due to interaction is difficult to take into account properly. For example, the TF screening length does not depend on density [120]. Gortel and and Swierkowski attempeted to include 2D screening for the condensate in the case of equal population within the RPA [101]. They use the normal phase susceptibilities in the dielectric function [121]. In that sense it is not a fully consistent calculation. The result is the drastic reduction of the gap function over-estimating the screening. We have tried this type of RPA screening for imbalanced layer and found similar suppression of the gap and discontinuities at the Fermi surface resulting from the discontinuity in 2D RPA susceptibility.

There is a simple screening mechanism that can be taken into account by a Yukawa like potential and that is introduced by the presence of the gates which are necessary to independently control the densities in the e-h bilayer [104]. The potential due to an electron is altered by the conducting gate layer. This can be modeled by an image charge behind the gate. At a long distance the electron plus its image charge are seen as a dipole, the bare Coulomb potential is thus

screened. In recent experiments with metal gates to control the charge densities the separation between the gate and 2D layer is about 250 nm [122]. Therefore the image charge is 500 nm distant from the real charge and we can consider that at larger distances than 500 nm the Coulomb potential will be seen as dipole potential. In our calculations we take the screening length to be 300 nm which in terms of the effective Bohr radius is about 20 a_B. We include screening in this simple form and disregard the 2D screening which is difficult to handle properly. In this case the screened interactions are written as

$$U_{\mathbf{q}}^{aa} = \frac{2\pi e^2}{\varepsilon \left[q^2 + q_0^2\right]^{1/2}} \qquad U_{\mathbf{q}}^{ab} = \frac{2\pi e^2}{\varepsilon \left[q^2 + q_0^2\right]^{1/2}} \mathrm{e}^{-qd} \tag{3.24}$$

where $q_0 = 1/20 a_B$.

3.4.3 Numerical Solution of the Gap Equations

The implementation of the numerical solution to the gap equations is by a multi-dimensional Newton-Raphson method for non-linear equations.

Given the inter-plane separation d and densities n_a, n_b, we want to solve for functions $\Delta_{\mathbf{k}}, \xi_{\mathbf{k}}, f_{\mathbf{k}}^+, f_{\mathbf{k}}^-$ represented on a one dimensional grid of k points and the chemical potentials μ_a, μ_b that give the desired densities.

A common method to solve the gap equations is to use an iteration scheme where an initial guess is iterated using the gap equations, substituting it back into the equations either directly or by mixing with the initial solution until convergence is reached. With equal electron and hole density we find that an iterative method converges to a non-zero gap function for all density values. With unequal densities the iterative method is sensitive to the starting point and usually converges to $\Delta_{\mathbf{k}} = 0$ solution.

An alternative way is to look at the equations as a non-linear root finding problem. Typically, we use a mesh of 100 points to represent the unknown functions of k. Together with chemical potentials this results in 300+2 unknowns. In the case of inter-planar interactions only, this reduces to 100+2 unknowns. For unequal populations, the range of k is broken into two or three intervals to handle the discontinuities at zero temperature.

Gaussian quadrature is used to carry out the integrations. We use the Newton-Raphson algorithm from Numerical Recipes [123] to solve for the unknown variables. The algorithm requires the evaluation of gradients. Therefore, instead of the zero temperature equations, we work with finite but small temperature to make the unknowns and integrands smooth functions of wave vector k. We make sure that we obtain a sharp $T = 0$ distribution functions and further decreasing the temperature does not affect our results. Details are given in Sec. 3.11.

3.4.4 Units

We work in Rydberg units , i.e. length is measured in effective Bohr radius a_B, momentum in $1/a_B$ and energy in effective Rydberg (Ryd).

$$1\text{Ryd} = \frac{\hbar^2}{2ma_B^2} = \frac{e^2}{2\varepsilon a_B} \tag{3.25}$$

where

$$a_B = \frac{\hbar^2\varepsilon}{me^2} \tag{3.26}$$

with the reduced mass m defined by

$$\frac{1}{m} = \frac{1}{m_a} + \frac{1}{m_b} \tag{3.27}$$

and $m_a = m_e$ and $m_b = m_h$ are the band mass of the electron and hole respectively.

3.5 Solutions of the Gap Equations

In this section we illustrate the solutions to the gap equations at representative density and population polarization. An asymmetry with respect to positive and negative polarization (excess electrons or holes) is introduced if electron and hole masses are different.

We use parameters that are relevant for experimental realizations in GaAs semiconductor structures and take mass ratio to be $m_a/m_b = 0.07/0.30$ and inter-layer separation $d = a_B$.

We present the solutions with and without the intra-layer (same species) interactions in order to see the effects of intra-layer interactions. The simple screening model, which removes a divergence in the derivative of the gap, smoothens the gap function and quasi-particle energy curves.

3.5.1 Balanced Populations

The gap function and quasi-particle energy at $r_s = 3$ and $\alpha = 0$ for four different cases are illustrated in Fig. 3.1-3.4 . Here the electron and hole chemical potentials are taken to be equal to each other so that their difference vanishes, $h = 0$. The reason the $E^{\pm}_{\mathbf{k}}$ branches are different from $E_{\mathbf{k}}$ is that there is a k-dependent difference $\Delta\xi_{\mathbf{k}}$ due to different electron and hole masses. These calculations are exactly at zero temperature. At $T = 0$ the chemical potential values could be different and still give the same solution provided that $E^{\pm}_{\mathbf{k}} > 0$ so that the quasi-particle states are not occupied and we still have equal electron and hole populations. Different chemical potentials would shift the $E^{\pm}_{\mathbf{k}}$ up or down.

The model screening approximately reduces the gap by half compared to bare interaction whereas the intra-layer interactions have a smaller effect at the density corresponding to $r_s = 3$.

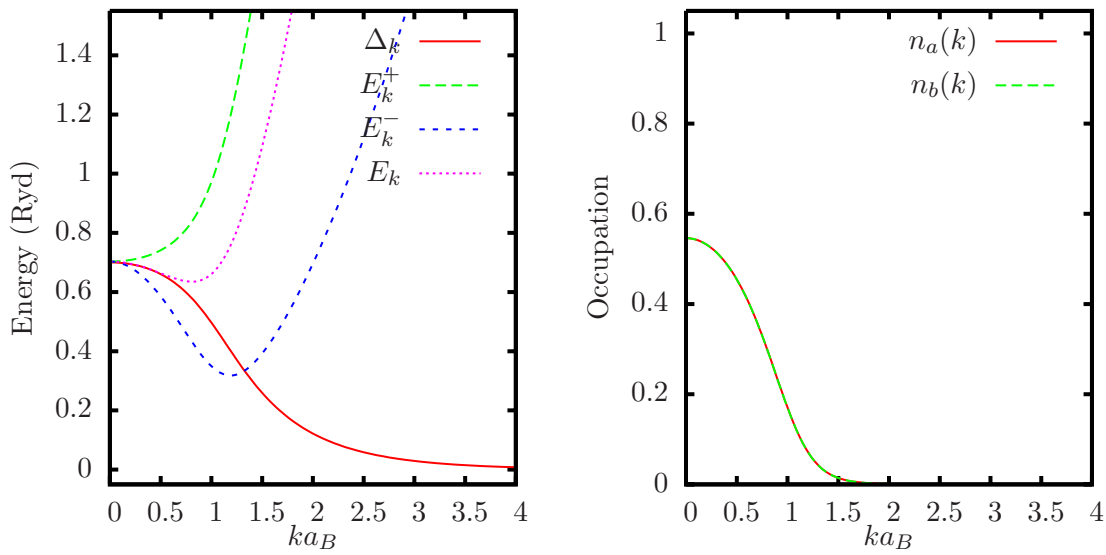

Figure 3.1: Gap function and quasi-particle energies at $r_s = 3, \alpha = 0$ with bare inter-layer interactions only. Occupation numbers distribution shown on the right has no Fermi surface.

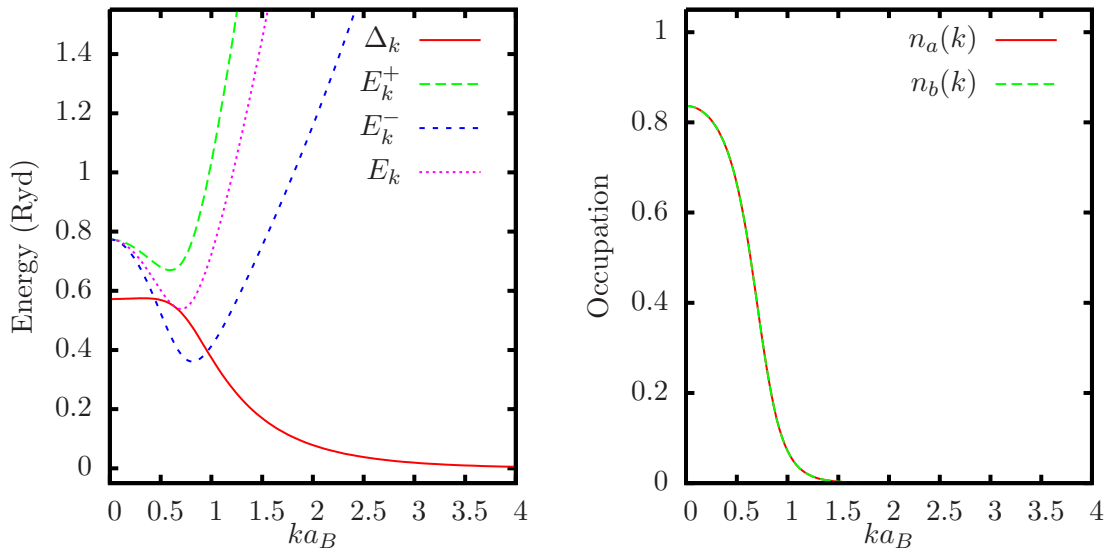

Figure 3.2: Gap function and quasi-particle energies at $r_s = 3, \alpha = 0$ with bare inter- and intra-layer interactions. Occupation numbers are shown on the right.

These BCS solutions have wave functions of the form

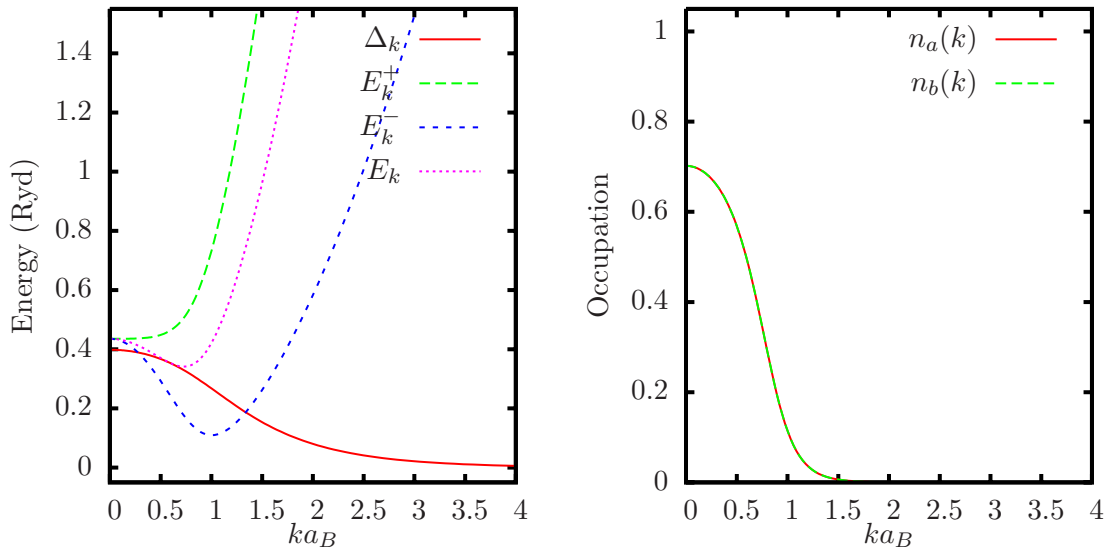

Figure 3.3: Gap function and quasi-particle energies at $r_s = 3, \alpha = 0$ with screened inter-layer interactions only. Occupation numbers are shown on the right.

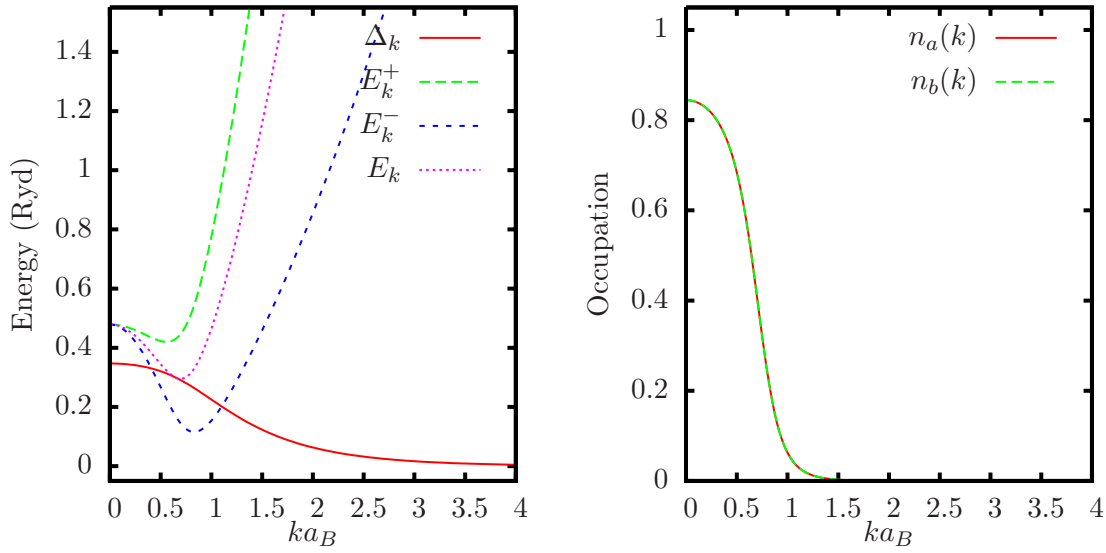

Figure 3.4: Gap function and quasi-particle energies at $r_s = 3, \alpha = 0$ with screened inter- and intra-layer interactions. Occupation numbers are shown on the right.

$$|\Psi_{BCS}\rangle = \prod_{\mathbf{k}} (u_{\mathbf{k}} + v_{\mathbf{k}} a^\dagger_{\mathbf{k}} b^\dagger_{-\mathbf{k}}) |0\rangle \tag{3.28}$$

where $|v_{\mathbf{k}}|^2$ is the distribution function for electrons and holes. (Expressions for $u_{\mathbf{k}}, v_{\mathbf{k}}$ in terms of $\Delta_{\mathbf{k}}, E_{\mathbf{k}}$ are given in Sec. 3.11. Note that due to interactions, the distribution is broadened and is different from a step function for non-interacting particles at $T = 0$.

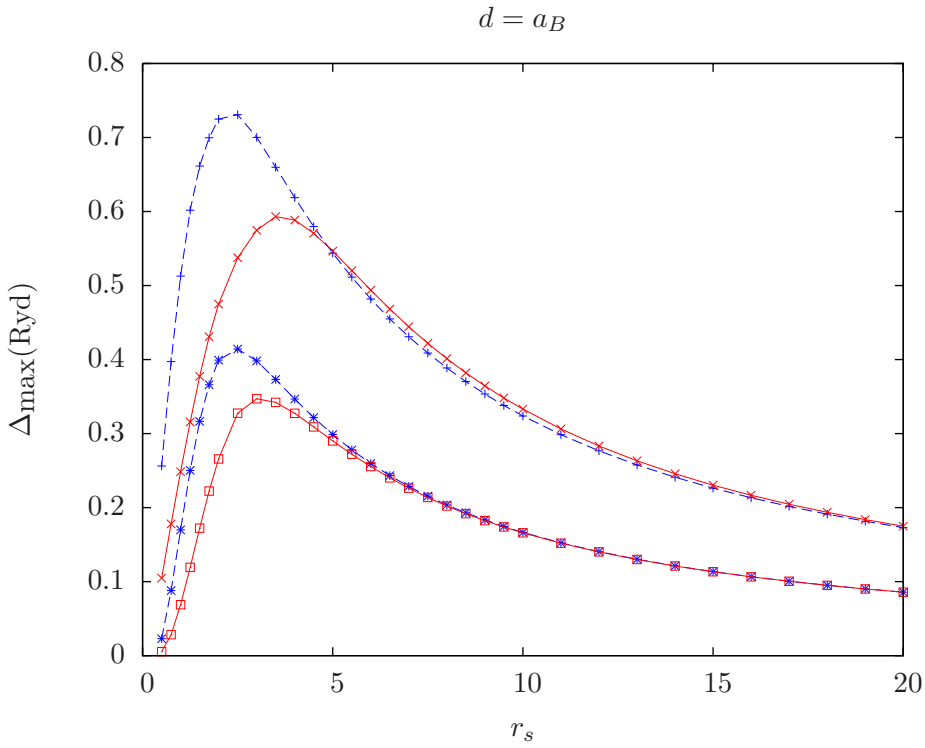

Figure 3.5: Maximum value of the gap function $\Delta_{\max}$ as a function of the density parameter r_s at fixed inter-layer separation $d = a_B$. Blue dashed curves show the values with inter-layer interactions only and red solid lines show the values with intra- and inter-layer interactions. The upper two curves correspond to bare Coulomb interactions whereas the lower set is obtained using screened interactions.

The main goal of this chapter is to study the effects of intra-layer interactions and screening on the phase diagram in the average density - density imbalance $(r_s - \alpha)$ plane. In Fig. 3.5 we show the effects of intra-layer interactions for equal density at fixed interlayer separation $d = a_B$. We see that for large r_s values the

effect of intra-layer interactions becomes smaller as expected because the intra-layer interactions scale as $1/r_s$. However, for r_s values up to $r_s = 5$, we see a noticeable decrease in the gap when electron-electron and hole-hole interactions are present. The simple model of screening employed here diminishes the gap approximately by half over all the density range.

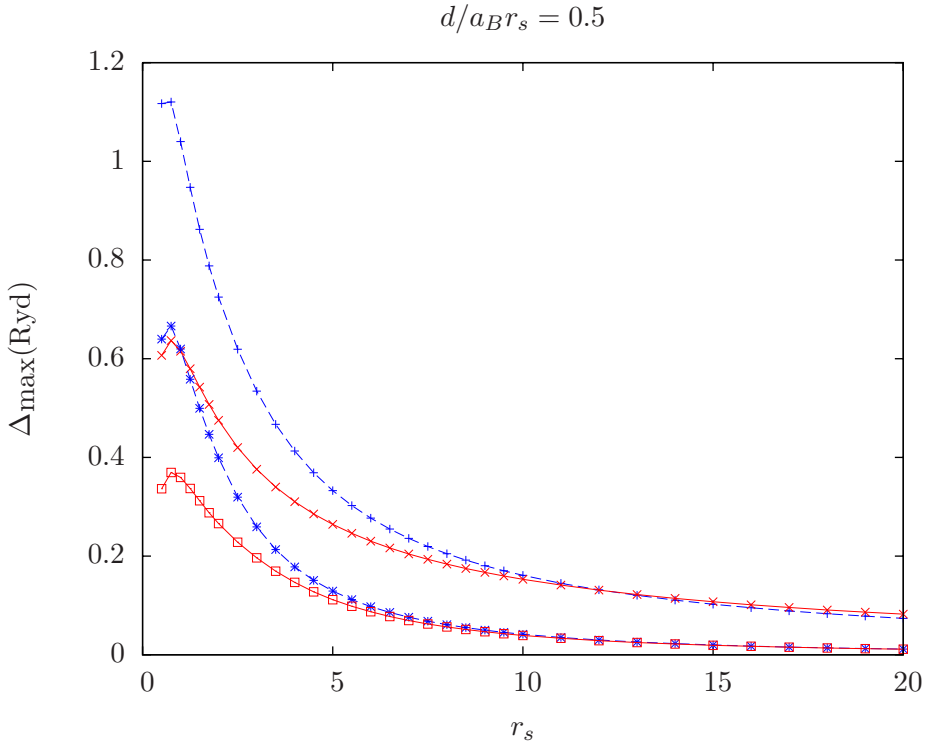

Figure 3.6: Maximum value of the gap function $\Delta_{\max}$ as a function of the density parameter r_s at fixed inter-layer separation $d/a_B r_s = 0.5$. Blue dashed curves show the values with inter-layer interactions only and red solid lines show the values with intra- and inter-layer interactions. The upper two curves correspond to bare Coulomb interactions whereas the lower set is obtained using screened interactions.

In the above comparison the ratio of the inter- to intra-layer interactions changes with r_s because d is kept fixed. The inter-layer interactions scale as $1/d$ for $d > a_B r_s$. For $d > a_B r_s$ keeping the ratio $d/a_B r_s$ fixed at different densities would show the pairing as a function of density at fixed inter-/intra-layer

interaction. However, this means large values of d for large r_s which decreases the coupling. In order to have comparable gap values we show the maximum value of the gap function as a function of r_s in Fig. 3.6 for $d/a_B r_s = 0.5$. The behavior is qualitatively similar to the case with fixed d. At these values of the parameters we expect to see the effects of intra-layer interactions up to $r_s \approx 5$.

3.5.2 Imbalanced Populations

For unequal populations the resulting wave function has a certain range of $\mathbf{k}$ (the set denoted by $\mathbf{P}$ below) states occupied with quasi-particles of the BCS theory giving rise to population imbalance. The region $\mathbf{P}$ is where the quasi-particle $E^{\pm}_{\mathbf{k}}$ energy becomes negative, i.e. less than that of the ground pair energy and the corresponding quasi-particle occupation becomes unity. Incidentally, the quasi-particles of BCS theory are just electron or holes states at that wave vector $\mathbf{k}$. Outside the set $\mathbf{P}$ we have pairs $\mathbf{k}, -\mathbf{k}$ of electrons and holes.[2]

$$|\Psi\rangle = \prod_{\mathbf{k}\in\mathbf{P}} \alpha^{\dagger}_{\mathbf{k}} |\Psi_{BCS}\rangle \tag{3.29}$$

$$= \prod_{\mathbf{q}\in\mathbf{P}} a^{\dagger}_{\mathbf{q}} \prod_{\mathbf{k}\notin\mathbf{P}} (u_{\mathbf{k}} + v_{\mathbf{k}} a^{\dagger}_{\mathbf{k}} b^{\dagger}_{-\mathbf{k}}) |0\rangle \tag{3.30}$$

At zero temperature we thus have a region in the $\mathbf{k}$ space where the electron (or hole) occupation becomes unity. Therefore, at $T = 0$ there can be one or two Fermi spheres depending where the set of $\mathbf{k} \in \mathbf{P}$ vectors are. These topologically different phases will be called Sarma 1 (S1) and Sarma 2 (S2) phases, respectively. These states have also been called breached pair states [124–126] because of the existence of Fermi spheres together with a condensate. The gap function is non-zero but there are gapless excitations.

Representative solutions displaying the two different type of states at various average density parameter r_s and population polarization α are shown in Fig. 3.7-3.22 for the inter-layer separation $d = a_B$. The figures show the gap function $\Delta_{\mathbf{k}}$ and the quasi-particle energies $E^{\pm}_{\mathbf{k}}$ on the left and the electron and hole

[2]For QMC applications this state can be written as a Slater determinant in real space.

occupation numbers n_a, n_b on the right. Fig. 3.7-3.10 show solution for electron and holes interacting with the bare inter-layer Coulomb interaction only. For each interaction model we show examples of Sarma 1 and Sarma 2 phases with excess electrons (light majority particles) or excess holes (heavy majority carriers. For example, Fig. 3.7 shows a S2 phase with positive population polarization α and Fig. 3.10 shows a S1 phase with negative population polarization for the case of bare inter-layer interactions only. In Fig. 3.11-3.14 in-plane Coulomb interactions, i.e. electron-electron and hole-hole interactions, are added. We include gate screening in Fig. 3.15-3.18 neglecting intra-layer interactions and in Fig. 3.19-3.22 with gate-screened inter-layer and intra-layer interactions.

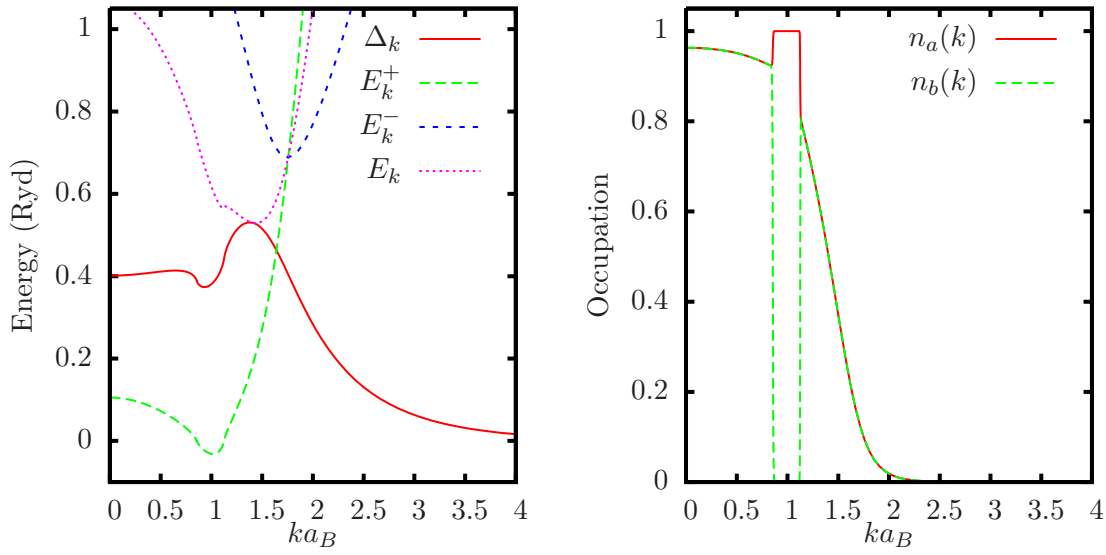

Figure 3.7: Gap function and quasi-particle energies at $r_s = 1.5, \alpha = 0.15$ with bare inter-layer interaction only. This is a Sarma 2 phase with excess electrons. Occupation numbers are shown on the right. ($m_e/m_h = 0.07/0.30$ and $d = a_B$.)

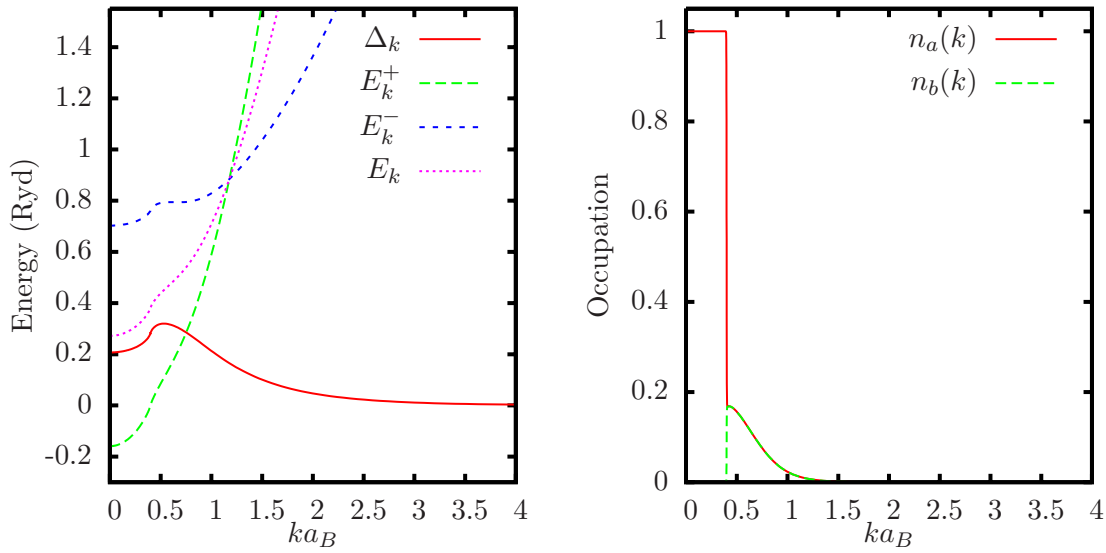

Figure 3.8: Gap function and quasi-particle energies at $r_s = 5, \alpha = 0.5$ with bare inter-layer interaction only. This is a Sarma 1 phase with excess electrons. Occupation numbers are shown on the right. ($m_e/m_h = 0.07/0.30$ and $d = a_B$.)

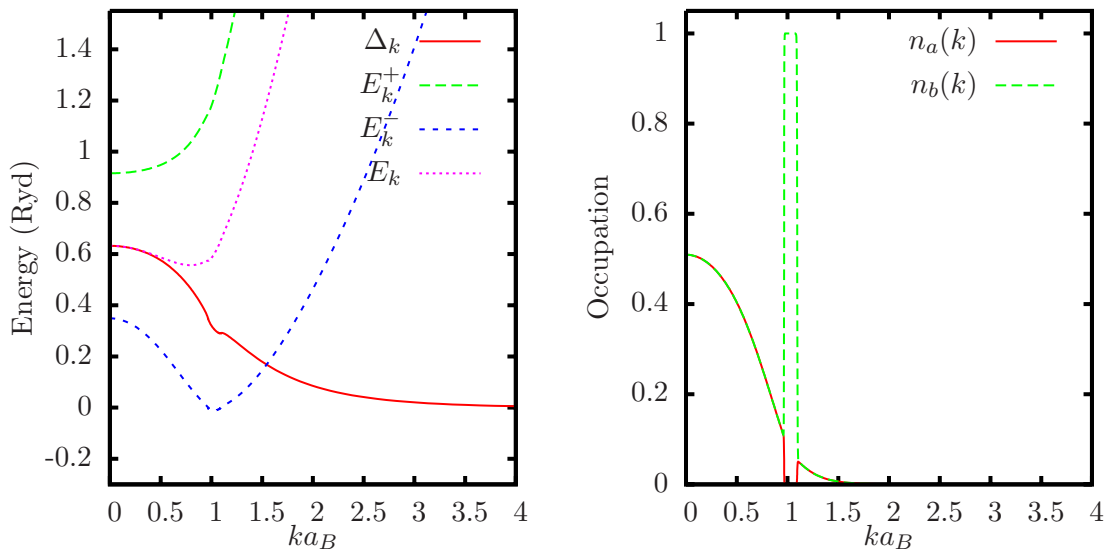

Figure 3.9: Gap function and quasi-particle energies at $r_s = 3, \alpha = -0.3$ with bare inter-layer interaction only. This is a Sarma 2 phase with excess holes. Occupation numbers are shown on the right. ($m_e/m_h = 0.07/0.30$ and $d = a_B$.)

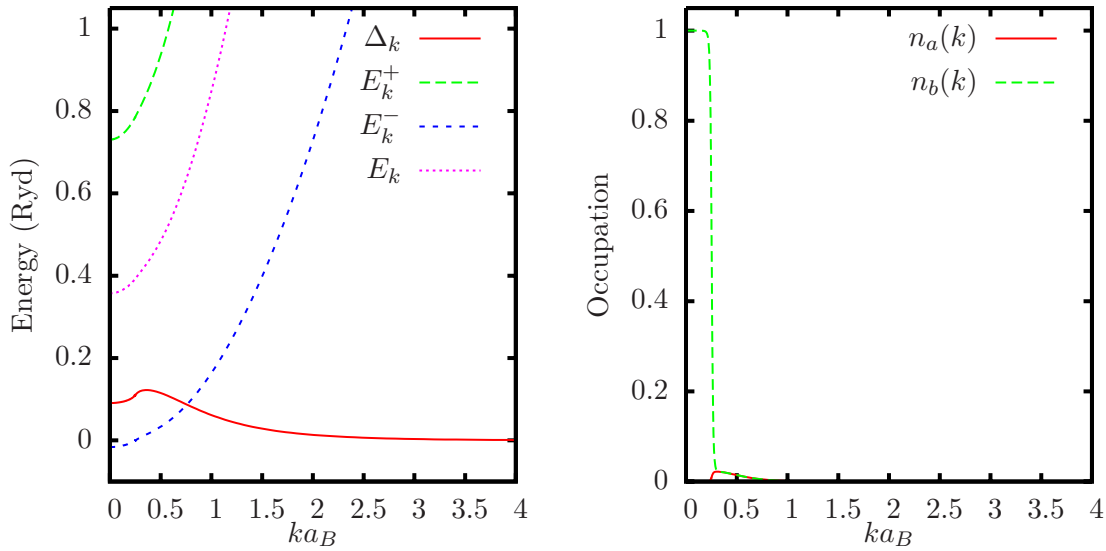

Figure 3.10: Gap function and quasi-particle energies at $r_s = 10, \alpha = -0.8$ with bare inter-layer interaction only. This is a Sarma 1 phase with excess holes. Occupation numbers are shown on the right. ($m_e/m_h = 0.07/0.30$ and $d = a_B$.)

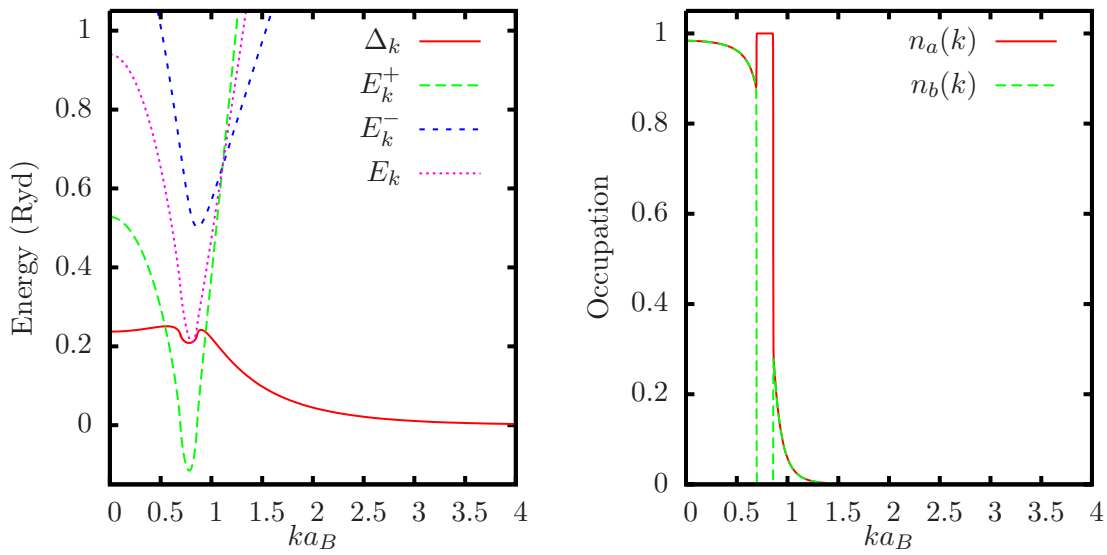

Figure 3.11: Gap function and quasi-particle energies at $r_s = 2.5, \alpha = 0.2$ with bare intra- and inter-layer interactions. This is a Sarma 2 phase with excess electrons. Occupation numbers are shown on the right. ($m_e/m_h = 0.07/0.30$ and $d = a_B$.)

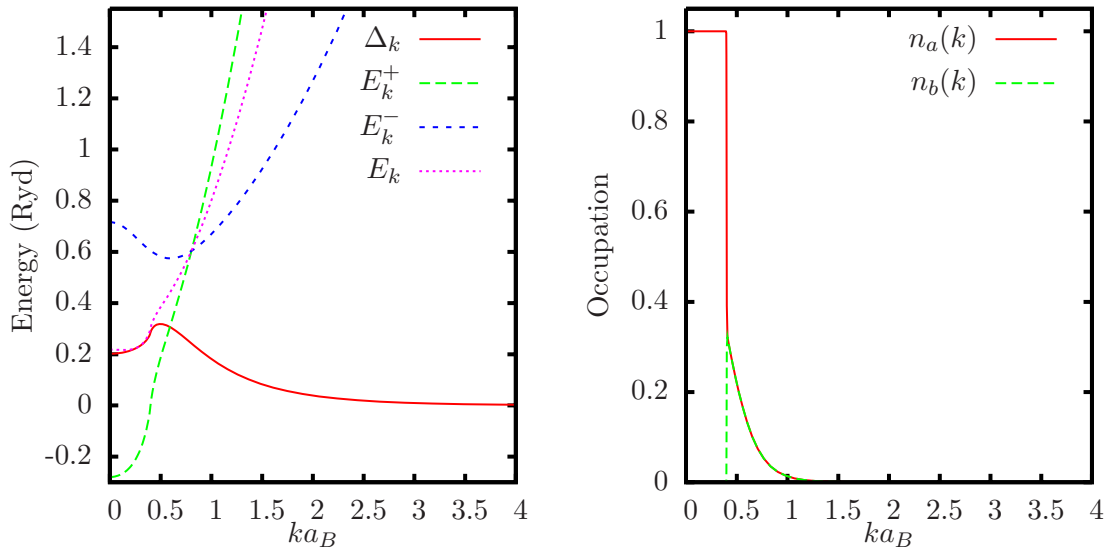

Figure 3.12: Gap function and quasi-particle energies at $r_s = 5, \alpha = 0.5$ with bare intra- and inter-layer interactions. This is a Sarma 1 phase with excess electrons. Occupation numbers are shown on the right. ($m_e/m_h = 0.07/0.30$ and $d = a_B$.)

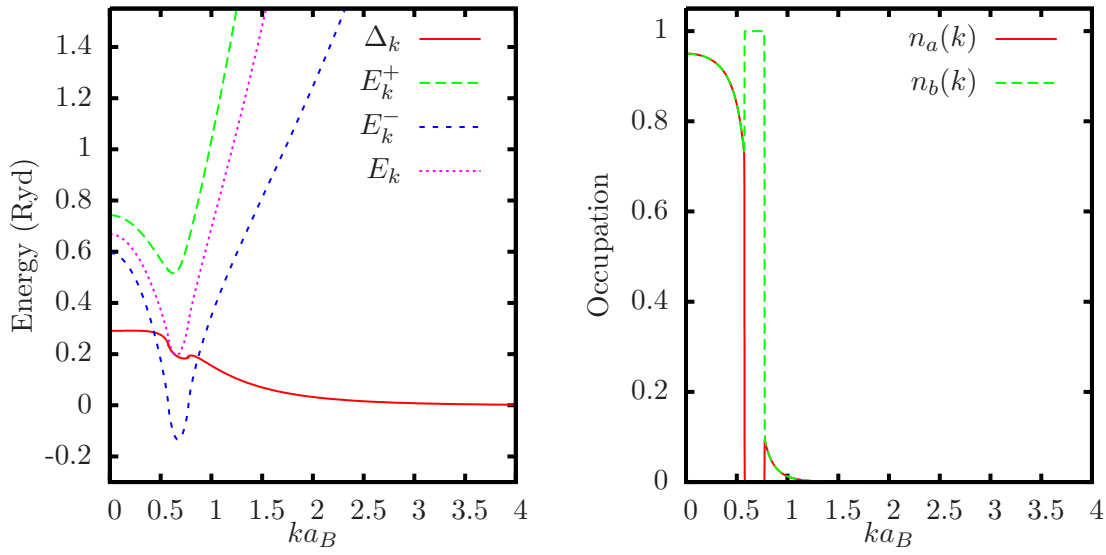

Figure 3.13: Gap function and quasi-particle energies at $r_s = 3, \alpha = -0.3$ with bare intra- and inter-layer interactions. This is a Sarma 2 phase with excess holes. Occupation numbers are shown on the right. ($m_e/m_h = 0.07/0.30$ and $d = a_B$.)

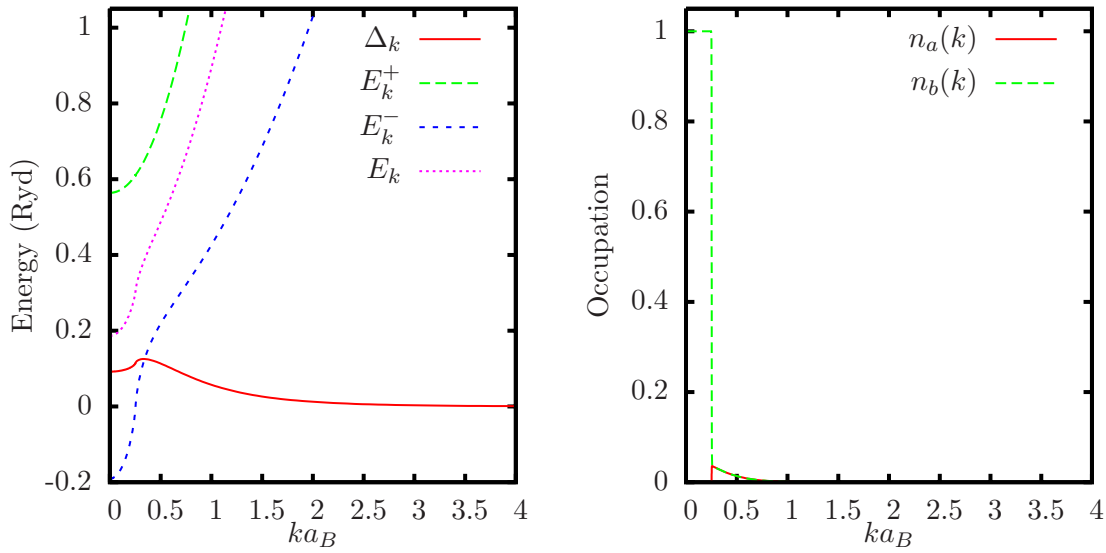

Figure 3.14: Gap function and quasi-particle energies at $r_s = 10, \alpha = -0.8$ with bare intra- and inter-layer interactions. This is a Sarma 1 phase with excess holes. Occupation numbers are shown on the right. ($m_e/m_h = 0.07/0.30$ and $d = a_B$.)

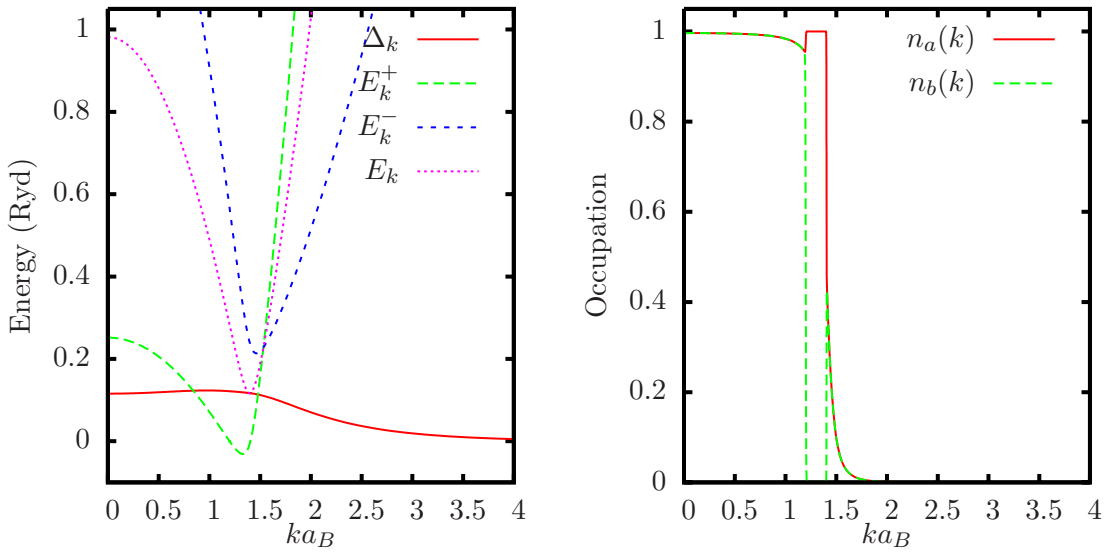

Figure 3.15: Gap function and quasi-particle energies at $r_s = 1.5, \alpha = 0.15$ with gate screened inter-layer interaction only. A Sarma 2 phase with excess electrons. Occupation numbers are shown on the right. ($m_e/m_h = 0.07/0.30$ and $d = a_B$.)

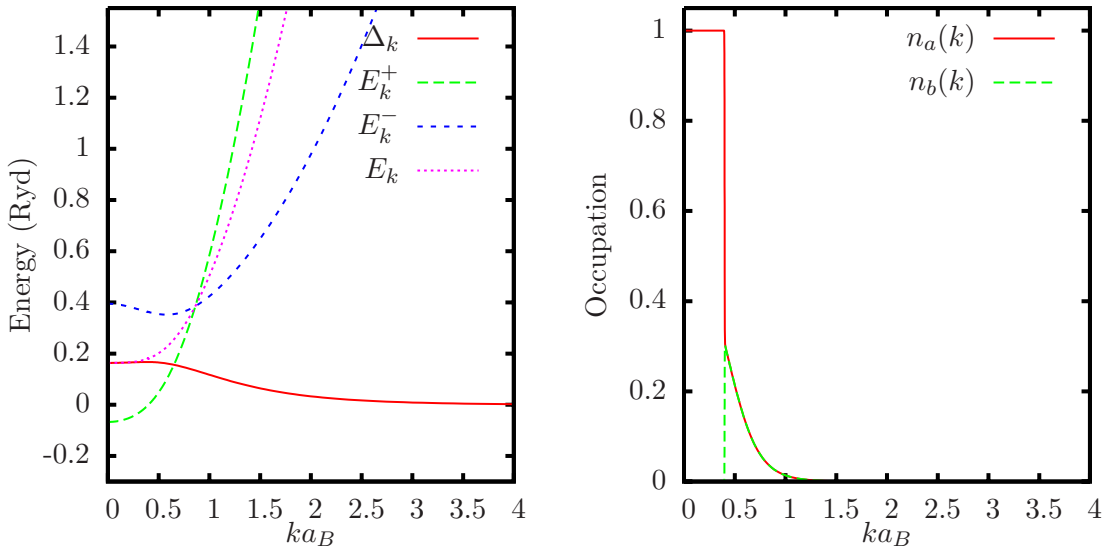

Figure 3.16: Gap function and quasi-particle energies at $r_s = 5, \alpha = 0.5$ with gate screened inter-layer interaction only. This is a Sarma 1 phase with excess electrons. Occupation numbers are shown on the right. ($m_e/m_h = 0.07/0.30$ and $d = a_B$.)

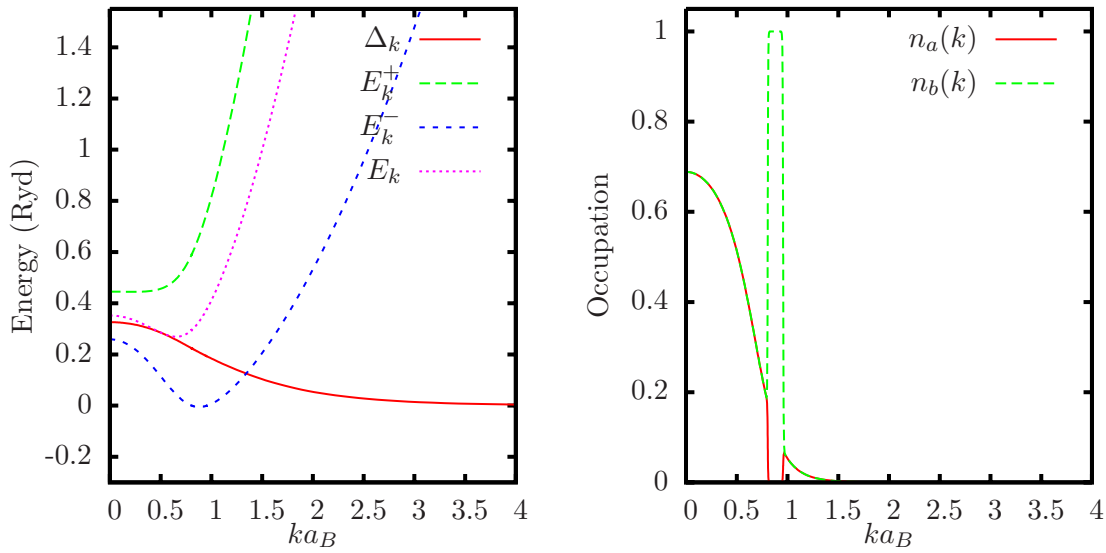

Figure 3.17: Gap function and quasi-particle energies at $r_s = 3, \alpha = -0.3$ with gate screened inter-layer interaction only. A Sarma 2 phase with excess holes. Occupation numbers are shown on the right. ($m_e/m_h = 0.07/0.30$ and $d = a_B$.)

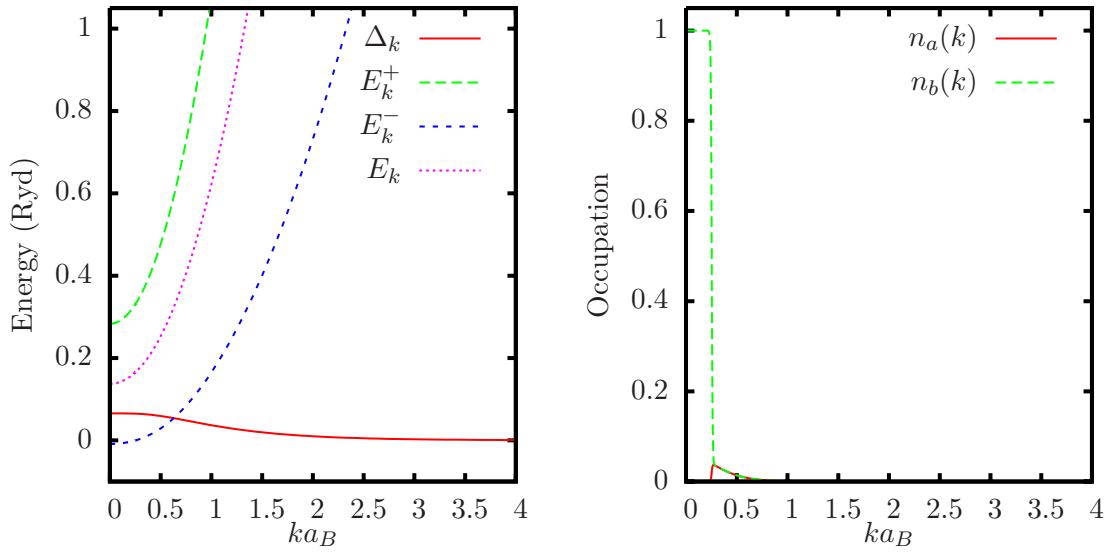

Figure 3.18: Gap function and quasi-particle energies at $r_s = 10, \alpha = -0.8$ with gate screened inter-layer interaction only. This is a Sarma 1 phase with excess holes. Occupation numbers are shown on the right. ($m_e/m_h = 0.07/0.30$ and $d = a_B$.)

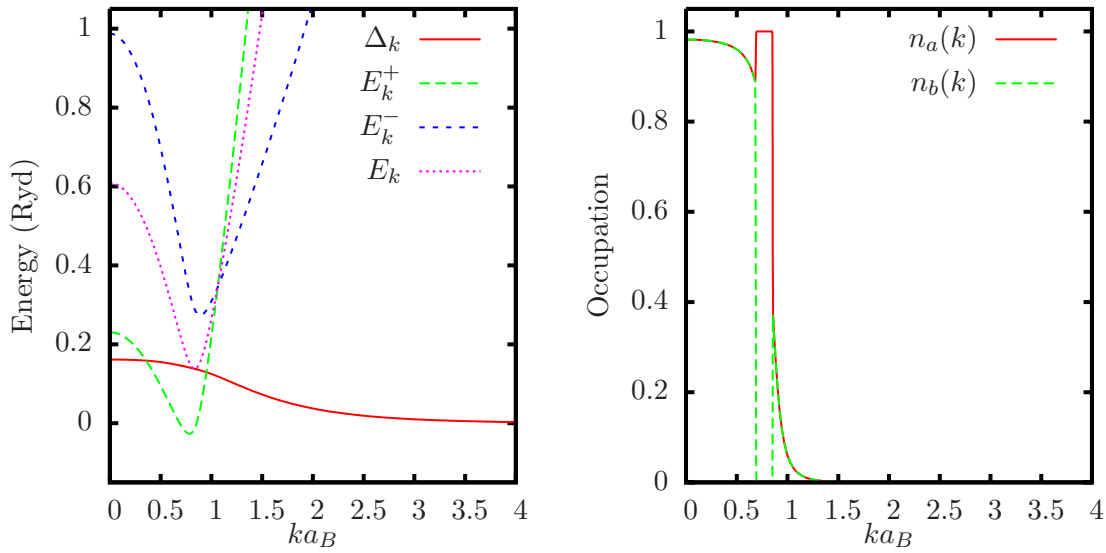

Figure 3.19: Gap function and quasi-particle energies at $r_s = 2.5, \alpha = 0.2$ with gate screened intra- and inter-layer interactions. A Sarma 2 phase with excess electrons. Occupation numbers on the right. ($m_e/m_h = 0.07/0.30$ and $d = a_B$.)

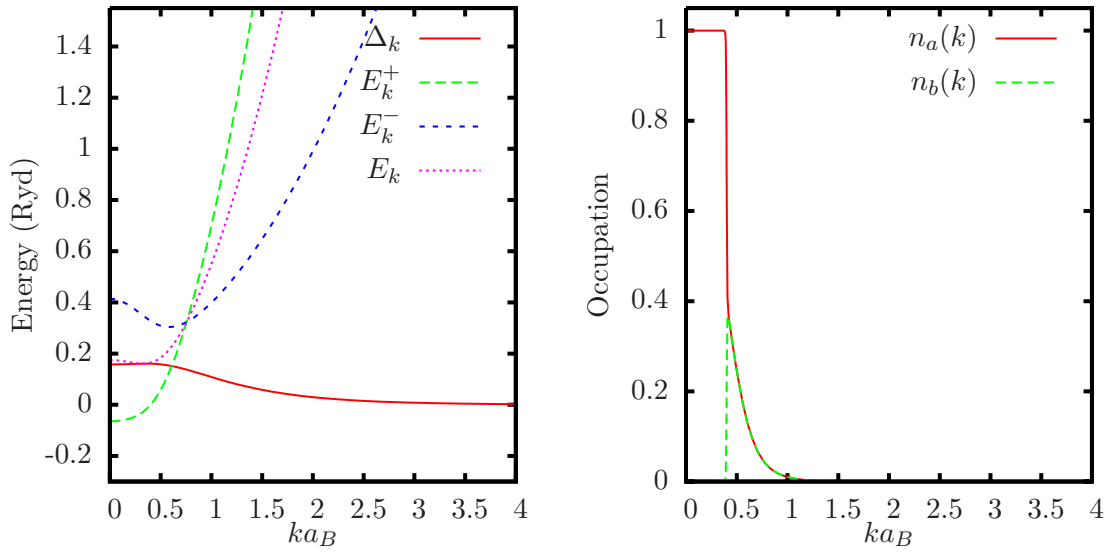

Figure 3.20: Gap function and quasi-particle energies at $r_s = 5, \alpha = 0.5$ with gate screened intra- and inter-layer interactions. This is a Sarma 1 phase with excess electrons. Occupation numbers are shown on the right. ($m_e/m_h = 0.07/0.30$ and $d = a_B$.)

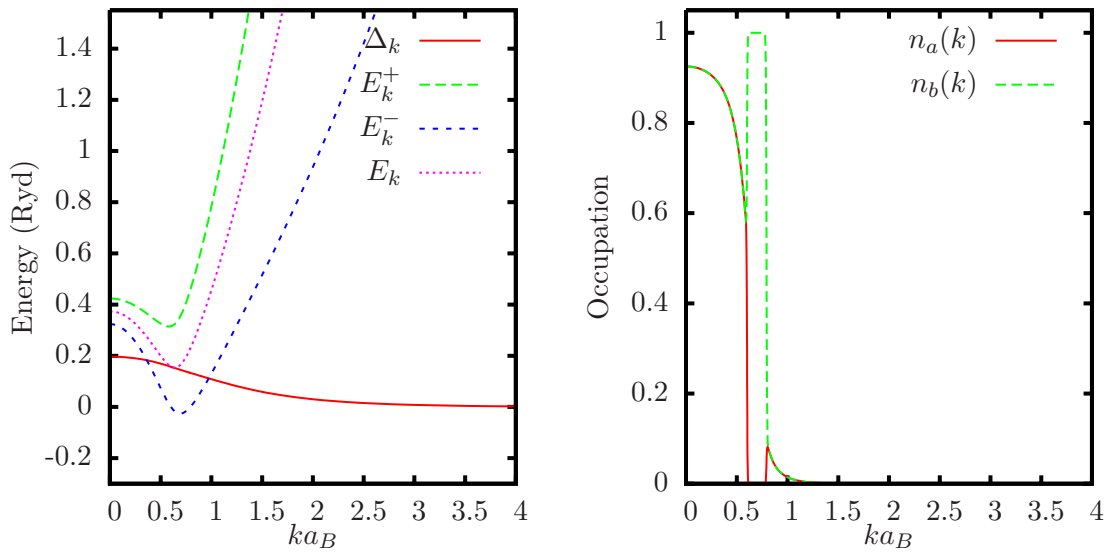

Figure 3.21: Gap function and quasi-particle energies at $r_s = 3, \alpha = -0.3$ with gate screened intra- and inter-layer interactions. A Sarma 2 phase with excess holes. Occupation numbers on the right. ($m_e/m_h = 0.07/0.30$ and $d = a_B$.)

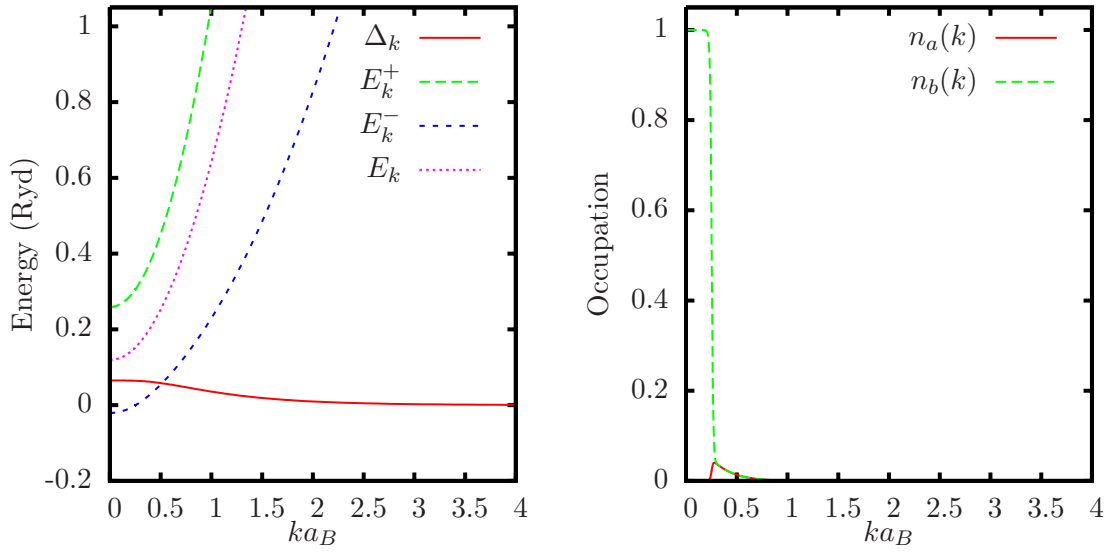

Figure 3.22: Gap function and quasi-particle energies at $r_s = 10, \alpha = -0.8$ with gate screened intra- and inter-layer interactions. A Sarma 1 phase with excess holes. Occupation numbers on the right. ($m_e/m_h = 0.07/0.30$ and $d = a_B$.)

3.6 Comparison with the Normal Phase

Since we are interested in the condensed state with population imbalance between layers, in this section we show the variation of the values of the maximum value of the gap function, which is related to the energy gain with respect to the normal phase, as a function of population polarization α.

The maximum value of the gap at fixed average density (fixed r_s) as a function of population polarization α is shown in Fig. 3.23. Also shown is the energy per particle along with the HF energy. It is seen that the condensed state has lower energy than the normal state and the difference goes to zero as the gap function vanishes with increasing density difference.

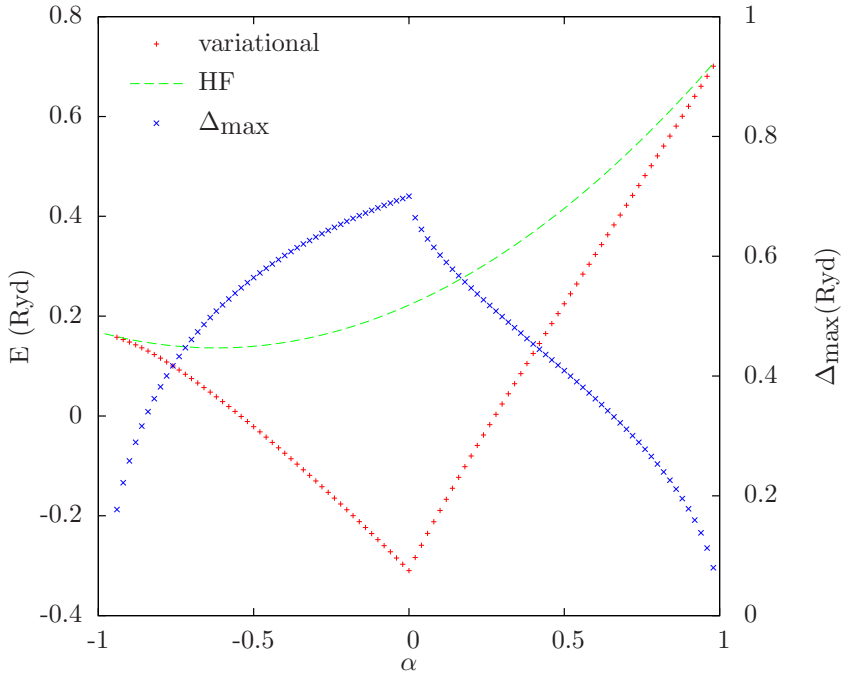

Figure 3.23: Energy and maximum value of $\Delta_{\mathbf{k}}$ as a function of α at $r_s = 3$ for bare inter-layer interactions only. The red points (plus sign) shows the energy of the Sarma phase and the green curve shows the energy of the Hartree-Fock approximation. System parameters are $d = a_B$, $m_e/m_h = 0.07/0.30$

Fig. 3.24 shows the effect of in-plane interactions on the maximum value of the gap function. In general, turning on the inter-plane interactions works in favor of the normal phase because of the negative exchange term. Therefore the polarization range for a non-zero gap and a condensed state is smaller.

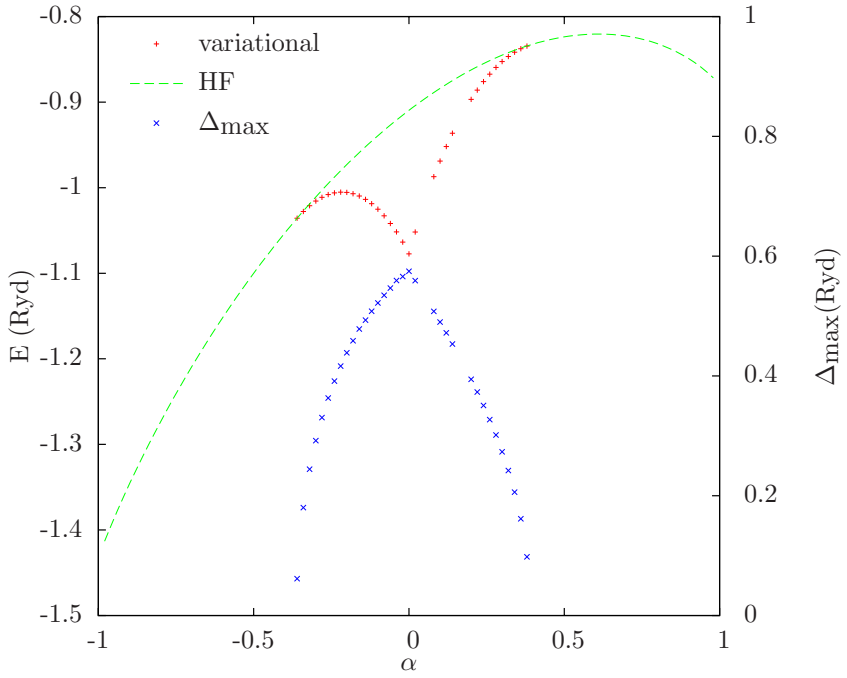

Figure 3.24: Parameters are as in Fig.(3.23) but intra-layer interactions are turned on. Condensed state is present for a smaller window of polarization.

The variation of the maximum of the gap as a function of polarization for representative values of the average density at three different values of the interlayer distance with and without bare intra-plane interactions is shown in Fig. 3.25. Increasing inter-layer distance decreases the coupling and reduces the gap. The greatest gap values take place close to densities corresponding to zero average chemical potential $\mu = 0$, [102] which marks the BCS-BEC crossover boundary.

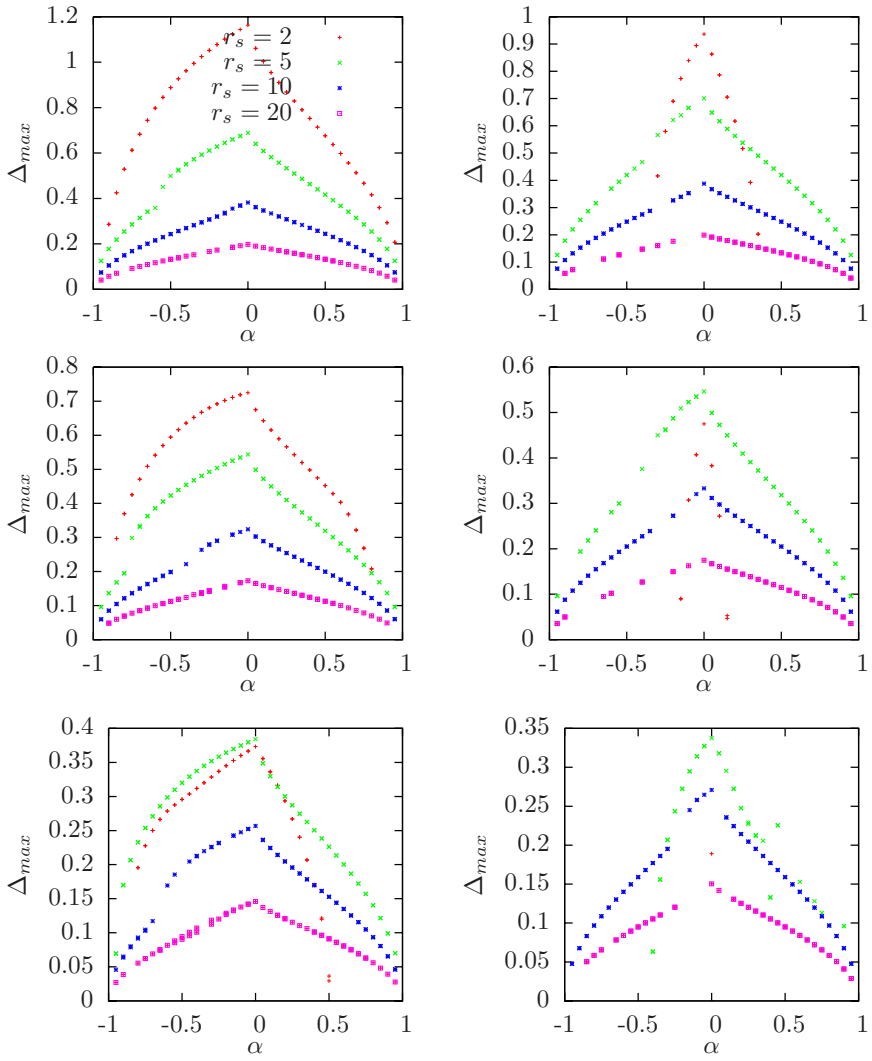

Figure 3.25: The maximum value of the gap function $\Delta_{\max}$ for $r_s = 2, 5, 10, 20$(red, green, blue, purple) at $d = 0.5a_B$(upper panel), $d = a_B$(middle panel) and $d = 2a_B$(lower panel) as a function of polarization with and without the in-plane interactions. The asymmetry with respect to positive and negative polarization α is due $m_e/m_h = 0.07/0.30$. As the average density moves to lower values (larger r_s) the pairing occurs over the whole α range and the pairing gap decreases. Reducing the inter-layer distance d reduces the coupling and this the gap function $\Delta_{\max}$.

3.7 Signature of the Superfluid Phase

In the condensed phase the difference in electron and hole chemical potential makes a jump as $\alpha = 0$ is crossed whereas the average chemical potential is continuous. The jump is also present in electron and hole chemical potential values. Pieri *et al.* suggested that this can be used as an indication of the superfluid state [102]. The discontinuity is shown in Fig. 3.26-3.28 for different cases.

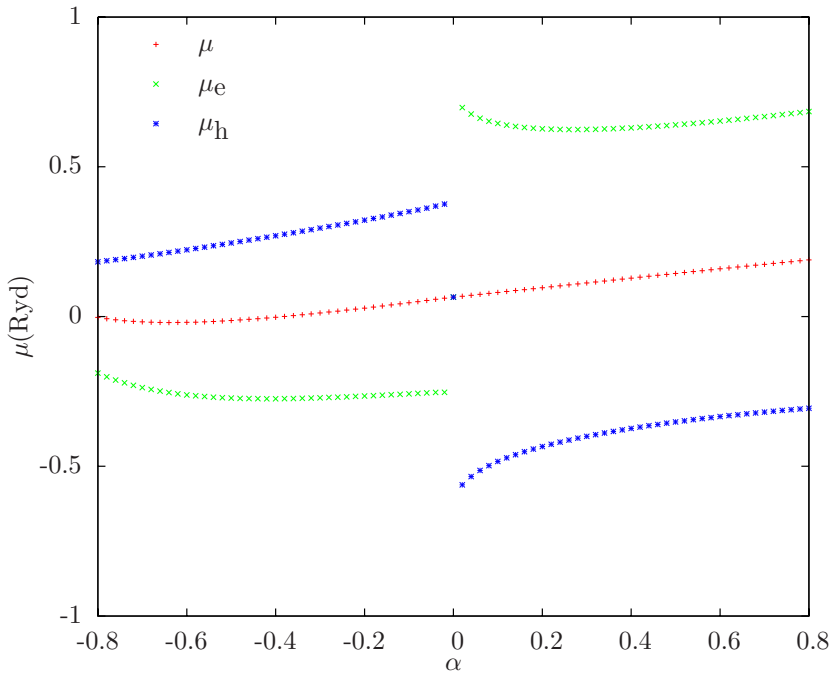

Figure 3.26: Electron and hole chemical potential values and their average as a function of polarization α at $r_s = 3$. Parameters are as in Fig.(3.23) and intra-layer interactions are turned off.

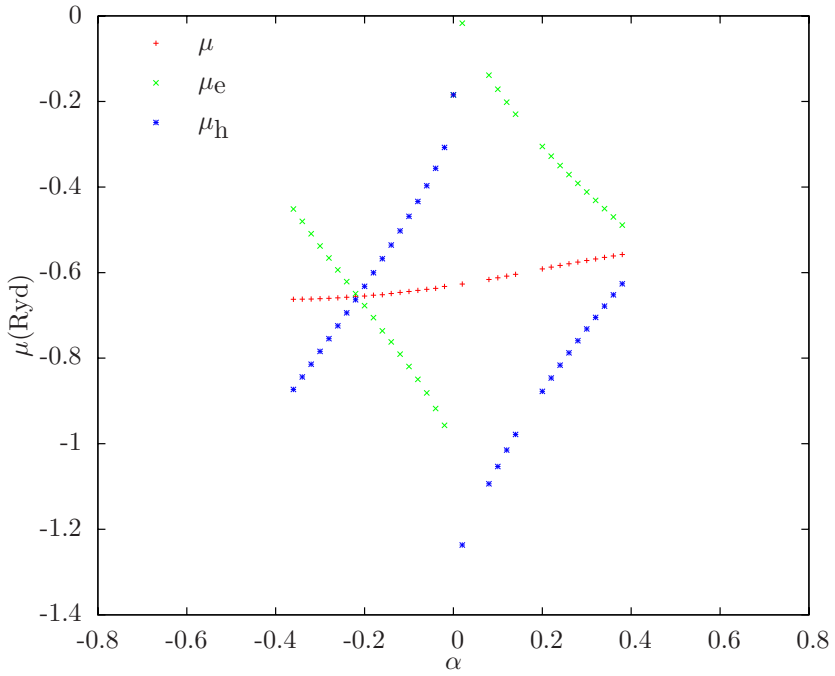

Figure 3.27: Parameters are as in Fig.(3.26) but intra-layer interactions are turned on. The jump at $\alpha = 0$ is an indication of nonzero gap.

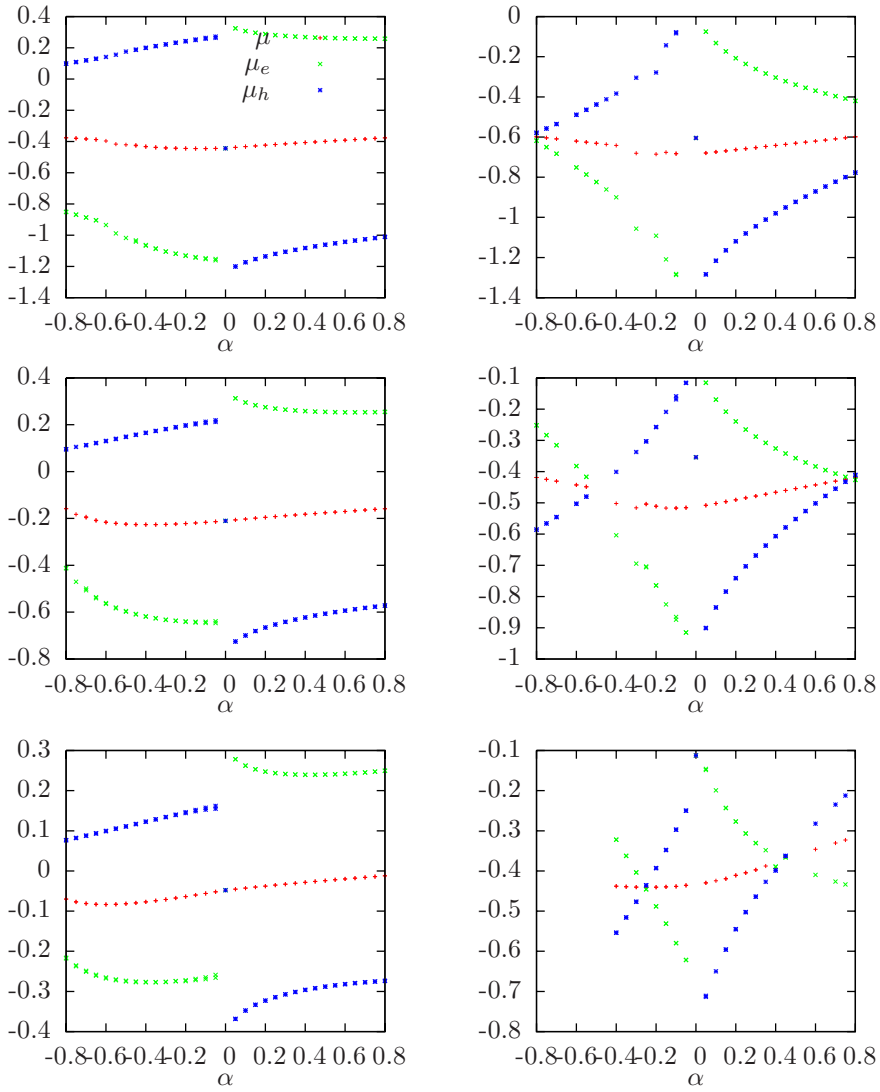

Figure 3.28: Variation of the chemical potential with polarization at $r_s = 5$ for three different values of $d = 0.5, 1, 2a_B$(upper, middle and lower panels, respectively) with and without the in-plane interactions. The jump in electron and hole chemical potential signals the presence of a pairing gap which should be overcome in opposite directions to create population imbalance for electrons and holes.

3.8 Local Stability

The local stability of the Sarma phase is usually assessed by calculating the superfluid mass density (phase stiffness) [102]. This quantity should be positive for a locally stable state and a negative value is identified with an instability. This instability is believed to be towards an FFLO phase [102, 127, 128]. However the existence of a locally stable Sarma phase does not exclude the possibility that there can still exist an FFLO phase with still lower energy.

The superfluid mass density is given by [74]

$$\rho_s = m_{\rm e} n_{\rm e} + m_{\rm h} n_{\rm h} - \frac{\hbar^2 \beta}{8\pi} \int dk k k^2 \frac{1}{2} \left[\frac{1}{\cosh^2(\beta E^+_{\mathbf{k}}/2)} + \frac{1}{\cosh^2(\beta E^-_{\mathbf{k}}/2)} \right] \quad (3.31)$$

where β is inverse temperature. At $T = 0$ this expression can be written as [102]

$$\rho_s = m_{\rm e} n_{\rm e} + m_{\rm h} n_{\rm h} - \frac{\hbar^2}{4\pi} \sum_{j,\lambda} \frac{(k^\lambda_j)^3}{\left| \frac{dE^\lambda_k}{dk} \right|_{k=k^\lambda_j}} . \quad (3.32)$$

where k^λ_j are the roots of E^λ_k with $\lambda = \pm$.

At zero temperature the last expression involves the derivative of Δ_k (through the derivative of $E^\pm_k$) at the zero crossings of $E^\pm_k$. Our calculations are carried out at nonzero but small temperature (which is needed to have a continuously changing functions for our numerical approach). We find that this derivative diverges logarithmically as $T \to 0$ for the bare Coulomb interaction. This divergence is shown in Fig. 3.29-3.31. This means that in this model at $T = 0$ the Sarma phase is always locally stable because the negative contribution to ρ_s vanishes. This confirms the expectations of Wilczek and coworkers [125] that mass ratio and the momentum structure of the interaction are crucial for determining the stability of Sarma phases. The divergence is due to the simultaneous presence of the Coulomb interaction, which is singular at $q = 0$, and the discontinuity in the distribution function at $T = 0$. The log-divergence at $T = 0$ was missed in the previous work by Pieri *et al.* [102] because the

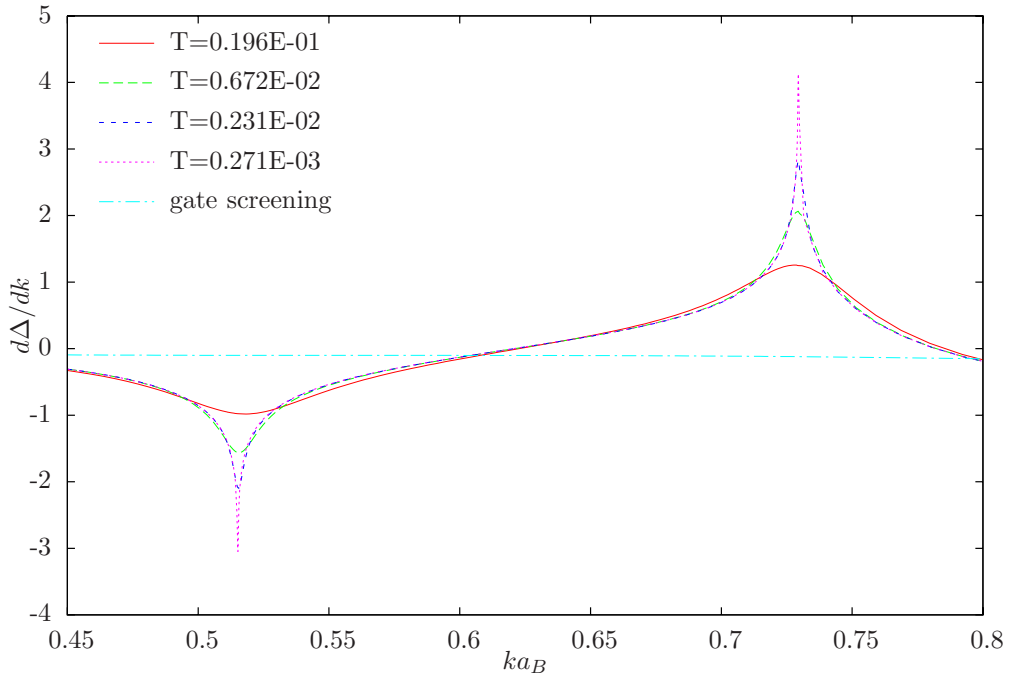

Figure 3.29: The derivative of the gap function as function of k $d\Delta_{\mathbf{k}}/dk$ at $d = a_B, r_s = 3, \alpha = 0.3$ including intra- and inter-plane interactions with $m_e/m_h = 0.07/0.30$ at various temperatures.

temperature used for the calculations was not low enough. We study the behavior of $\mathrm{d}\Delta_{\mathbf{k}}/\mathrm{d}k$ at the zero crossings of $E^{\pm}_{\mathbf{k}}$ as a function of T in detail in Sec. 3.13.

Finite temperature effects and/or screening removes this divergence. Our calculations with a simple screened interaction show that Sarma phases do become locally unstable at some region of the $r_s - \alpha$ plane which will be discussed in the next section.

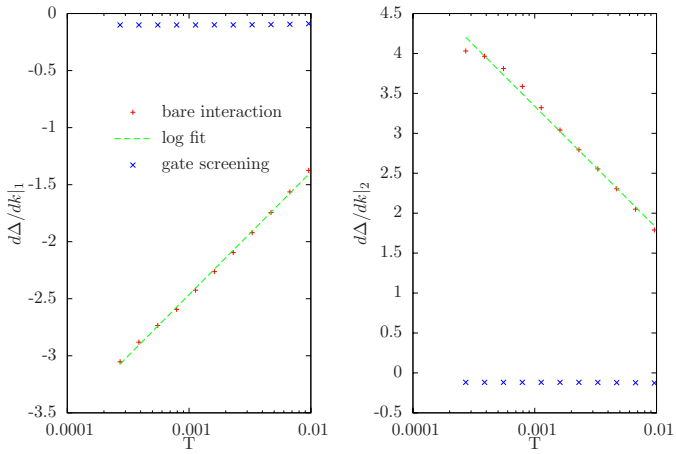

Figure 3.30: $d\Delta_{\mathbf{k}}/dk$ at the zero crossings of E_k^+, where the spikes develop in Fig.(3.29) marking the region of full occupation in the distribution function such as in in Fig.(3.11), as a function of decreasing temperature in units of effective Rydberg. The x-axis is logarithmic.

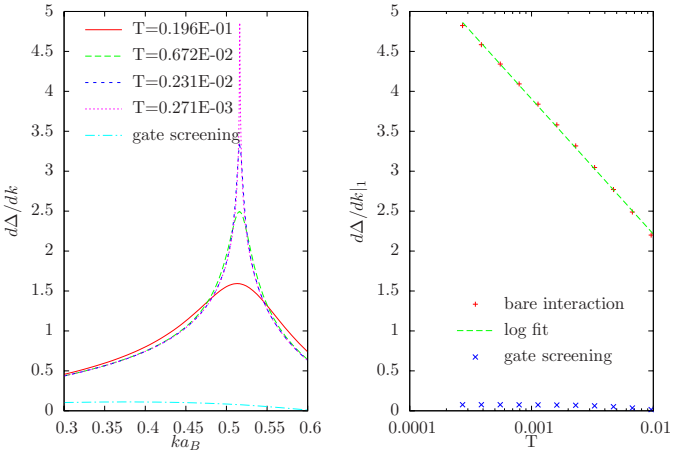

Figure 3.31: Sample plots showing the divergence of the derivative at the zero crossing of E_k^+ for $d = a_B, r_s = 3, \alpha = 0.3$ with no intra-layer interactions.

3.9 Phase Diagram at $d = a_B$

In this section we discuss the ensuing phase diagrams comparing the energy of the Sarma phases with the normal phase. We also consider the instability towards an FFLO phase. We set the inter-layer separation equal to one effective Bohr radius $d = a_B$ and study the phase diagram for the following four cases: (i) bare inter-layer interactions only, (ii) bare inter- and intra-layer interactions, (iii) screened inter-layer interactions only and (iv) screened inter- and intra-layer interactions.

The $\alpha = 0$ line is special in the phase diagram because it corresponds to the BCS state with equal layer densities.

For bare interactions, we find that the derivative of the gap at the zero crossings of the quasi-particle energy diverges at $T = 0$ which enters in the superfluid mass density calculation. The superfluid density is always positive and Sarma phase is always stable. Therefore, in the top panel of Fig. 3.32 we do not show any FFLO phase but our calculations do not rule out the presence of such a state with even lower energy. We show boundaries between the normal and Sarma phases. Two topologically different Sarma phases, Sarma 1 with one Fermi surface and Sarma 2 with two Fermi surfaces, are present in the phase diagrams. The effect of intra-layer interactions is to move the Normal-Sarma boundaries to lower density. The exchange interaction lowers the normal phase energy whereas the gap is not so much affected by intra-layer interactions and the energy is relatively similar. In the bottom panel of Fig. 3.32 the results are shown for the screened interaction. With inter-layer interactions only, the Sarma phase becomes unstable for a large portion of the phase diagram, especially with excess holes, i.e. $\alpha < 0$. (lower left panel) There is no stable S2 phase. The phase diagram including the intra-layer interactions has S2 phase stable in some region of the phase space and we end up with a rich phase diagram when both intra-layer and screening effects are present.

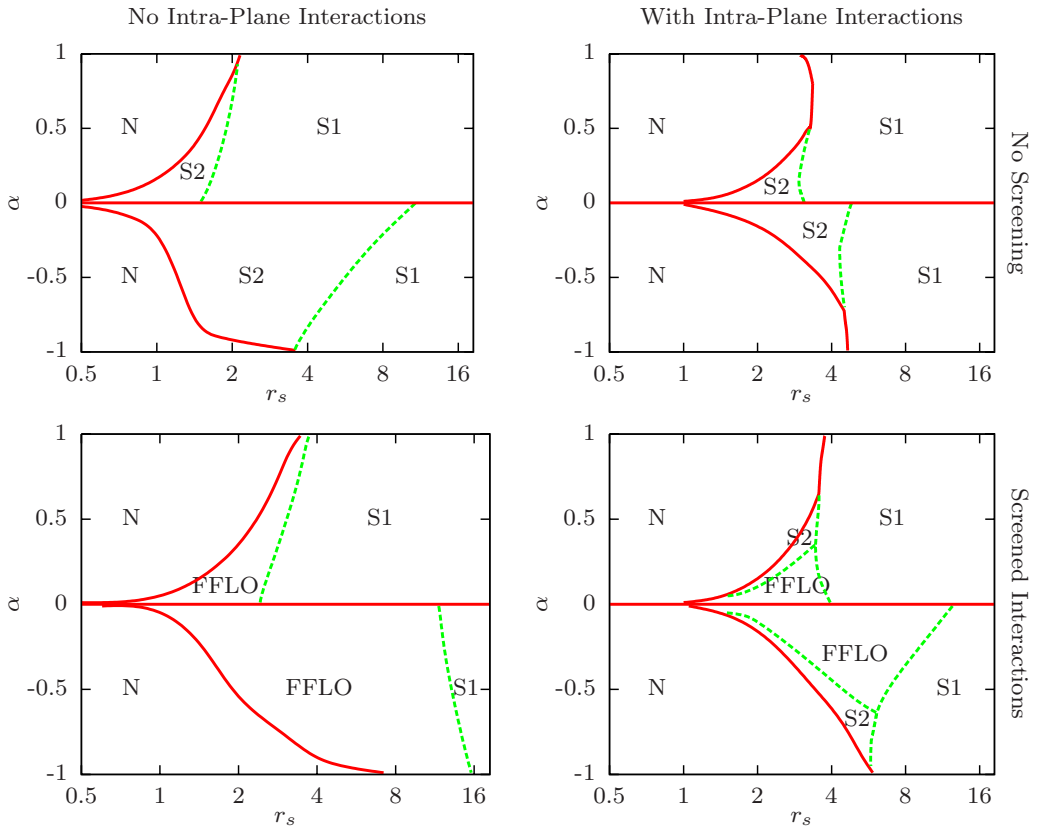

Figure 3.32: Phase diagrams for inter-layer separation $d = a_B$. Superfluid (S1/S2) - normal (N) phase boundaries are shown with red solid lines. A negative superfluid mass density showing a local instability is assumed to be towards an FFLO phase. S1, S2 and FFLO boundaries are shown with green dashed lines. The four cases shown are: Bare inter-layer interactions only (upper left panel), bare intra- and inter-layer interaction (upper right), gate screened inter-layer interactions only (lower left) and gate screened intra- and inter-layer interaction (lower right). $\alpha = 0$ line corresponds to the BCS state with equal populations.

3.10 Summary

We have studied exciton condensation in an electron-hole bilayer with population imbalance. Solving the mean-field gap equations we obtain the phase diagram for different electron and hole densities. The condensed Sarma phases are found to

be locally stable with bare Coulomb interactions which is very sensitive to finite temperature and screening effects. Introducing a simple screening model, we find that the some regions of phase space become unstable which we identify as an instability towards an FFLO state. We find a rich phase diagram in the crossover region with a possibility to observe the mentioned phases in the crossover regime corresponding to attainable densities and inter-plane separation with current experiments.

Appendix

3.11 Derivation of the Mean-Field Equations

We would like to determine the ground state with respect to the variational wave function

$$\begin{aligned} |\Psi\rangle &= \prod_{\mathbf{k}} (u_{\mathbf{k}}^p + v_{\mathbf{k}}^a \alpha_{\mathbf{k}}^\dagger + v_{\mathbf{k}}^b \beta_{-\mathbf{k}}^\dagger)(u_{\mathbf{k}} + v_{\mathbf{k}} a_{\mathbf{k}}^\dagger b_{-\mathbf{k}}^\dagger) \, |0\rangle \\ &= \prod_{\mathbf{k}} (u_{\mathbf{k}}^p + v_{\mathbf{k}}^a \alpha_{\mathbf{k}}^\dagger + v_{\mathbf{k}}^b \beta_{-\mathbf{k}}^\dagger) \, |\Psi_{BCS}\rangle \, . \end{aligned} \tag{3.33}$$

which is a slightly generalized form of the BCS wave function. Normalization is ensured by $|u_{\mathbf{k}}|^2 + |v_{\mathbf{k}}|^2 = 1$ and $|u_{\mathbf{k}}|^2 + |v_{\mathbf{k}}^a|^2 + |v_{\mathbf{k}}^b|^2 = 1$. Bogoluibov operators $\alpha_{\mathbf{k}}^\dagger$ and $\beta_{-\mathbf{k}}^\dagger$ defined below, create properly normalized states with particles and orthogonal to $|\Psi\rangle_{BCS}$ by acting on it. Instead of minimizing the energy at zero temperature, we consider a canonical ensemble of BCS and its excitations and minimize the free energy. This is the finite temperature BCS theory and gives the same results as with the above class of variational wave functions at zero temperature. Alternatively, the reduced BCS Hamiltonian can be diagonalized with a unitary transformation. The ground state gives the same wave function.

3.11.1 The Bogolioubov Transformation

It is convenient to introduce the Bogolioubov operators through the following *canonical* transformation

$$\alpha_{\mathbf{k}} = u_{\mathbf{k}} a_{\mathbf{k}} - v_{\mathbf{k}} b_{-\mathbf{k}}^\dagger \qquad \beta_{-\mathbf{k}} = u_{\mathbf{k}} b_{-\mathbf{k}} + v_{\mathbf{k}} a_{\mathbf{k}}^\dagger \tag{3.34}$$

$$\alpha_{\mathbf{k}}^\dagger = u_{\mathbf{k}}^* a_{\mathbf{k}}^\dagger - v_{\mathbf{k}}^* b_{-\mathbf{k}} \qquad \beta_{-\mathbf{k}}^\dagger = u_{\mathbf{k}}^* b_{-\mathbf{k}}^\dagger + v_{\mathbf{k}}^* a_{\mathbf{k}} \tag{3.35}$$

The inverse transformations are

$$a_{\mathbf{k}} = u_{\mathbf{k}}^* \alpha_{\mathbf{k}} + v_{\mathbf{k}} \beta_{-\mathbf{k}}^\dagger \qquad b_{-\mathbf{k}} = u_{\mathbf{k}}^* \beta_{-\mathbf{k}} - v_{\mathbf{k}} \alpha_{\mathbf{k}}^\dagger \tag{3.36}$$

$$a_{\mathbf{k}}^\dagger = u_{\mathbf{k}} \alpha_{\mathbf{k}}^\dagger + v_{\mathbf{k}}^* \beta_{-\mathbf{k}} \qquad b_{-\mathbf{k}}^\dagger = u_{\mathbf{k}} \beta_{-\mathbf{k}}^\dagger - v_{\mathbf{k}}^* \alpha_{\mathbf{k}} \tag{3.37}$$

The BCS state written in Eq.(3.33) is the vacuum state for the Bogolioubov destruction operators.

$$\alpha_{\mathbf{k}} \left|\Psi_{BCS}\right\rangle = \beta_{\mathbf{k}} \left|\Psi_{BCS}\right\rangle = 0 \tag{3.38}$$

Together with the canonical commutation relations this property enables one to use Wick's theorem to calculate expectation values with respect to the BCS state easily.

3.11.2 Minimization

In this section we minimize

$$\langle \hat{F} \rangle = \langle \hat{H} \rangle - TS - \mu_a \langle \hat{N}_a \rangle - \mu_b \langle \hat{N}_b \rangle \tag{3.39}$$

with respect to the variational parameters. The entropy S for the variational class of states is given by

$$S = -k_B \sum_{\mathbf{k}\sigma} [f^\sigma_{\mathbf{k}} \ln f^\sigma_{\mathbf{k}} + (1 - f^\sigma_{\mathbf{k}}) \ln(1 - f^\sigma_{\mathbf{k}})] \tag{3.40}$$

where $f^\pm_{\mathbf{k}}$ are the average occupation numbers of excitations of wave number $\mathbf{k}$ which are taken to be independent.

The expectation value of the Hamiltonian can be written as

$$\begin{aligned}
\langle \hat{H} \rangle \;=\; & \sum_{\mathbf{k}} (\epsilon^a_{\mathbf{k}} + \epsilon^b_{\mathbf{k}}) |v_{\mathbf{k}}|^2 (1 - f^+_{\mathbf{k}} - f^-_{\mathbf{k}}) + \sum_{\mathbf{k}} (\epsilon^a_{\mathbf{k}} f^+_{\mathbf{k}} + \epsilon^b_{\mathbf{k}} f^-_{\mathbf{k}}) \\
& + \frac{1}{V} \sum_{\mathbf{k}\mathbf{k}'}{}' U^{ab}_{\mathbf{q}} u_{\mathbf{k}} v^*_{\mathbf{k}} u^*_{\mathbf{k}'} v_{\mathbf{k}'} (1 - f^+_{\mathbf{k}} - f^-_{\mathbf{k}})(1 - f^+_{\mathbf{k}'} - f^-_{\mathbf{k}'}) \\
& - \frac{1}{2V} \sum_{\mathbf{k}\mathbf{k}'}{}' U^{aa}_{\mathbf{q}} |v_{\mathbf{k}}|^2 |v_{\mathbf{k}'}|^2 (1 - f^+_{\mathbf{k}} - f^-_{\mathbf{k}})(1 - f^+_{\mathbf{k}'} - f^-_{\mathbf{k}'}) \\
& - \frac{1}{2V} \sum_{\mathbf{k}\mathbf{k}'}{}' U^{aa}_{\mathbf{q}} 2 |v_{\mathbf{k}}|^2 (1 - f^+_{\mathbf{k}} - f^-_{\mathbf{k}}) f^+_{\mathbf{k}'} - \frac{1}{2V} \sum_{\mathbf{k}\mathbf{k}'}{}' U^{aa}_{\mathbf{q}} f^+_{\mathbf{k}} f^+_{\mathbf{k}'} \\
& - \frac{1}{2V} \sum_{\mathbf{k}\mathbf{k}'}{}' U^{bb}_{\mathbf{q}} |v_{\mathbf{k}}|^2 |v_{\mathbf{k}'}|^2 (1 - f^+_{\mathbf{k}} - f^-_{\mathbf{k}})(1 - f^+_{\mathbf{k}'} - f^-_{\mathbf{k}'}) \\
& - \frac{1}{2V} \sum_{\mathbf{k}\mathbf{k}'}{}' U^{bb}_{\mathbf{q}} 2 |v_{\mathbf{k}}|^2 (1 - f^+_{\mathbf{k}} - f^-_{\mathbf{k}}) f^-_{\mathbf{k}'} - \frac{1}{2V} \sum_{\mathbf{k}\mathbf{k}'}{}' U^{bb}_{\mathbf{q}} f^-_{\mathbf{k}} f^-_{\mathbf{k}'}
\end{aligned} \tag{3.41}$$

where we assume overall charge neutrality in the system, through additional uniformly charged layers, thus the primed summations are with $\mathbf{q} = \mathbf{k} - \mathbf{k}' \neq 0$ and furthermore we drop the constant Hartree energy stored in the electric field between the bilayer system and uniformly charged neutralizing layers. This energy can be absorbed in the definition of chemical potentials.

Now we take $u_{\mathbf{k}}$'s and $v_{\mathbf{k}}$'s to be real numbers and write

$$u_k = \cos\theta_{\mathbf{k}}, \qquad v_{\mathbf{k}} = \sin\theta_{\mathbf{k}} \tag{3.42}$$

and define the following

$$2\xi^+_{\mathbf{k}} = \xi^a_{\mathbf{k}} + \xi^b_{\mathbf{k}} \qquad 2\mu = \mu_a + \mu_b \tag{3.43}$$

$$2\xi^-_{\mathbf{k}} = \xi^a_{\mathbf{k}} + \xi^b_{\mathbf{k}} \qquad 2h = \mu_a - \mu_b \tag{3.44}$$

so that the free energy can be written as

$$\begin{aligned}
\langle \hat{F} \rangle = & \sum_{\mathbf{k}} 2\xi^+_{\mathbf{k}} \sin^2\theta_{\mathbf{k}}(1 - f^+_{\mathbf{k}} - f^-_{\mathbf{k}}) + \sum_{\mathbf{k}} (f^+_{\mathbf{k}}\xi^a_{\mathbf{k}} + f^-_{\mathbf{k}}\xi^b_{\mathbf{k}}) \\
& + \frac{1}{4V}\sum_{\mathbf{k}\mathbf{k}'} U^{ab}_{\mathbf{k}\mathbf{k}'} \sin 2\theta_{\mathbf{k}} \sin 2\theta_{\mathbf{k}'}(1 - f^+_{\mathbf{k}} - f^-_{\mathbf{k}})(1 - f^+_{\mathbf{k}'} - f^-_{\mathbf{k}'}) \\
& - \frac{1}{V}\sum_{\mathbf{k}\mathbf{k}'} U^{aa}_{\mathbf{k}\mathbf{k}'} \sin^2\theta_{\mathbf{k}} \sin^2\theta_{\mathbf{k}'}(1 - f^+_{\mathbf{k}} - f^-_{\mathbf{k}})(1 - f^+_{\mathbf{k}'} - f^-_{\mathbf{k}'}) \\
& - \frac{1}{V}\sum_{\mathbf{k}\mathbf{k}'} U^{aa}_{\mathbf{k}\mathbf{k}'} \sin^2\theta_{\mathbf{k}}(1 - f^+_{\mathbf{k}} - f^-_{\mathbf{k}})(f^+_{\mathbf{k}'} + f^-_{\mathbf{k}'}) \\
& - \frac{1}{2V}\sum_{\mathbf{k}\mathbf{k}'} U^{aa}_{\mathbf{k}\mathbf{k}'}(f^+_{\mathbf{k}} f^+_{\mathbf{k}'} + f^-_{\mathbf{k}} f^-_{\mathbf{k}'}) \\
& + \frac{1}{\beta}\sum_{\mathbf{k}} \left[f^+_{\mathbf{k}} \ln f^+_{\mathbf{k}} + (1 - f^+_{\mathbf{k}}) \ln(1 - f^+_{\mathbf{k}}) \right] \\
& + \frac{1}{\beta}\sum_{\mathbf{k}} \left[f^-_{\mathbf{k}} \ln f^-_{\mathbf{k}} + (1 - f^-_{\mathbf{k}}) \ln(1 - f^-_{\mathbf{k}}) \right]
\end{aligned} \tag{3.45}$$

Minimizing with respect to $\theta_{\mathbf{k}}$ gives

$$\begin{aligned}
\Bigg[\left(2\xi^+_{\mathbf{k}} - \frac{1}{V}\sum_{\mathbf{k}'}{}' U^{aa}_{\mathbf{k}\mathbf{k}'} 2\sin^2\theta_{\mathbf{k}'}(1 - f^+_{\mathbf{k}'} - f^-_{\mathbf{k}'}) - \frac{1}{V}\sum_{\mathbf{k}'}{}' U^{aa}_{\mathbf{k}\mathbf{k}'}(f^+_{\mathbf{k}'} + f^-_{\mathbf{k}'}) \right) \sin 2\theta_{\mathbf{k}} \\
+ \left(\frac{1}{V}\sum_{\mathbf{k}'}{}' U^{ab}_{\mathbf{k}\mathbf{k}'} 2\sin 2\theta_{\mathbf{k}'}(1 - f^+_{\mathbf{k}'} - f^-_{\mathbf{k}'}) \right) \cos 2\theta_{\mathbf{k}} \Bigg] (1 - f^+_{\mathbf{k}} - f^-_{\mathbf{k}}) = 0
\end{aligned} \tag{3.46}$$

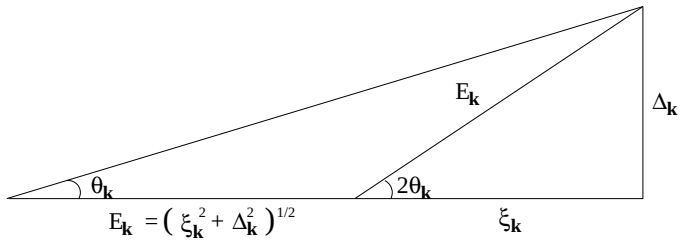

Figure 3.33: Relations between $\Delta_{\mathbf{k}}$, $\xi_{\mathbf{k}}$, $E_{\mathbf{k}}$, $\sin 2\theta_{\mathbf{k}}$ and $\sin\theta_{\mathbf{k}}$.

which can be written as

$$\tan 2\theta_{\mathbf{k}} = \frac{-\frac{1}{2V}\sum_{\mathbf{k}'}{}'U^{ab}_{\mathbf{k}\mathbf{k}'}\sin 2\theta_{\mathbf{k}'}(1-f^+_{\mathbf{k}'}-f^-_{\mathbf{k}'})}{\xi^+_{\mathbf{k}}-\frac{1}{2V}\sum_{\mathbf{k}'}{}'U^{aa}_{\mathbf{k}\mathbf{k}'}\left[2\sin^2\theta_{\mathbf{k}'}(1-f^+_{\mathbf{k}'}-f^-_{\mathbf{k}'})+f^+_{\mathbf{k}'}+f^-_{\mathbf{k}'}\right]} \equiv \frac{\Delta_{\mathbf{k}}}{\xi_{\mathbf{k}}} \quad (3.47)$$

It follows that

$$\sin 2\theta_{\mathbf{k}} = \frac{\Delta_{\mathbf{k}}}{(\xi^2_{\mathbf{k}}+\Delta^2_{\mathbf{k}})^{1/2}} \equiv \frac{\Delta_{\mathbf{k}}}{E_{\mathbf{k}}} \quad (3.48)$$

and

$$\sin^2\theta_{\mathbf{k}} = \frac{\Delta^2_{\mathbf{k}}}{2(\Delta^2_{\mathbf{k}}+\xi^2_{\mathbf{k}}+\xi_{\mathbf{k}}E_{\mathbf{k}})} = \frac{1}{2}(1-\frac{\xi_{\mathbf{k}}}{E_{\mathbf{k}}}) \quad (3.49)$$

with $\xi^2_{\mathbf{k}}+\Delta^2_{\mathbf{k}} = E^2_{\mathbf{k}}$.

Imposing $\partial\langle\hat{F}\rangle/\partial f^+_{\mathbf{k}} = 0$

$$\begin{aligned}
\frac{\partial\langle\hat{F}\rangle}{\partial f^+_{\mathbf{k}}} &= -2\xi^+_{\mathbf{k}}\sin^2\theta_{\mathbf{k}} + \xi^a_{\mathbf{k}} - \frac{1}{2V}\sum_{\mathbf{k}'}{}'U^{ab}_{\mathbf{k}\mathbf{k}'}\sin 2\theta_{\mathbf{k}'}(1-f^+_{\mathbf{k}'}-f^-_{\mathbf{k}'})\sin 2\theta_{\mathbf{k}} \\
&\quad + \frac{1}{V}\sum_{\mathbf{k}'}{}'U^{aa}_{\mathbf{k}\mathbf{k}'}2\sin^2\theta_{\mathbf{k}'}(1-f^+_{\mathbf{k}'}-f^-_{\mathbf{k}'})\sin^2\theta_{\mathbf{k}} + \frac{1}{V}\sum_{\mathbf{k}'}{}'U^{aa}_{\mathbf{k}\mathbf{k}'}(f^+_{\mathbf{k}'}+f^-_{\mathbf{k}'})\sin^2\theta_{\mathbf{k}} \\
&\quad - \frac{1}{V}\sum_{\mathbf{k}'}{}'U^{aa}_{\mathbf{k}\mathbf{k}'}\sin^2\theta_{\mathbf{k}'}(1-f^+_{\mathbf{k}'}-f^-_{\mathbf{k}'}) - \frac{1}{V}\sum_{\mathbf{k}'}{}'U^{aa}_{\mathbf{k}\mathbf{k}'}f^+_{\mathbf{k}'} \\
&\quad + \frac{1}{\beta}\left[\ln f^+_{\mathbf{k}} + 1 - \ln(1-f^+_{\mathbf{k}}) - 1\right] = 0 \\
-\ln\left(\frac{f^+_{\mathbf{k}}}{1-f^+_{\mathbf{k}}}\right) &= \beta\left[E_{\mathbf{k}} + \xi^-_{\mathbf{k}} + \frac{1}{2V}\sum_{\mathbf{k}'}{}'U^{aa}_{\mathbf{k}\mathbf{k}'}(f^-_{\mathbf{k}'}-f^+_{\mathbf{k}'})\right] \equiv \beta(E_{\mathbf{k}}+\Delta E_{\mathbf{k}}) \equiv \beta E^+_{\mathbf{k}} \quad (3.50)
\end{aligned}$$

Similarly minimizing with respect to $f^-_{\mathbf{k}}$ we find

$$f^-_{\mathbf{k}} = \frac{1}{e^{\beta E^-_{\mathbf{k}}}+1}, \qquad E^-_{\mathbf{k}} = E_{\mathbf{k}} - \Delta E_{\mathbf{k}} \quad (3.51)$$

With the above definitions the coupled gap equations are

$$\Delta_{\mathbf{k}} = -\frac{1}{V}\sum_{\mathbf{k}'}{}'U^{ab}_{\mathbf{k}\mathbf{k}'}\frac{\Delta_{\mathbf{k}'}}{2E_{\mathbf{k}'}}(1-f^+_{\mathbf{k}'}-f^-_{\mathbf{k}'}) \tag{3.52}$$

$$\xi_{\mathbf{k}} = \xi^+_{\mathbf{k}} - \frac{1}{2V}\sum_{\mathbf{k}'}{}'U^{aa}_{\mathbf{k}\mathbf{k}'}\left[1-\frac{\xi_{\mathbf{k}'}}{E_{\mathbf{k}'}}(1-f^+_{\mathbf{k}'}-f^-_{\mathbf{k}'})\right] \tag{3.53}$$

$$E^2_{\mathbf{k}} = \xi^2_{\mathbf{k}} + \Delta^2_{\mathbf{k}} \tag{3.54}$$

$$f^{\pm}_{\mathbf{k}} = \frac{1}{\mathrm{e}^{\beta E^{\pm}_{\mathbf{k}}}+1} \qquad \begin{array}{l} E^{\pm}_{\mathbf{k}} = E_{\mathbf{k}} \pm \Delta E_{\mathbf{k}} \\ \Delta E_{\mathbf{k}} = \xi^-_{\mathbf{k}} + \frac{1}{2V}\sum_{\mathbf{k}'}{}'U^{aa}_{\mathbf{k}\mathbf{k}'}(f^-_{\mathbf{k}'}-f^+_{\mathbf{k}'}) \end{array} \tag{3.55}$$

3.12 Scaling

We work in units where length is measured in effective Bohr radius a_B, momentum in $1/a_B$ and energy in Rydberg. Let us denote dimensionless quantities with a tilde sign. The quantities introduced earlier can be rewritten in a form suitable for numerical calculation in the following way.

$$\begin{aligned} 2\xi^+_{\mathbf{k}} &= \xi^a_{\mathbf{k}} + \xi^b_{\mathbf{k}} \\ &= \frac{\hbar^2}{2}\left(\frac{1}{m_a}+\frac{1}{m_b}\right)k^2 - (\mu_a+\mu_b) \\ &= \frac{\hbar^2 k^2}{2m} - 2\mu \\ \widetilde{\xi^+_{\mathbf{k}}} &= \frac{1}{2}\widetilde{k}^2 - \widetilde{\mu} \equiv \widetilde{\epsilon}_{\mathbf{k}} - \widetilde{\mu} \end{aligned}$$

where $\widetilde{k} = ka_B$ and $\widetilde{\xi^+_{\mathbf{k}}}$ and $\widetilde{\mu}$ are in units of Rydberg.

Similarly,

$$\begin{aligned} 2\xi^-_{\mathbf{k}} &= \xi^a_{\mathbf{k}} - \xi^b_{\mathbf{k}} \\ &= \frac{\hbar^2}{2}\left(\frac{1}{m_a}-\frac{1}{m_b}\right)k^2 - (\mu_a-\mu_b) \\ &= \frac{\hbar^2}{m}\frac{m}{2}\left(\frac{1}{m_a}-\frac{1}{m_b}\right)k^2 - 2h \\ \widetilde{\xi^-_{\mathbf{k}}} &= \frac{\beta-1}{\beta+1}\frac{\widetilde{k}^2}{2} - \widetilde{h}, \qquad \beta = m_b/m_a \end{aligned}$$

and the Coulomb potential becomes

$$\begin{aligned} U(r) &= \frac{e^2}{\varepsilon r} \\ \widetilde{U}(\widetilde{r}) &= \frac{1}{\widetilde{r}}. \end{aligned}$$

The dimensionless expressions for the the average inter particle spacing in terms of Bohr radius r_s related to the average density per plane and population polarization α related to the density difference are

$$n = \frac{1}{2}(n_a + n_b) = \frac{1}{\pi a_B^2 r_s^2} \qquad \text{and} \qquad \widetilde{n} = \frac{1}{\pi r_s^2} \tag{3.56}$$

$$\alpha = \frac{n_a - n_b}{n_a + n_b} = \frac{\widetilde{n}_a - \widetilde{n}_b}{\widetilde{n}_a + \widetilde{n}_b} \tag{3.57}$$

3.12.1 Numerical Evaluation of Wave Vector Sums

The $\mathbf{k}$ sums in the gap equations pose two numerical difficulties at $T = 0$. The Coulomb potential is singular at $|\mathbf{k} - \mathbf{k}'| = 0$. We treat this singularity carefully using the following trick of introducing an exponential cut. The second difficulty arises from the fact that at $T = 0$ the distribution functions become step functions and the integrand becomes discontinuous. We evaluate the integrals using Gaussian quadrature and to handle the discontinuity we break up the integration grid in to two or tree pieces.

Singularity of the Coulomb Potential

The gap equations involve sums of the form

$$U = \sum_{\mathbf{q}} \frac{1}{|\mathbf{q} - \mathbf{k}|} F(q) \qquad \text{and} \qquad U_2 = \sum_{\mathbf{q}} \frac{\mathrm{e}^{-|\mathbf{q}-\mathbf{k}|d}}{|\mathbf{q} - \mathbf{k}|} F(q) \tag{3.58}$$

where $F(q)$ is a nonsingular function of q. Here the sums U and U_2 are functions of k. The first sum U above can be related to the second one.

$$\begin{aligned} U &= \sum_{\mathbf{q}} \frac{1}{|\mathbf{q}-\mathbf{k}|} F(q) \\ &= \sum_{\mathbf{q}} \frac{1}{|\mathbf{q}-\mathbf{k}|} \left(1 - \mathrm{e}^{-|\mathbf{q}-\mathbf{k}|d}\right) F(q) + \sum_{\mathbf{q}} \frac{1}{|\mathbf{q}-\mathbf{k}|} \mathrm{e}^{-|\mathbf{q}-\mathbf{k}|d} F(q) \\ &= U_1 + U_2 \end{aligned} \tag{3.59}$$

where U_1 does not have a singularity and can be calculated as an integral in the thermodynamic limit using $\sum_{\mathbf{k}} \to \int \frac{\mathrm{d}^2 k}{(2\pi)^2}$,

$$\begin{aligned} U_1 &= \sum_{\mathbf{q}} \frac{1}{|\mathbf{q}-\mathbf{k}|} \left(1 - \mathrm{e}^{-|\mathbf{q}-\mathbf{k}|d}\right) F(q) \\ U_1 &= \frac{1}{4\pi^2} \int_0^\infty q \mathrm{d}q \, F(q) \int_0^{2\pi} \mathrm{d}\phi \, \frac{\left(1 - \mathrm{e}^{-|\mathbf{q}-\mathbf{k}|d}\right)}{|\mathbf{q}-\mathbf{k}|} \end{aligned} \tag{3.60}$$

Finally, we rewrite the problematic sum U_2 as

$$\begin{aligned} U_2 &= \sum_{\mathbf{q}} \frac{\mathrm{e}^{-|\mathbf{q}-\mathbf{k}|}}{|\mathbf{q}-\mathbf{k}|} F(q) \\ &= \sum_{\mathbf{q}\neq\mathbf{k}} \frac{\mathrm{e}^{-|\mathbf{q}-\mathbf{k}|}}{|\mathbf{q}-\mathbf{k}|} \left[F(q) - F(k)\right] + F(k) \sum_{\mathbf{q}} \frac{\mathrm{e}^{-|\mathbf{q}-\mathbf{k}|}}{|\mathbf{q}-\mathbf{k}|} \\ &= \sum_{\mathbf{q}\neq\mathbf{k}} \frac{\mathrm{e}^{-|\mathbf{q}-\mathbf{k}|}}{|\mathbf{q}-\mathbf{k}|} \Delta F(q,k) + F(k) T(r=0) \end{aligned} \tag{3.61}$$

where the sum does not involve $q = k$ and $T(r = 0)$ is the Fourier transform of $\mathrm{e}^{-|\mathbf{q}-\mathbf{k}|}/|\mathbf{q}-\mathbf{k}|$ at $r = 0$. Furthermore, we can express the remaining sum in terms of a similar integral for U_1 in the thermodynamic limit.

$$\begin{aligned} U_2 &= \frac{1}{4\pi^2} \int_0^\infty q \mathrm{d}q \, \Delta F(q,k) \int_0^{2\pi} \mathrm{d}\phi \, \left[\frac{\mathrm{e}^{-|\mathbf{q}-\mathbf{k}|} - 1}{|\mathbf{q}-\mathbf{k}|} - \frac{1}{|\mathbf{q}-\mathbf{k}|}\right] + F(k) T(0) \\ U_2 &= \frac{1}{4\pi^2} \int_0^\infty q \mathrm{d}q \, \Delta F(q,k) \left[\int_0^{2\pi} \mathrm{d}\phi \, \frac{\mathrm{e}^{-|\mathbf{q}-\mathbf{k}|} - 1}{|\mathbf{q}-\mathbf{k}|} - \frac{2}{k} K\left(\frac{q}{k}\right)\right] + F(k) T(0) \end{aligned} \tag{3.62}$$

where $K(q/k)$ is the complete elliptic integral of the first kind. Below we show why the angular integration is never carried out for $q = k$ case.

Numerical Integration

We evaluate integrals using Gaussian quadrature [123]. We approximate the integral by a weighted sum.

$$\int_0^\infty f(q)dq = \sum_i w_i f(q_i) \tag{3.63}$$

where q_i are the abscissae and w_i are the Gaussian weights. In fact the q_i make up the mesh points where functions of k are represented. In this way we obtain the results of the integrals at the mesh points.

$$\begin{aligned} U_1 &= \frac{1}{4\pi^2}\int_0^\infty q\mathrm{d}q\, F(q)\int_0^{2\pi}\mathrm{d}\phi\,\frac{\left(1-\mathrm{e}^{-|\mathbf{q}-\mathbf{k}|d}\right)}{|\mathbf{q}-\mathbf{k}|} \\ U_{1,j} &= \frac{1}{4\pi^2}\sum_i w_i q_i F(q_i)\int_0^{2\pi}\mathrm{d}\phi\,\frac{\left(1-\mathrm{e}^{-|\mathbf{q}_i-\mathbf{k}_j|d}\right)}{|\mathbf{q}_i-\mathbf{k}_j|} \end{aligned} \tag{3.64}$$

We can represent the results of the integral at grid points as a vector. The above equations can then be written in matrix form

$$\bar{U_1} = \bar{\bar{B}}_1\bar{F} \tag{3.65}$$

where the components of the vectors are $U_{1,i} = U_1(k_i)$ and $F_i = F(k_i)$ and the matrix elements are given by

$$U_{1,ij} = \frac{1}{4\pi^2}w_i q_i\int_0^{2\pi}\mathrm{d}\phi\,\frac{\left(1-\mathrm{e}^{-|\mathbf{q}_i-\mathbf{k}_j|d}\right)}{|\mathbf{q}_i-\mathbf{k}_j|} \tag{3.66}$$

Since we know that $U_{1,ii}$ vanish, we do not have to calculate them explicitly.

Similarly, for U_2 we have

$$\begin{aligned} U_2 &= \frac{1}{4\pi^2}\int_0^\infty q\mathrm{d}q\,\Delta F(q,k)\left[\int_0^{2\pi}\mathrm{d}\phi\,\frac{\mathrm{e}^{-|\mathbf{q}-\mathbf{k}|}-1}{|\mathbf{q}-\mathbf{k}|} - \frac{2}{k}K\left(\frac{q}{k}\right)\right] + F(k)T(0) \\ U_{2,j} &= \frac{1}{4\pi^2}\sum_i w_i q_i\Delta F(q_i,k_j)\left[\int_0^{2\pi}\mathrm{d}\phi\,\frac{\mathrm{e}^{-|\mathbf{q}_i-\mathbf{k}_j|}-1}{|\mathbf{q}-\mathbf{k}|} - \frac{2}{k_j}K\left(\frac{q_i}{k_j}\right)\right] + F(k_j)T(0) \end{aligned} \tag{3.67}$$

which can also be written as a vector equation.

The zero to infinity range for the radial q integration is in practice mapped to a finite interval using a tangent transformation.

$$q = q_0 \tan\theta \quad \text{and} \quad dq = \frac{q_0}{\cos^2\theta} d\theta \tag{3.68}$$

where q_0 is a scale factor and is put equal to 1.

Discontinuities for Population Imbalance at $T = 0$

At zero temperature the quasi-particle occupation numbers $f_{\mathbf{k}}^{\pm}$ become unity over a finite interval. The factors $(1-f_{\mathbf{k}}^{+}-f_{\mathbf{k}}^{-})$ are then zero over that interval and they do not contribute to the integral. The multiplication with step function results in discontinuities which is undesired with Gaussian integration. In order to calculate the integrals properly we identify the region at finite but small temperature and while decreasing the temperature we break up the integration grid into two or three parts such that the discontinuities are at the end points of the intervals. These are the zero crossings of one branch of $E_{\mathbf{k}}^{\pm}$. At each step the gap and quasi-particle energies are transferred to the new mesh using a cubic spline since lowering the temperature at each step moves the zero crossings.

For small r_s, the other length scale in the problem, which is k_F, becomes important. (typically for $r_s < 1$.) For this reason a finer grid around k_F becomes necessary for small r_s.

3.12.2 Initial Values

We start from the corresponding balanced situation solution for the same average density r_s which is obtained using the iterative method. We then introduce a small finite temperature and a chemical potential difference to create imbalance and lower the temperature until $f_{\mathbf{k}}^{\pm}$ distribution is a sharp step function and quantities do not depend on temperature.

3.12.3 Calculation of Energy

Using the definitions for $\Delta_{\mathbf{k}}, \Delta E_{\mathbf{k}}$, the energy expression can be reduced to a one dimensional integral which is useful for our numerical calculation.

$$\begin{aligned}\langle H\rangle =& \sum_{\mathbf{k}} \epsilon^{+}_{\mathbf{k}} \left(1 - \frac{\xi_{\mathbf{k}}}{E_{\mathbf{k}}}\right) + \sum_{\mathbf{k}} \epsilon^{a}_{\mathbf{k}} f^{+}_{\mathbf{k}} + \sum_{\mathbf{k}} \epsilon^{b}_{\mathbf{k}} f^{-}_{\mathbf{k}} \\ &+ \sum_{\mathbf{k}} \frac{1}{2}\frac{\Delta_{\mathbf{k}}}{E_{\mathbf{k}}} \left[\frac{1}{2V}\sum_{\mathbf{k}'} U^{ab}_{\mathbf{k}\mathbf{k}'} \frac{\Delta_{\mathbf{k}'}}{E_{\mathbf{k}'}} \left(1 - f^{+}_{\mathbf{k}'} - f^{-}_{\mathbf{k}'}\right)\right] \left(1 - f^{+}_{\mathbf{k}} - f^{-}_{\mathbf{k}}\right) \\ &- \sum_{\mathbf{k}} \frac{1}{2}\left(1 - \frac{\xi_{\mathbf{k}}}{E_{\mathbf{k}}}\right) \left[\frac{1}{2V}\sum_{\mathbf{k}'} U^{aa}_{\mathbf{k}\mathbf{k}'} \left(1 - \frac{\xi_{\mathbf{k}'}}{E_{\mathbf{k}'}}\right) \left(1 - f^{+}_{\mathbf{k}'} - f^{-}_{\mathbf{k}'}\right)\right] \left(1 - f^{+}_{\mathbf{k}} - f^{-}_{\mathbf{k}}\right) \\ &- \sum_{\mathbf{k}} \frac{1}{2}\left(1 - \frac{\xi_{\mathbf{k}}}{E_{\mathbf{k}}}\right) \left(\frac{1}{2V} + \frac{1}{2V}\right) \left[\sum_{\mathbf{k}'} U^{aa}_{\mathbf{k}\mathbf{k}'} \left(f^{+}_{\mathbf{k}'} + f^{-}_{\mathbf{k}'}\right)\right] \left(1 - f^{+}_{\mathbf{k}} - f^{-}_{\mathbf{k}}\right) \\ &- \sum_{\mathbf{k}} \left[\frac{1}{2V}\sum_{\mathbf{k}'} U^{aa}_{\mathbf{k}\mathbf{k}'} f^{+}_{\mathbf{k}'}\right] f^{+}_{\mathbf{k}} - \sum_{\mathbf{k}} \left[\frac{1}{2V}\sum_{\mathbf{k}'} U^{aa}_{\mathbf{k}\mathbf{k}'} f^{-}_{\mathbf{k}'}\right] f^{-}_{\mathbf{k}}\end{aligned} \tag{3.69}$$

where $\epsilon^{+}_{\mathbf{k}} = (\epsilon^{a}_{\mathbf{k}} + \epsilon^{b}_{\mathbf{k}})/2$. Next we group these terms for contributions coming from the condensate, unpaired electrons and unpaired holes and simplify the first double sum using the definition of $\Delta_{\mathbf{k}}$.

$$\begin{aligned}\langle H\rangle =& \sum_{\mathbf{k}} \left[\left(\epsilon^{+}_{\mathbf{k}} + \frac{1}{2}\left(\xi_{\mathbf{k}} - \xi^{+}_{\mathbf{k}}\right)\right)\left(1 - \frac{\xi_{\mathbf{k}}}{E_{\mathbf{k}}}\right) - \frac{1}{2}\frac{\Delta^2_{\mathbf{k}}}{E_{\mathbf{k}}}\right]\left(1 - f^{+}_{\mathbf{k}} - f^{-}_{\mathbf{k}}\right) \\ &+ \sum_{\mathbf{k}} \left[\epsilon^{a}_{\mathbf{k}} - \frac{1}{4V}\sum_{\mathbf{k}'} U^{aa}_{\mathbf{k}\mathbf{k}'} \left\{\left(1 - \frac{\xi_{\mathbf{k}'}}{E_{\mathbf{k}'}}\right)\left(1 - f^{+}_{\mathbf{k}'} - f^{-}_{\mathbf{k}'}\right) + 2f^{+}_{\mathbf{k}'}\right\}\right] f^{+}_{\mathbf{k}} \\ &+ \sum_{\mathbf{k}} \left[\epsilon^{b}_{\mathbf{k}} - \frac{1}{4V}\sum_{\mathbf{k}'} U^{aa}_{\mathbf{k}\mathbf{k}'} \left\{\left(1 - \frac{\xi_{\mathbf{k}'}}{E_{\mathbf{k}'}}\right)\left(1 - f^{+}_{\mathbf{k}'} - f^{-}_{\mathbf{k}'}\right) + 2f^{-}_{\mathbf{k}'}\right\}\right] f^{-}_{\mathbf{k}}\end{aligned} \tag{3.70}$$

Finally, we eliminate the remaining $\mathbf{k}'$ sums using the definition of $\Delta E_{\mathbf{k}}$.

$$\begin{aligned}\langle H\rangle =&\frac{1}{2}\sum_{\mathbf{k}}\left[\left(2\epsilon^{+}_{\mathbf{k}}+\xi_{\mathbf{k}}-\xi^{+}_{\mathbf{k}}\right)\left(1-\frac{\xi_{\mathbf{k}}}{E_{\mathbf{k}}}\right)-\frac{\Delta^2_{\mathbf{k}}}{E_{\mathbf{k}}}\right]\left(1-f^{+}_{\mathbf{k}}-f^{-}_{\mathbf{k}}\right)\\&+\frac{1}{2}\sum_{\mathbf{k}}\left[2\epsilon^{a}_{\mathbf{k}}+\xi_{\mathbf{k}}-\xi^{+}_{\mathbf{k}}-\xi^{-}_{\mathbf{k}}+\Delta E_{\mathbf{k}}\right]f^{+}_{\mathbf{k}}\\&+\frac{1}{2}\sum_{\mathbf{k}}\left[2\epsilon^{b}_{\mathbf{k}}+\xi_{\mathbf{k}}-\xi^{+}_{\mathbf{k}}+\xi^{-}_{\mathbf{k}}-\Delta E_{\mathbf{k}}\right]f^{-}_{\mathbf{k}}\end{aligned}\tag{3.71}$$

which can also be expressed as

$$\begin{aligned}\langle H\rangle =&\frac{1}{2}\sum_{\mathbf{k}}\left[\left(\epsilon^{+}_{\mathbf{k}}+\mu+\xi_{\mathbf{k}}\right)\left(1-\frac{\xi_{\mathbf{k}}}{E_{\mathbf{k}}}\right)-\frac{\Delta^2_{\mathbf{k}}}{E_{\mathbf{k}}}\right]\left(1-f^{+}_{\mathbf{k}}-f^{-}_{\mathbf{k}}\right)\\&+\frac{1}{2}\sum_{\mathbf{k}}\left[2\epsilon^{+}_{\mathbf{k}}+2\epsilon^{-}_{\mathbf{k}}+\xi_{\mathbf{k}}-\xi^{+}_{\mathbf{k}}-\xi^{-}_{\mathbf{k}}+\Delta E_{\mathbf{k}}\right]f^{+}_{\mathbf{k}}\\&+\frac{1}{2}\sum_{\mathbf{k}}\left[2\epsilon^{+}_{\mathbf{k}}-2\epsilon^{-}_{\mathbf{k}}+\xi_{\mathbf{k}}-\xi^{+}_{\mathbf{k}}+\xi^{-}_{\mathbf{k}}-\Delta E_{\mathbf{k}}\right]f^{-}_{\mathbf{k}}\end{aligned}\tag{3.72}$$

or as

$$\begin{aligned}\langle H\rangle =&\frac{1}{2}\sum_{\mathbf{k}}\left[\left(\xi^{+}_{\mathbf{k}}+2\mu+\xi_{\mathbf{k}}\right)\left(1-\frac{\xi_{\mathbf{k}}}{E_{\mathbf{k}}}\right)-\frac{\Delta^2_{\mathbf{k}}}{E_{\mathbf{k}}}\right]\left(1-f^{+}_{\mathbf{k}}-f^{-}_{\mathbf{k}}\right)\\&+\frac{1}{2}\sum_{\mathbf{k}}\left[\xi^{+}_{\mathbf{k}}+2\mu+\xi_{\mathbf{k}}+\xi^{-}_{\mathbf{k}}+2h+\Delta E_{\mathbf{k}}\right]f^{+}_{\mathbf{k}}\\&+\frac{1}{2}\sum_{\mathbf{k}}\left[\xi^{+}_{\mathbf{k}}+2\mu+\xi_{\mathbf{k}}-\xi^{-}_{\mathbf{k}}-2h-\Delta E_{\mathbf{k}}\right]f^{-}_{\mathbf{k}}\end{aligned}\tag{3.73}$$

in terms of quantities appearing in the gap equations.

3.13 Analysis of $\mathrm{d}\Delta_{\mathbf{k}}/\mathrm{d}k$ at Zero Crossings of $E^{\pm}_{\mathbf{k}}$

The value of the quantity $\mathrm{d}E^{\pm}_{\mathbf{k}}/\mathrm{d}k$ at zero crossings of $E^{\pm}_{\mathbf{k}}$ is important in the calculation of the superfluid mass density ρ_s at $T=0$. Here we study the behavior of the the derivative $\mathrm{d}E^{\pm}_{\mathbf{k}}/\mathrm{d}k$ at $k=k^*$, the zero crossings of $E^{\pm}_{\mathbf{k}}$, in the bilayer system. We show that this quantity diverges logarithmically at $k=k^*$ as $T\to 0$

and as $k \to k^*$ at $T = 0$ for the bare Coulomb interaction. This divergence is due to a corresponding divergence of $\mathrm{d}\Delta_{\mathbf{k}}/\mathrm{d}k$, where $\Delta_{\mathbf{k}}$ is the solution of the gap equation:

$$\Delta_{\mathbf{k}} = -\int \frac{\mathrm{d}^2k'}{(2\pi)^2} U^{eh}_{\mathbf{k},\mathbf{k}'} \frac{\Delta_{\mathbf{k}'}}{2E_{\mathbf{k}'}} \left[1 - f(E^+_{\mathbf{k}'}) - f(E^-_{\mathbf{k}'})\right] \tag{3.74}$$

$$= -\frac{1}{2\pi}\int_0^\infty k'\mathrm{d}k' \left\{ \bar{U}^{eh}(k,k') \frac{\Delta_{\mathbf{k}'}}{2E_{\mathbf{k}'}} \left[1 - f(E^+_{\mathbf{k}'}) - f(E^-_{\mathbf{k}'})\right] \right\} \tag{3.75}$$

where we have introduced the angle-averaged potential energy

$$\bar{U}^{eh}(k,k') = \frac{1}{2\pi}\int_{-\pi}^{\pi} \mathrm{d}\theta\, U^{eh}\left(\sqrt{k^2 + k'^2 - 2kk'\cos\theta}\right) \tag{3.76}$$

We use two interaction potentials as given before. One is the bare Coulomb interaction

$$U^{eh}(\mathbf{q}) = -2\pi\frac{e^2}{\varepsilon}\frac{\mathrm{e}^{-qd}}{q} \tag{3.77}$$

and the second is Coulomb interaction with simple model gate screening

$$U^{eh}(\mathbf{q}) = -2\pi\frac{e^2}{\varepsilon}\frac{\mathrm{e}^{-qd}}{\sqrt{q^2 + q_0^2}} \tag{3.78}$$

where q_0 is a momentum cut-off.

A preliminary step in the analysis of the behavior of $\mathrm{d}\Delta_{\mathbf{k}}/\mathrm{d}k$ is the study of $\bar{U}^{eh}(k,k')$ as $k \to k'$. The unscreened potential $\bar{U}^{eh}(k,k')$ diverges logarithmically as $k \to k'$. The screening cures this divergence. Let us consider then the leading behavior of

$$\bar{U}^{eh}(k, k+\delta k) = -\frac{e^2}{\varepsilon}\times \int_{-\pi}^{\pi} \mathrm{d}\theta \frac{\exp\left[-d\sqrt{k^2 + k^2 + 2k\delta k + (\delta k)^2 - 2k^2\cos\theta - 2k\delta k\cos\theta}\right]}{\left[2k^2 + 2k\delta k + (\delta k)^2 - 2k^2\cos\theta - 2k\delta k\cos\theta + q_0^2\right]^{1/2}} \tag{3.79}$$

We are interested in the "irregular" part of this integral which arises from the vanishing of the denominator in the above integral when $q_0 = 0$ for $\delta k \to 0$ and

$\theta \to 0$. The numerator is regular and we can thus set $\delta k = 0$ and $\theta = 0$ there. We have [3]

$$\bar{U}^{irreg}(k, k+\delta k) = -\frac{e^2}{\varepsilon}\int_{-\pi}^{\pi} \mathrm{d}\theta \, \frac{1}{\left[(2k^2 + 2k\delta k)(1-\cos\theta) + (\delta k)^2 + q_0^2\right]^{1/2}} \quad (3.80)$$

We can expand $\cos\theta$ about the origin as a Taylor series since the divergence arises for $\theta \to 0$. Let $\theta_0 \ll 1$ such that $\cos\theta \approx 1 - \theta^2/2$. Then

$$\begin{aligned}
\bar{U}^{irreg}(k, k+\delta k) &\approx -\frac{e^2}{\varepsilon}\int_{-\theta_0}^{\theta_0} \mathrm{d}\theta \, \frac{1}{\left[(k^2 + k\delta k)\theta^2 + (\delta k)^2 + q_0^2\right]^{1/2}} \\
&\approx -\frac{2e^2}{\varepsilon}\int_{0}^{\theta_0} \mathrm{d}\theta \, \frac{1}{\left[k^2\theta^2 + (\delta k)^2 + q_0^2\right]^{1/2}} \\
&\approx -\frac{2e^2}{\varepsilon}\int_{0}^{\theta_0} \frac{\mathrm{d}\theta}{\sqrt{(\delta k)^2 + q_0^2}} \, \frac{1}{\left[\left(k\theta/\sqrt{(\delta k)^2 + q_0^2}\right)^2 + 1\right]^{1/2}} \\
&\approx -\frac{2e^2}{\varepsilon k}\int_{0}^{k\theta_0/\sqrt{(\delta k)^2+q_0^2}} \mathrm{d}x \, \frac{1}{\sqrt{x^2+1}}
\end{aligned}$$

When both δk and q_0 are small we find

$$\bar{U}^{irreg}(k, k+\delta k) \approx -\frac{2e^2}{\varepsilon k}\sinh^{-1}\left(\frac{k\theta_0}{\sqrt{(\delta k)^2 + q_0^2}}\right) \quad (3.81)$$

$$\approx -\frac{2e^2}{\varepsilon k}\ln\left(\frac{2k\theta_0}{\sqrt{(\delta k)^2 + q_0^2}}\right) \quad (3.82)$$

where we have assumed $\sqrt{(\delta k)^2 + q_0^2} \ll k\theta_0$, which can always be satisfied for sufficiently small q_0 and δk.

We now move on to calculate $\mathrm{d}\Delta_{\mathbf{k}}/\mathrm{d}k$. Differentiating Eq. 3.75 with respect to k, we obtain

$$\frac{\mathrm{d}\Delta_{\mathbf{k}}}{\mathrm{d}k} = -\frac{1}{2\pi}\int_0^{\infty} k'\mathrm{d}k' \left\{\frac{\partial}{\partial k}\bar{U}^{eh}(k,k')\frac{\Delta_{\mathbf{k}'}}{2E_{\mathbf{k}'}}\left[1 - f(E^+_{\mathbf{k}'}) - f(E^-_{\mathbf{k}'})\right]\right\} \quad (3.83)$$

Using

$$\frac{\partial}{\partial k}\bar{U}^{irreg}(k,k') \approx -\frac{\partial}{\partial k'}\bar{U}^{irreg}(k,k') \quad (3.84)$$

[3]Note that $\bar{U}^{irreg}$ is just the angle averaged Coulomb potential in the plane.

when $k \approx k'$, we have

$$\frac{\mathrm{d}\Delta_{\mathbf{k}}}{\mathrm{d}k} \approx \frac{1}{2\pi}\int_0^\infty k' \frac{\Delta_{\mathbf{k}'}}{2E_{\mathbf{k}'}}\left[1 - f(E^+_{\mathbf{k}'}) - f(E^-_{\mathbf{k}'})\right]\frac{\partial}{\partial k'}\bar{U}^{irreg}(k,k')\,\mathrm{d}k' \tag{3.85}$$

Integrating by parts and keeping the divergent term (surface terms actually vanish for finite nonzero k), we get

$$\frac{\mathrm{d}\Delta_{\mathbf{k}}}{\mathrm{d}k} \approx -\frac{1}{2\pi}\int_0^\infty \bar{U}^{irreg}(k,k')\frac{\mathrm{d}}{\mathrm{d}k'}\left\{k' \frac{\Delta_{\mathbf{k}'}}{2E_{\mathbf{k}'}}\left[1 - f(E^+_{\mathbf{k}'}) - f(E^-_{\mathbf{k}'})\right]\right\}\mathrm{d}k' \tag{3.86}$$

We first analyze the behavior of $\mathrm{d}\Delta_{\mathbf{k}}/\mathrm{d}k$ at $T = 0$ as a function of the distance δk from the zero crossing of $E^{\pm}_{\mathbf{k}}$ and the screening wave vector q_0.

Let us assume for definiteness that the relevant zero crossings are for the $E^+_{\mathbf{k}}$ branch. The term which is responsible for the divergence of $\mathrm{d}\Delta/\mathrm{d}k$ at the zero crossing is that associated with $\mathrm{d}f(E^+_{\mathbf{k}'})/\mathrm{d}k'$ in Eq. 3.86. [4] We focus on this term when k, k' are close to a zero crossing at k^*.

$$\frac{\mathrm{d}\Delta_{\mathbf{k}}}{\mathrm{d}k} \approx -\frac{1}{2\pi}\int_0^\infty \bar{U}^{irreg}(k,k')\,k' \frac{\Delta_{\mathbf{k}'}}{2E_{\mathbf{k}'}}\frac{\mathrm{d}}{\mathrm{d}k'}\left[-f(E^+_{\mathbf{k}'})\right]\mathrm{d}k' \tag{3.87}$$

At $T = 0$, $f(x) = \Theta(-x)$ and $f'(x) = -\delta(x)$, so that

$$\begin{aligned}
\frac{\mathrm{d}\Delta_{\mathbf{k}}}{\mathrm{d}k} &\approx -\frac{1}{2\pi}\int_0^\infty \bar{U}^{irreg}(k,k')\,k' \frac{\Delta_{\mathbf{k}'}}{2E_{\mathbf{k}'}}\delta(E^+_{\mathbf{k}'})\frac{\mathrm{d}E^+_{\mathbf{k}'}}{\mathrm{d}k'}\,\mathrm{d}k' && (3.88)\\
&\approx -\frac{1}{2\pi}\int_0^\infty \bar{U}^{irreg}(k,k')\,k' \frac{\Delta_{\mathbf{k}'}}{2E_{\mathbf{k}'}}\frac{\delta(k'-k^*)}{\left|\frac{\mathrm{d}E^+_{\mathbf{k}'}}{\mathrm{d}k'}\right|}\frac{\mathrm{d}E^+_{\mathbf{k}'}}{\mathrm{d}k'}\,\mathrm{d}k' && (3.89)\\
&\approx -\frac{1}{2\pi}\bar{U}^{irreg}(k,k^*)\,k' \frac{\Delta_{\mathbf{k}'}}{2E_{\mathbf{k}'}}\mathrm{sgn}\left(\left.\frac{\mathrm{d}E^+_{\mathbf{k}'}}{\mathrm{d}k'}\right|_{k'=k^*}\right) && (3.90)
\end{aligned}$$

Using Eq. 3.82 close to k^*

$$\frac{\mathrm{d}\Delta_{\mathbf{k}}}{\mathrm{d}k} \approx \frac{1}{2\pi}\frac{2e^2}{\varepsilon k^*}\ln\left(\frac{2k^*\theta_0}{\sqrt{(k-k^*)^2+q_0^2}}\right)k^*\frac{\Delta^*_{\mathbf{k}}}{2E_{\mathbf{k}^*}}\mathrm{sgn}\left(\frac{\mathrm{d}E^+_{\mathbf{k}^*}}{\mathrm{d}k^*}\right) \tag{3.91}$$

and for $q_0 = 0$ we find

$$\left|\frac{\mathrm{d}\Delta_{\mathbf{k}}}{\mathrm{d}k}\right| \approx \frac{e^2}{\pi\varepsilon}\frac{\Delta^*_{\mathbf{k}}}{2E_{\mathbf{k}^*}}\ln\left(\frac{2k^*\theta_0}{|k-k^*|}\right) \tag{3.92}$$

[4] Note that the derivative of $\Delta_{\mathbf{k}'}/E_{\mathbf{k}'}$ gives rise to a divergence $\ln(k'-k^*)$, as we demonstrate below, which when multiplied by U^{irreg} yield a divergence $\ln^2(k'-k^*)$. This term is however finite when integrated over k' and thus does not contribute to the divergence of $\Delta_{\mathbf{k}}$.

With no screening and at $T = 0$ we thus have that $\mathrm{d}\Delta_{\mathbf{k}}/\mathrm{d}k$ diverges logarithmically as $k \to k^*$.

With screening, at $T = 0$ and for $k = k^*$ we have

$$\left|\frac{\mathrm{d}\Delta_{\mathbf{k}}}{\mathrm{d}k}\right|_{k=k^*} \approx \frac{e^2}{\pi\varepsilon}\frac{\Delta^*_{\mathbf{k}}}{2E_{\mathbf{k}^*}} \ln\left(\frac{2k^*\theta_0}{q_0}\right) \tag{3.93}$$

and see that the screening cuts off the logarithmic divergence at $k = k^*$ and $T = 0$.

Finally, we consider the behavior with temperature T at $k = k^*$ and for $q_0 \to 0$. Going back to Eq. 3.86, we see that the derivative of $f(E^+_{\mathbf{k}})$ at finite T is not a δ-function but is broadened over an energy interval of width $\sim 2T$. Within the logarithmic accuracy of the present calculation we can approximate the derivative at finite but small T

$$-\frac{\mathrm{d}f(x)}{\mathrm{d}x} \approx \delta_T(x) \tag{3.94}$$

where

$$\delta_T(x) = \begin{cases} \frac{1}{2T}, & |x| < T \\ 0, & \text{elsewhere} \end{cases} \tag{3.95}$$

Notice that the area under this function is unity. We have then

$$-\frac{\mathrm{d}f(E^+_{\mathbf{k}'})}{\mathrm{d}k'} = \delta_T(E^+_{\mathbf{k}'})\frac{\mathrm{d}E^+_{\mathbf{k}'}}{\mathrm{d}k'} \tag{3.96}$$

and

$$\delta_T(E^+_{\mathbf{k}'}) = \begin{cases} \frac{1}{2T}, & |k-k^*||\mathrm{d}E^+_{\mathbf{k}'}/\mathrm{d}k'|_{k'=k^*} < T \\ 0, & \text{elsewhere} \end{cases} \tag{3.97}$$

so that

$$\frac{\mathrm{d}\Delta_{\mathbf{k}}}{\mathrm{d}k} \approx -\frac{1}{2\pi}\int_0^\infty \bar{U}^{irreg}(k,k')k'\frac{\Delta_{\mathbf{k}'}}{2E_{\mathbf{k}'}}\delta_T(E^+_{\mathbf{k}'})\frac{\mathrm{d}E^+_{\mathbf{k}'}}{\mathrm{d}k'}\,\mathrm{d}k' \tag{3.98}$$

For $q_0 \to 0$

$$\left.\frac{\mathrm{d}\Delta_{\mathbf{k}}}{\mathrm{d}k}\right|_{k=k^*} \approx \frac{1}{2\pi}\frac{2e^2}{\varepsilon k^*}\int_{k^*-\Delta k}^{k^*+\Delta k} \ln\left(\frac{k^*\theta_0}{|k'-k^*|}\right)k'\frac{\Delta_{\mathbf{k}'}}{2E_{\mathbf{k}'}}\frac{1}{2T}\frac{\mathrm{d}E^+_{\mathbf{k}'}}{\mathrm{d}k'}\,\mathrm{d}k' \tag{3.99}$$

where $\Delta k = T/|\mathrm{d}E^+_{\mathbf{k}^*}/\mathrm{d}k^*|$.

$$\left.\frac{\mathrm{d}\Delta_{\mathbf{k}}}{\mathrm{d}k}\right|_{k=k^*} \approx \frac{1}{2\pi}\frac{2e^2}{\varepsilon k^*}k^*\frac{\Delta^*_{\mathbf{k}}}{2E^*_{\mathbf{k}}}\frac{1}{2T}\frac{\mathrm{d}E^+_{\mathbf{k}^*}}{\mathrm{d}k^*}2\int_0^{\Delta k}\ln\left(\frac{k^*\theta_0}{\delta k}\right)\mathrm{d}(\delta k) \quad (3.100)$$

$$\approx \frac{e^2}{\pi\varepsilon}\frac{\Delta^*_{\mathbf{k}}}{2E^*_{\mathbf{k}}}\frac{1}{T}\frac{\mathrm{d}E^+_{\mathbf{k}^*}}{\mathrm{d}k^*}\int_0^{\Delta k}\left[\underbrace{\ln(k^*\theta_0)}_{\text{negligible}}-\ln(\delta k)\right]\mathrm{d}(\delta k) \quad (3.101)$$

$$\approx -\frac{e^2}{\pi\varepsilon}\frac{\Delta^*_{\mathbf{k}}}{2E^*_{\mathbf{k}}}\frac{1}{T}\frac{\mathrm{d}E^+_{\mathbf{k}^*}}{\mathrm{d}k^*}\left[\Delta k\ln\Delta k-\Delta k\right] \quad (3.102)$$

$$\approx -\frac{e^2}{\pi\varepsilon}\frac{\Delta^*_{\mathbf{k}}}{2E^*_{\mathbf{k}}}\frac{1}{T}\frac{\mathrm{d}E^+_{\mathbf{k}^*}}{\mathrm{d}k^*}\Delta k\ln\Delta k \quad (3.103)$$

$$\approx -\frac{e^2}{\pi\varepsilon}\frac{\Delta^*_{\mathbf{k}}}{2E^*_{\mathbf{k}}}\frac{1}{T}\frac{\mathrm{d}E^+_{\mathbf{k}^*}}{\mathrm{d}k^*}\frac{T}{|\mathrm{d}E^+_{\mathbf{k}^*}/\mathrm{d}k^*|}\ln\left(T/|\mathrm{d}E^+_{\mathbf{k}^*}/\mathrm{d}k^*|\right) \quad (3.104)$$

$$(3.105)$$

and we find

$$\left|\frac{\mathrm{d}\Delta_{\mathbf{k}}}{\mathrm{d}k}\right|_{k=k^*} \approx \frac{e^2}{\pi\varepsilon}\frac{\Delta^*_{\mathbf{k}}}{2E^*_{\mathbf{k}}}|\ln T| \quad (3.106)$$

In summary, we have the following behavior for the derivative expressed in our units.

$$\frac{\mathrm{d}\Delta_{\mathbf{k}}}{\mathrm{d}k} = -\sigma\frac{\Delta^*_{\mathbf{k}}}{\pi E^*_{\mathbf{k}}}\times\begin{cases}\ln|k-k^*| & \text{as} \quad k\to k^* \quad \text{for} \quad T=0 \quad \text{and} \quad q_0=0\\ \ln q_0 & \text{as} \quad q_0\to 0 \quad \text{for} \quad T=0 \quad \text{and} \quad k=k^*\\ \ln T & \text{as} \quad T\to 0 \quad \text{for} \quad q_0=0 \quad \text{and} \quad k=k^*\end{cases} \quad (3.107)$$

and $\sigma = +1$ at the first zero crossing of $E^+_{\mathbf{k}}$ when there are two zero crossings and $\sigma = -1$ at the second crossing or when there is just one zero crossing.

We now check these expressions numerically for an S1 phase with one zero crossing and an S2 phase with two. We use system parameters $m_e/m_h = 0.07/0.30$ and $d = a_B$. Fig. 3.34-3.38 show that a corresponding slope from the logarithmic fit around the divergence region ($T \sim 0$ or $k \sim k^*$) agrees with the predicted value within a relative difference of less than 10 % for all cases.

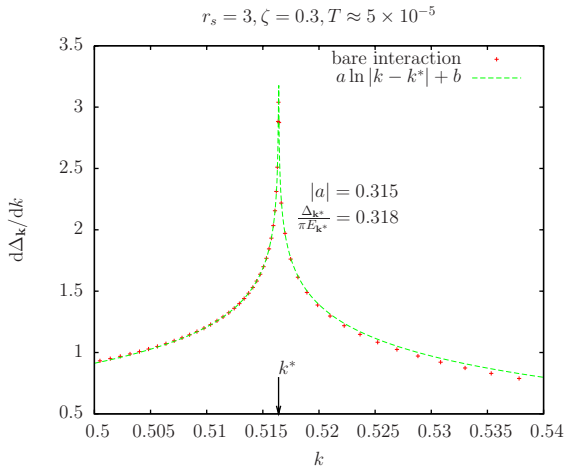

Figure 3.34: Derivative of the gap function at $T = 0$ with no screening around the zero crossing of $E^+_{\mathbf{k}}$. Comparison of the value of the logarithmic fit with the expected value.

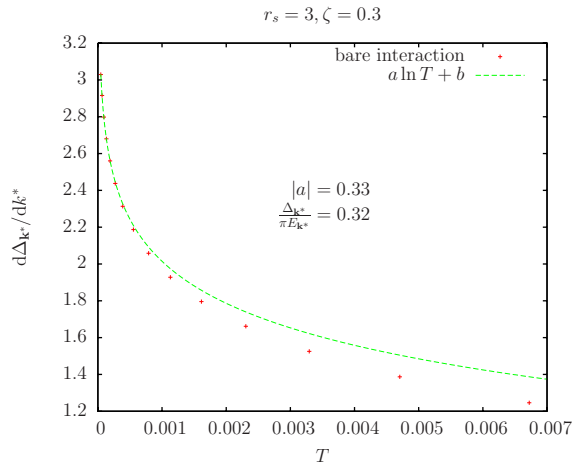

Figure 3.35: The value of the derivative of the gap at $k = k^*$ as a function of temperature T. Comparison of the value of the logarithmic fit with the expected value.

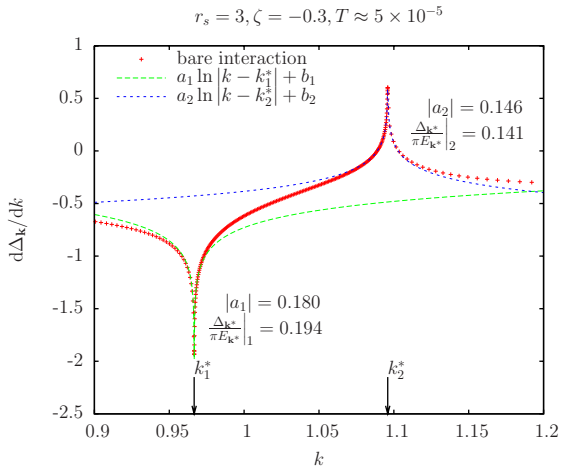

Figure 3.36: Derivative of the gap function at $T = 0$ with no screening around the zero crossings of $E^-_{\mathbf{k}}$. Comparison of the value of the logarithmic fit with the expected value.

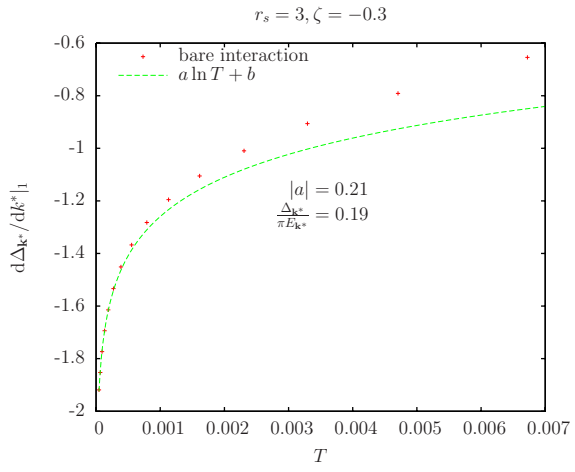

Figure 3.37: The value of the derivative of the gap at $k = k_1^*$ as a function of temperature T. Comparison of the value of the logarithmic fit with the expected value.

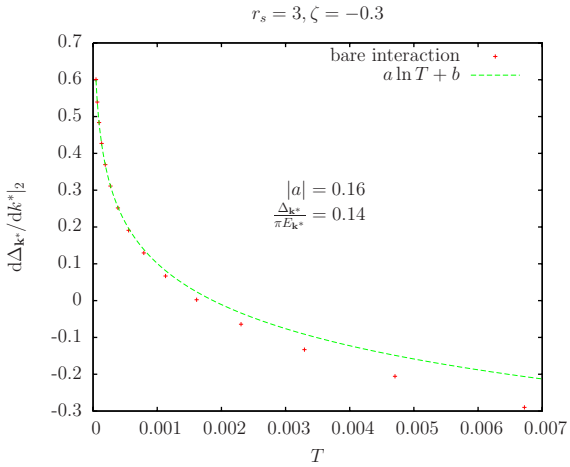

Figure 3.38: The value of the derivative of the gap at $k = k_2^*$ as a function of temperature T. Comparison of the value of the logarithmic fit with the expected value.

Chapter 4

Dimensional Crossover in 2D Bose-Fermi Mixtures

4.1 Introduction

Fermionic atomic gases were brought together with bosonic atoms to quantum degeneracy in several alkali atom mixtures, such as ^{7}Li-^{6}Li [129, 130], ^{23}Na-^{6}Li [131], ^{87}Rb-^{40}K [132–134], and very recently in a mixed gas of ytterbium (Yb) isotopes, ^{174}Yb-^{173}Yb [135]. The boson-fermion (BF) coupling strongly affects the equilibrium properties of the mixture and can drive quantum phase transitions, as collapse [134] in the presence of attractive BF interaction, or spatial demixing as recently observed in the context of three-dimensional (3D) atomic fermion - molecular boson mixtures [69, 136], where the strong interspecies repulsion leads to phase separation.

Such mixtures can be realized from an imbalanced two-component Fermi gas (^{40}K-^{40}K or ^{6}Li-^{6}Li mixtures) where all minority fermions become bound with partners from the majority component as bosons and form a Bose-Einstein condensate (BEC). Though imbalanced Fermi gases allowed to observe spatial phase separation between bosonic dimers and excess majority fermions, the advantage of a two atomic species BF mixture is that boson-boson (BB) and

BF interactions can be driven independently and that one can access attractive BF interactions [137, 138].

The structure and the stability of trapped BF mixtures were studied in 3D by using the Thomas-Fermi approximation for the fermionic component [139, 140] and by using a modified Gross-Pitaevskii (GP) equation for the bosons which self-consistently includes the mean-field interaction generated by the fermionic cloud [141, 142]. Effects of the geometry induced by the trap deformation were studied in the Thomas-Fermi regime in a quasi-3D limit, i.e. when collisions can still be considered as three-dimensional [143]. Such a simple model predicts, in a pancake-shaped trap, that the stability of the mixture depends only on the scattering length and the transverse width of the cloud. One should expect, in a true dimensional crossover, namely including dimensional effects in scattering events, that the mixture stability depends critically on the energy, and thus on the number of particles.

The dimensional crossover from a 3D to a 2D trapped mixture may be studied in the experiments by flattening magnetic or dipolar confinements [144], or by trapping atoms in specially designed pancake potentials, as rotating traps [145], gravito-optical surface traps [146], rf-induced two-dimensional traps [147] or in one-dimensional lattices [148] where a 3D gas can be split in several independent disks.

In the limit where scattering events are two-dimensional, it is well known that a hard-core boson gas shows very different features from its 3D counterpart. In 3D, particle interactions can be described by the zero-momentum and zero-energy limit of T-matrix, leading to a constant coupling parameter. In 2D, T-matrix vanishes at low momentum and energy [149, 150] and the first-order contribution to the coupling is obtained by taking into account the many-body shift in the effective collision energy of two-condensate atoms [151, 152]. This leads to an energy dependent coupling parameter that greatly affects the equilibrium and the dynamical properties of the gas [153, 154].

In this chapter we study the equilibrium properties of a mixture of condensed bosons and spin-polarized fermions, through the dimensional crossover from three

to two dimensions, by following the procedure outlined by Roth [141] for the 3D mixture. We neglect fermion-fermion interactions and we include BF s-wave interaction self-consistently in a suitably modified GP equation for the bosons. For the case of BF repulsive interaction, the increasing anisotropy softens the repulsion, and a quasi-3D spatially demixed mixture is mixed in quasi-2D. For the case of BF attractive interactions, the dimensional crossover acts as a Feshbach resonance and induces repulsive interactions, so that a Q3D mixture near collapse can be driven towards spatial demixing in Q2D. In the strictly 2D regime the results depend on the model one assumes for the two-dimensional scattering lengths.

The chapter is organized as follows. In Sec. 4.2 we introduce the theoretical mean-field model for the description of ground-state density profiles of the BF mixture. The models for the coupling through the dimensional crossover are outlined in Sec. 4.3. The density profiles obtained for a ^{6}Li-^{7}Li and a ^{40}K-^{87}Rb mixtures are shown in Sec. 4.4. Sec. 4.5 offers a summary and some concluding remarks. Details of the numerical calculations are given in Sec. 4.6.

4.2 Mean-Field Model for the Density Profiles

We consider a BF mixture in a 2D geometry, with respective particle numbers N_B and N_F, confined in harmonic trap potentials $V_{B(F)} = \frac{1}{2} m_{B(F)} \omega_{B(F)}^2 r^2$. Here $m_{B(F)}$ is boson (fermion) mass and $\omega_{B(F)}$ is the radial trap frequency as seen by boson (fermion) species. Within the mean-field approach the total energy functional at $T = 0$ is written as

$$\begin{aligned} E[\psi_B, \psi_F] = & \int d^2r \left\{ \frac{\hbar^2}{2m_B} |\nabla \psi_B|^2 + V_B(r) |\psi_B|^2 + \frac{1}{2} g_{BB} |\psi_B|^4 \right\} \\ & + \int d^2r \left\{ T_F + V_F(r) |\psi_F|^2 \right\} + \int d^2r \, g_{BF} |\psi_B|^2 |\psi_F|^2, \end{aligned} \tag{4.1}$$

where ψ_B is the ground-state wave function of bosons and $|\psi_F|^2 = n_F$ gives the fermion density. In the above boson species are in the condensed state and fermion component is assumed to be spin-polarized and its kinetic energy is written within

the Thomas-Fermi-Weizacker approximation as [155–157]

$$T_F = \frac{\hbar^2}{m_F}\left(\pi n_F^2 + \frac{\lambda_W}{8}\frac{|\nabla n_F|^2}{n_F}\right), \tag{4.2}$$

where $n_F = |\psi_F|^2$ is the fermion density and the Weizsacker constant is $\lambda_W = 1/4$. Contrary to the boson wave function ψ_B, the fermionic wave function introduced above to describe the fermion density is only a mere artifice for having more symmetric equations. In the mean-field description, the fermion component is described by the density. Normalization conditions for N_B bosons and N_F fermions read

$$N_B = \int d^2r|\psi_B|^2 \tag{4.3}$$

and

$$N_F = \int d^2r|\psi_F|^2. \tag{4.4}$$

The interaction couplings between the bosons and between bosons and fermions are denoted by g_{BB} and g_{BF}, respectively. One notable difference between the form of the energy functional given above and that in 3D, is that the BB and BF interaction strengths are in general density dependent in contrast to the situation in 3D. More specifically, in 3D the interaction strengths are proportional to the scattering lengths a_{BB} and a_{BF} whereas in 2D as we shall explain below they depend on the density or equivalently the chemical potential. The Euler-Lagrange equations for the mixture read [156, 157]

$$\left\{-\frac{\hbar^2}{2m_B}\nabla^2 + V_B + g_{BB}|\psi_B|^2 + g_{BF}|\psi_F|^2 - \mu_B\right\}\psi_B = 0\,, \tag{4.5}$$

and

$$\left\{-\frac{\hbar^2}{2m_F}\lambda_W\nabla^2 + V_F + \frac{\hbar^2}{m_F}2\pi|\psi_F|^2 + g_{BF}|\psi_B|^2 - \mu_F\right\}\psi_F = 0\,, \tag{4.6}$$

in which we have introduced the chemical potentials $\mu_{B,F}$ for bosons and fermions. The above equations of motion are obtained by functional differentiation from $E[\psi_B, \psi_F]$ neglecting the higher-order terms involving $\delta g/\delta\psi_{B,F}$ which is valid in the dilute gas limit $n_B a_{BB}^2 \ll 1$ and $n_F a_{BF}^2 \ll 1$. The dilute gas conditions

above further maintain that beyond mean-field corrections are not called for. They can become notable when a_{BB}, a_{BF} and/or N_B, N_F are large for fixed trap frequencies. For the systems under consideration we have chosen the parameters appropriately and verified by numerical calculations so that $n_B a_{BB}^2$, $n_F a_{BF}^2 \ll 1$. Therefore, in the examples we shall discuss subsequently, the beyond mean-field terms in the energy functional are not important.

It should also be noted that the existence of BEC in 2D needs to be treated carefully. Initial attempts have concluded that no BEC could occur in 2D trapped gases but recent considerations within the Hartree-Fock-Bogoliubov approximation, [158] the density dependent interaction strength [159] and numerical simulations [160] have established firmly the occurrence of BEC for such systems. Thus, our assumption of a 2D condensate at $T = 0$ is justified.

We solve these equations numerically using the method of steepest descend and also by directly minimizing the energy functional. This is described in Sec. 4.6.

4.3 2D Interaction Models

In cold atom experiments a 2D geometry is obtained by trapping the atoms in a highly anisotropic trap where the axial confinement is very tight, so that the axial potential is on the same order or larger than the chemical potentials of the two components. Within this condition, the axial widths are on the order of the oscillator lengths for the axial direction $a_{jz} = \sqrt{\hbar/m_j\omega_{jz}}$, ω_{jz} being the axial trap frequency for bosons ($j = B$) and for fermions ($j = F$). For the sake of clarity and simplicity, in the following we simply assume that $a_{Bz} = a_{Fz} = a_z$, a condition that could be realized in the experiments by a suitable choice of the axial confinement.

The value of a_z with respect to the modulus of the 3D scattering lengths, determines whether the scattering events occur in 3D or in 2D, and thus suggests how to calculate the many-body interaction potentials.

The interaction couplings g_{BB} and g_{BF} are determined microscopically from

the effective interaction potentials (two-body scattering amplitude, T-matrix are briefly discussed in Sec. 4.6) in the limit of low energy and momenta. In the case of a 3D system, the scattering amplitude and g_{BB} and g_{BF} are constants determined by the s-wave scattering lengths a_{BB} and a_{BF}. In 2D the scattering theory approaches give rise to a logarithmic dependence on density [149, 150]. Starting from a 3D system and increasing the anisotropy (by increasing the trap frequencies in the axial direction) the geometry flattens to take a pancake shape and eventually a genuine 2D system is obtained. In the following we identify different scattering regimes depending on the relation between the axial confinement length and scattering lengths and provide expressions for the interaction couplings in these regimes.

4.3.1 Quasi-3D Scattering

In this regime, the axial oscillator length a_z of the mixture is assumed to be larger than the modulus of a_{BB} and a_{BF}, the s-wave scattering lengths for BB and BF interactions, respectively.

The effective BB interaction strength can be obtained by multiplying the 3D value of the coupling

$$g_{BB}^{3D} = 4\pi\hbar^2 a/m_B \tag{4.7}$$

with a factor $|\phi(0)|^2 = 1/\sqrt{2\pi}a_z$, $\phi(z)$ being the axial wave function. This is obtained by assuming that the motion in the z-direction is frozen in the ground state of the harmonic potential with trapping frequency ω_{jz} and integrating the 3D GP equation over z (after multiplying with $\phi^*(z)$ in the spirit of taking an expectation value. The chemical potential μ_j gets shifted by $\hbar\omega_{jz}/2$). Assuming that the profile for fermions also to be Gaussian in the z-direction, we apply the same idea to the BF interaction $g_{BF}^{3D} = 2\pi\hbar^2 a/m_{BF}$, where m_{BF} is the reduced mass. Thus, we obtain

$$g_{BB} = \frac{2\sqrt{2\pi}\hbar^2}{m_B}\frac{a_{BB}}{a_z}, \text{ and } g_{BF} = \frac{\sqrt{2\pi}\hbar^2}{m_{BF}}\frac{a_{BF}}{a_z}, \tag{4.8}$$

as the effective interaction couplings in the quasi-3D scattering regime.

4.3.2 Strictly-2D Scattering

This regime corresponds to the limit $a_z \ll |a_{BB}|, |a_{BF}|$. The coupling parameter we use is from a T-matrix calculation [151, 152, 161] which takes into account the many-body shift in the effective collision energy of two condensate atoms and it becomes a self-consistent problem. Since $a_z \ll |a_{BB}|$, $|a_{BF}|$ the calculation is purely 2D, and the interaction strengths do not depend on the parameters in the z-direction. Al Khawaja *et al.* [151] argue that when two condensate atoms collide at zero momentum they both require an energy μ_B to be excited from the condensate and thus the many-body coupling is given by evaluating at $-2\mu_B$ the two-body T-matrix (T_{2b}) setting $g_{BB} = \langle 0|T_{2b}(-2\mu_B)|0\rangle$. On the other hand, Lee *et al.* [161] calculate T_{2b} at $-\mu_B$ arguing that this result includes the effect of quasiparticle energy spectrum of the intermediate states in the collision. Gies *et al.* [162] claim that Al Khawaja *et al.* [151] argument that the excitation of a single condensate atom is associated with an energy of $-\mu_B$ includes on the mean-field energy of initial and final states and neglects the other many-body effects on the collision which presumably are included in the result $g_{BB} = \langle 0|T_{2b}(-\mu_B)|0\rangle$. With this proviso we take

$$g_{BB} = \frac{-4\pi\hbar^2}{m_B} \frac{1}{\ln\left(\mu_B m_B a_{BB}^2/4\hbar^2\right)} \tag{4.9}$$

and similarly,

$$g_{BF} = \frac{-2\pi\hbar^2}{m_{BF}} \frac{1}{\ln\left((\mu_B + \mu_F) m_{BF} a_{BF}^2/4\hbar^2\right]} \tag{4.10}$$

where the scattering lengths $a_{BB} = a_{BB}^{2D}$ and $a_{BF} = a_{BF}^{2D}$ are in principle 2D scattering lengths. Our choice for the 2D scattering lengths will be discussed in Sec. 4.4. In the case of BF interaction strength we used the reduced mass m_{BF} and made replacement $\mu \to (\mu_B + \mu_F)/2$. Similar considerations to write down the BF T-matrix were also made by Mur-Petit *et al.* [163, 164].

In this regime the interaction parameters must be determined self-consistently.

The chemical potentials are given by

$$\mu_B = \frac{1}{N_B}\int d^2r \left\{ \frac{\hbar^2}{2m_B}|\nabla\psi_B|^2 + \frac{1}{2}m_B\omega_B^2 r^2|\psi_B|^2 + g_{BB}|\psi_B|^4 + g_{BF}|\psi_F|^2|\psi_B|^2 \right\} \tag{4.11}$$

and

$$\mu_F = \frac{1}{N_F}\int d^2r \left\{ \frac{\hbar^2}{2m_F}\lambda_W|\nabla\psi_F|^2 + \frac{1}{2}m_F\omega_F^2 r^2|\psi_F|^2 + \frac{\hbar^2}{m_F}2\pi|\psi_F|^4 + g_{BF}|\psi_F|^2|\psi_B|^2 \right\} \tag{4.12}$$

We start with initial chemical potentials, calculate g's and then calculate chemical potentials using the obtained wave functions in the above equations and require self-consistency. Note that in this regime the results do not depend on the value of ω_{jz}, i.e. on the value of the anisotropy parameter $\lambda = \omega_{B,z}/\omega_B$.

4.3.3 Quasi-2D Scattering

When $a_z \gtrsim |a_{BB}|, |a_{BF}|$ collisions are two-dimensional but influenced by the z-direction. In this regime, which is in between the previous cases, the 2D scattering length can be expressed in terms of the 3D scattering length [165]. Substituting

$$a_{ij}^{2D} = 2\sqrt{2}\sqrt{\frac{\pi}{B}}a_z e^{-\sqrt{\pi/2}\frac{a_z}{a_{ij}^{3D}}} \tag{4.13}$$

in the coupling strength expressions for strictly 2D regime with $B \approx 0.915$, the coupling strengths now become [161]

$$g_{BB} = \frac{\frac{2\sqrt{2\pi}\hbar^2}{m_B}\frac{a_{BB}}{a_z}}{1 + \frac{1}{\sqrt{2\pi}}\frac{a_{BB}}{a_z}\ln(B\hbar^2/2\pi\mu_B m_B a_z^2)} \tag{4.14}$$

and

$$g_{BF} = \frac{\frac{\sqrt{2\pi}\hbar^2}{m_{BF}}\frac{a_{BF}}{a_z}}{1 + \frac{1}{\sqrt{2\pi}}\frac{a_{BF}}{a_z}\ln(B\hbar^2/2\pi(\mu_B+\mu_F)m_{BF}a_z^2)}. \tag{4.15}$$

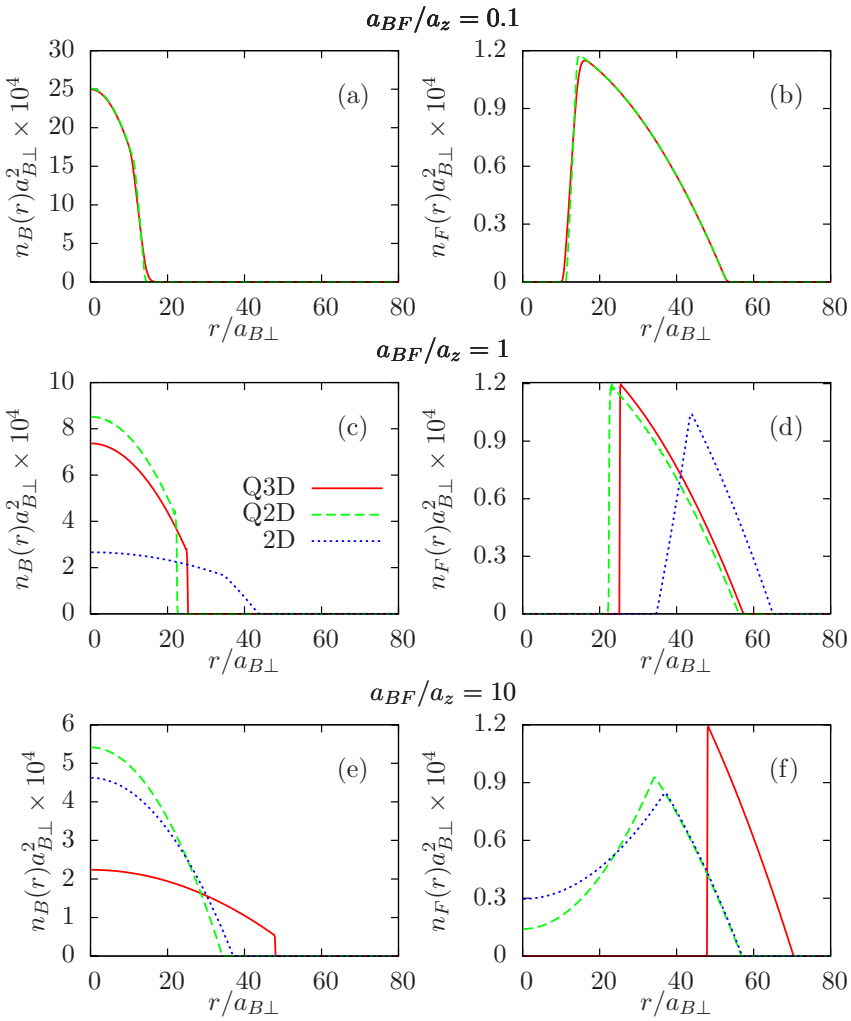

Figure 4.1: Boson and fermion density profiles for ^{6}Li-^{7}Li mixture with $N_B = 10^6$ and $N_F = 5 \times 10^5$, radial trapping frequencies $\omega_B/2\pi = 4000\,Hz$, $\omega_F/2\pi = 3520\,Hz$ and scattering lengths $a_{BB} = 5.1\,a_0$, $a_{BF} = 38\,a_0$ where a_0 is the Bohr radius. The length unit is the radial harmonic oscillator length $a_\perp = \sqrt{\hbar/m_B\omega_B}$. The density given is in units of $10^{-4}a_{B,\perp}^{-2}$ and is normalized to unity. The three regimes $a_{BF}/a_z = 0.1$, 1, 10 correspond to values of the asymmetry parameter $\lambda \approx 10^3$, 10^5, and 10^7, respectively.

	$\mu_B/\hbar\omega_{Bz}$				$\mu_F/\hbar\omega_{Fz}$		
$\frac{a_{BF}}{a_z}$	Q3D	Q2D	2D	$\frac{a_{BF}}{a_z}$	Q3D	Q2D	2D
0.1	0.19	0.19	n/a	0.1	0.90	0.90	n/a
1	0.0056	0.0055	0.018	1	0.010	0.010	0.013
10	0.00017	0.000085	0.000095	10	0.00016	0.00010	0.00010

Table 4.1: The ratio of the chemical potential in two dimensions to the trapping energy in the third direction in different models for the Li-Li mixture. Increasing values of a_{BF}/a_z corresponding to higher values of the asymmetry parameter λ show that tighter confinement in the third direction makes the mixture more and more two-dimensional. The values being less than unity render the system kinematically two-dimensional.

4.4 Results and Discussion

We first consider a lithium mixture with particle numbers $N_B = 10^6$ and $N_F = 5 \times 10^5$, and radial trapping frequencies $\omega_B/2\pi = 4000\,\text{Hz}$ and $\omega_F/2\pi = 3520\,\text{Hz}$. The BB and BF scattering lengths are taken as $a_{BB} = 5.1\,a_0$ and $a_{BF} = 38\,a_0$, respectively, in which a_0 is the Bohr radius.

In Fig. 4.1 we show the density distributions $n_B(r)$ and $n_F(r)$ of bosonic and fermionic components in the three scattering regimes: the quasi-3D, where the coupling is given by Eq. (4.8), the quasi-2D, where the coupling is given in Eqs. (4.14) and (4.15), and the strictly 2D, where we use the coupling given in Eqs. (4.9) and (4.10) and where we set the two-dimensional scattering lengths equal to a_{ij}^{2D} (Eq. (4.13)) evaluated in the limit of vanishing a_z/a_{ij}^{3D}. This choice assures the strictly 2D model to be the limiting case of the Q2D, that depicts the crossover behavior.

When $a_{BF}/a_z = 0.1$ (top panel) the mixture has 3D character in terms of collisions even though the geometrical confinement ($\lambda = 10^3$) renders the system 2D kinematically. The ratio of the chemical potentials in the 2D description to the trapping energy in the third direction, $\mu_B/\hbar\omega_{Bz}$ $\mu_F/\hbar\omega_{Fz}$, being less than unity also confirms that the system is geometrically 2D. (see Table 4.1) In this regime the densities for quasi-3D and quasi-2D models look very similar. The

boson and fermion components occupy the inner and outer parts of the disk giving a segregated phase for the chosen parameters. The 2D model is evidently inapplicable in this regime because $a_{BF}/a_z < 1$.

In the middle panels of Fig. 4.1 we show density profiles for the same mixture with $a_{BF}/a_z = 1$ for an anisotropy parameter $\lambda = 10^5$. This corresponds to a completely frozen motion in the z-direction and to the crossover in the scattering properties from 3D to 2D. Figures 4.1(c) and 4.1(d) reveal that the density profiles in the three models are very similar, except for the fact that the 2D model predicts a larger spatial extension of the density profiles.

Finally, in the bottom panel of Fig. 4.1 we consider $a_{BF}/a_z = 10$ with $\lambda = 10^7$. a_z being smaller than in the previous case, the two-dimensional scattering lengths are smaller and both the 2D and Q2D models predict a mixed phase even in the center of the trap, while the Q3D curves still show phase separation. For this anisotropy parameter, the scattering events should be truly 2D and our corresponding model should yield the most accurate density profiles. Evidently the Q3D model is not valid anymore, but we plot it just to compare the predictions of the different models.

From the numerical examples presented above we find that the collisional properties of different scattering regimes can influence the density profiles $n_B(r)$ and $n_F(r)$ in a boson-fermion mixture. Vanishing fermion density in the center of the trap is a sign of spatial separation (demixing) and the onset of spatial separation also marks the point where TF approximation fails. This can be seen in Fig. 4.2 and Fig. 4.3 where we show the TF radii and chemical potential values as a function of the asymmetry parameter. The bosonic radius decreases approaching demixing since the boson component is squeezed by the fermions while the fermionic radius increases due to the fact that fermions being pushed out by bosons. The inaccessible region corresponding to $a_{BF}/a_z \approx 1$ can be identified with demixing as the numerical solution of GP equation shows. As λ is increased further the interactions strengths get smaller, the components mix again. The boson and fermion radii increase and decrease respectively as the Q2D model approaches the strictly 2D model.

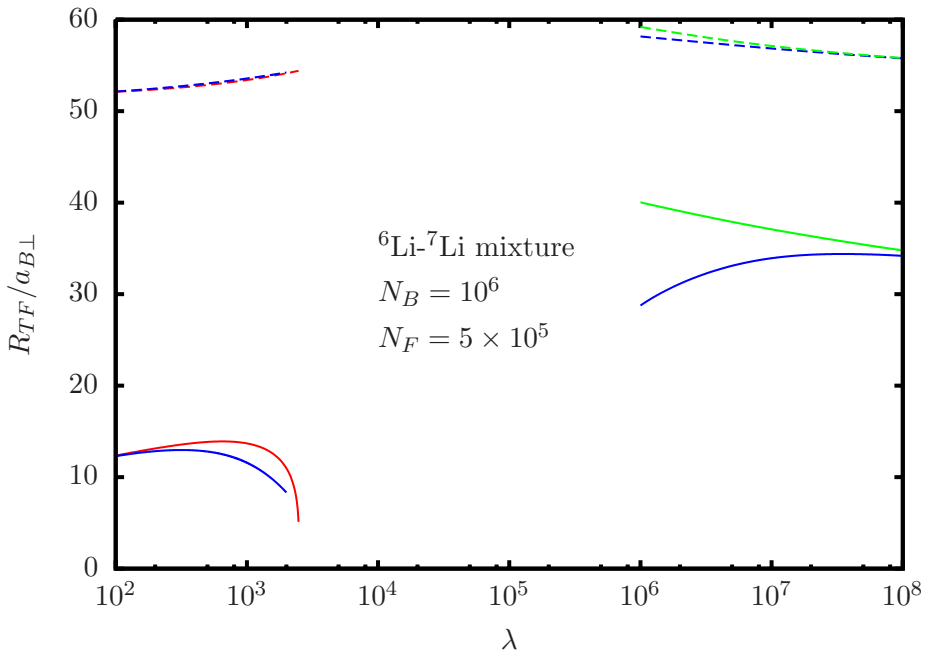

Figure 4.2: The Thomas-Fermi radii as a function of the asymmetry parameter λ for the ^{6}Li-^{7}Li mixture. The color code for the three models is: red for Q3D, blue for Q2D and green for 2D scattering. The solid lines show boson values and the dashed lines show fermion values. The inaccessible region corresponds to spatial separation. For system parameters, see Fig. 4.1.

We now turn our attention to ^{40}K-^{87}Rb mixture having an attractive BF scattering length. We consider a system with particle numbers $N_B = 10^6$ and $N_F = 5 \times 10^5$, and radial trapping frequencies $\omega_B/2\pi = 257\,\text{Hz}$ and $\omega_F/2\pi = 378\,\text{Hz}$. The BB and BF scattering lengths are taken as $a_{BB} = 110\,a_0$ and $a_{BF} = -284\,a_0$, respectively [166]. For attractive interactions, the effective 2D BF scattering length is positive [see Eq. (4.13)], namely the dimensional crossover induces effective repulsive interactions [163, 164], as already predicted in a condensate with attractive boson-boson interaction [165]. Thus, the strictly 2D couplings (Refs. [151, 161–164]) refer to hard-core collisions [149].

Figure 4.4 illustrates the density profiles $n_B(r)$ and $n_F(r)$ in quasi-3D and 2D

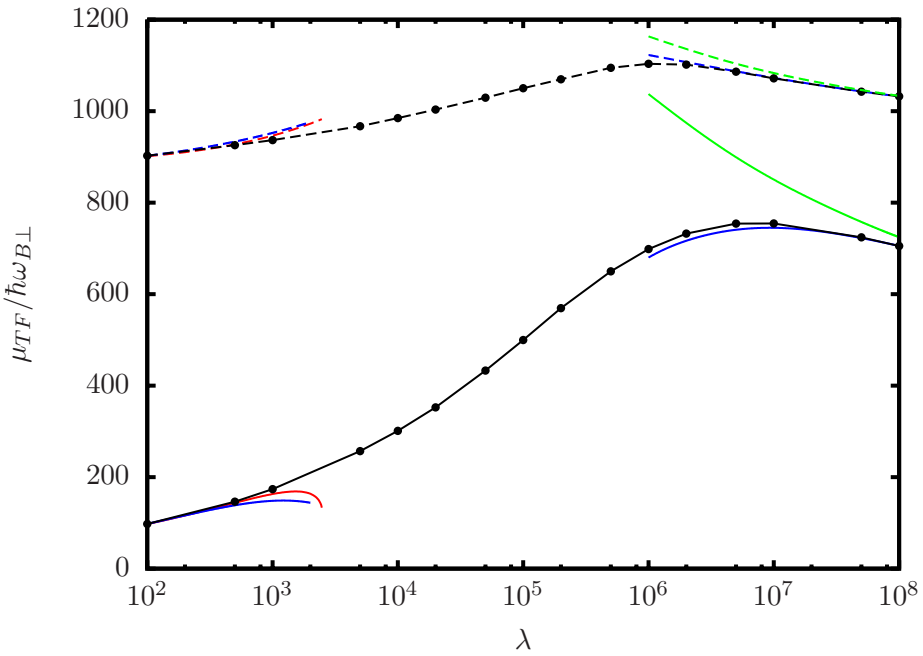

Figure 4.3: The chemical potential values within the TF approximation as a function of the asymmetry parameter λ for the ^{6}Li-^{7}Li mixture. The color code for the three models is: red for Q3D, blue for Q2D and green for 2D scattering. The solid lines show boson values and the dashed lines show fermion values. The inaccessible region corresponds to spatial separation. The black curve with points is obtained from the numerical solution of GP equation for the Q2D model which approaches to Q3D and 2D models at the limiting regimes. For system parameters, see Fig. 4.1.

scattering regimes, characterized by $a_{BF}/a_z = -0.3$ ($\lambda \approx 2 \times 10^2$) and $a_{BF}/a_z = -10$ ($\lambda \approx 2 \times 10^5$), respectively. In the case $a_{BF}/a_z = -0.3$, we observe that the density profiles are similar for quasi-3D and quasi-2D models and show a bump in the center of the fermionic density due to the attraction with the bosons. For $a_{BF}/a_z = -10$, the Q2D model approaches the 2D one, the only difference being that the first model predicts complete spatial separation between the bosonic and the fermionic components, while the second predicts a residual mixed phase at the center of the trap. The energy in the plane and in the third direction is

	$\mu_B/\hbar\omega_{Bz}$			$\mu_F/\hbar\omega_{Fz}$			
$\frac{a_{BF}}{a_z}$	Q3D	Q2D	2D	$\frac{a_{BF}}{a_z}$	Q3D	Q2D	2D
-0.3	0.23	1.2	n/a	-0.3	3.0	3.2	n/a
-10	n/a	0.0063	0.0070	-10	n/a	0.0046	0.0046

Table 4.2: The ratio of the chemical potential in two dimensions to the trapping energy in the third direction in different models for the K-Rb mixture. Increasing values of $|a_{BF}|/a_z$ corresponding to higher values of the asymmetry parameter λ show that tighter confinement in the third direction makes the mixture more and more two-dimensional.

compared in Table 4.2 where the use of a 2D description is seen to be proper.

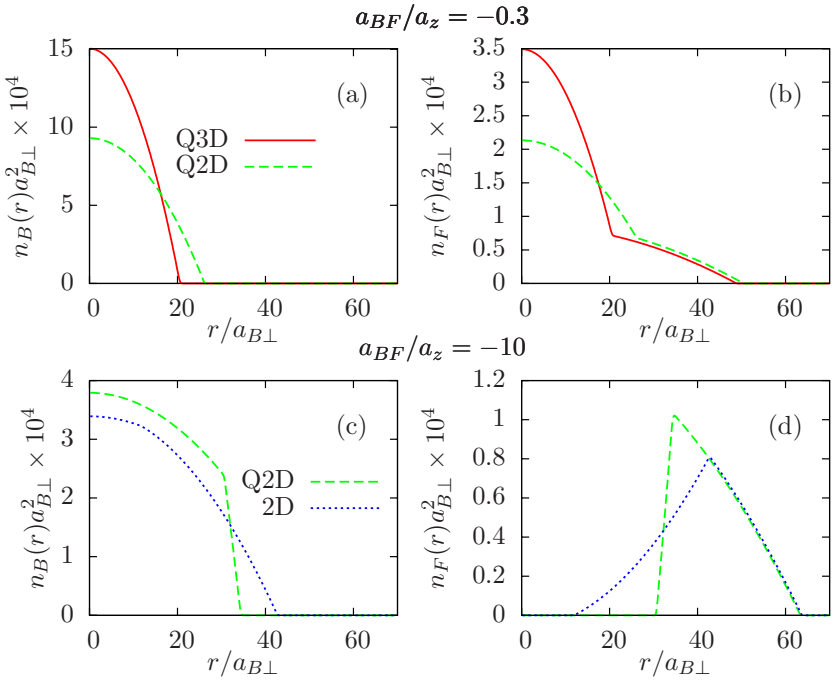

Figure 4.4: Same as in Fig. 4.1 for the ^{40}K-^{87}Rb mixture with $N_B = 10^6, N_F = 5 \times 10^5$. The values of $|a_{BF}|/a_z = 0.3,\ 10$ correspond to $\lambda \approx 2 \times 10^2$ and 2×10^5.

The crossover between the two regimes is shown in Fig. 4.5 and Fig. 4.6 from

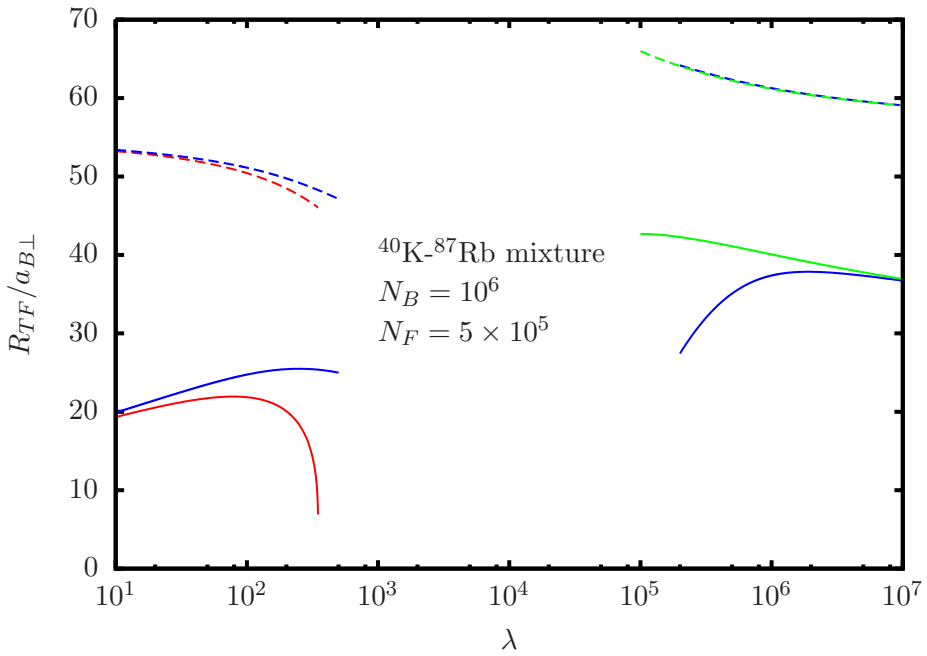

Figure 4.5: The Thomas-Fermi radii as a function of the asymmetry parameter λ for the ^{40}K-^{87}Rb mixture. The color code for the three models is: red for Q3D, blue for Q2D and green for 2D scattering. The solid lines show boson values and the dashed lines show fermion values. The inaccessible region corresponds to collapse. For system parameters, see Fig. 4.4.

a different perspective where TF radii and chemical potential values are plotted as a function of the asymmetry parameter λ for the three models. Unlike the situation in the Li-Li mixture the boson cloud radius increases and fermion cloud radius decreases at first due to increasing attractive BF interaction and as λ is increased further the mixture cloud starts to shrink all together. The inaccessible region around $a_{BF} \approx a_z$ corresponds collapse of the system due to attractive BF interaction. (see also Fig. 4.8) Beyond this region, on the other side of the resonance, the interaction turns from attractive to repulsive and as it decreases in strength the components mix again in the 2D limit.

The density profiles on both sides of the crossover region for the Q2D model

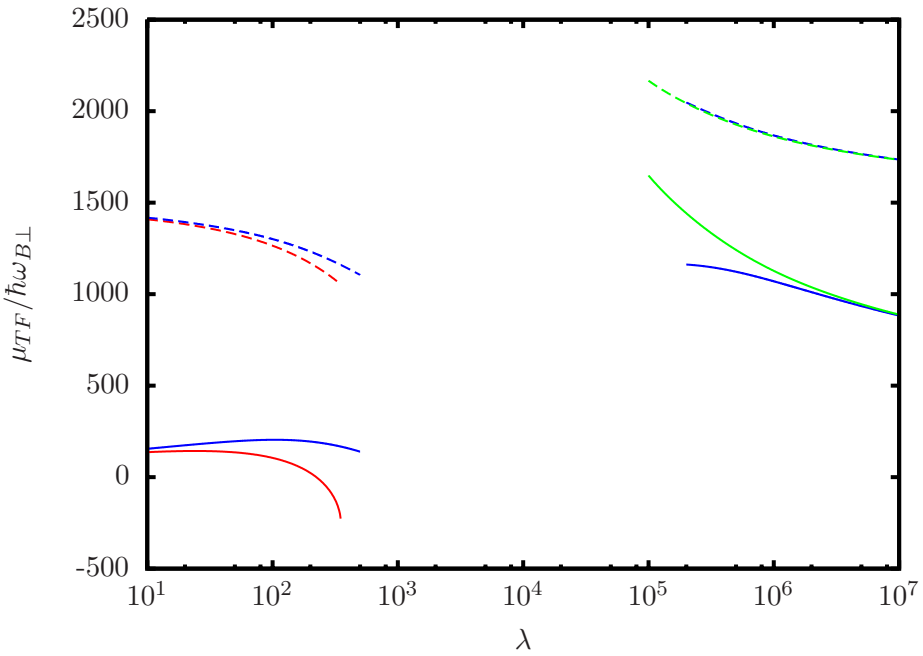

Figure 4.6: The chemical potential values within the TF approximation as a function of the asymmetry parameter λ for the ^{40}K-^{87}Rb mixture. The color code for the three models is: red for Q3D, blue for Q2D and green for 2D scattering. The solid lines show boson values and the dashed lines show fermion values. The inaccessible region corresponds to collapse. For system parameters, see Fig. 4.4.

are shown in Fig. 4.7. For the first three values of $\lambda \leq 10^2$, the fermionic density is enhanced at the center of the trap because of the presence of the bosons. In this regime the BF coupling term is negative, as shown in Fig. 4.8. At $\lambda = 10^5$ the fermions are pushed out of the center of the trap because of the large repulsive BF interaction (see Fig. 4.8). By increasing further and further the anisotropy, the BF coupling is still positive but decreases and the two components are partially mixed. For $10^2 < \lambda < 10^5$ no stable solutions are found. Thus, as shown in Fig. 4.8, the dimensional crossover plays the role of a Feshbach resonance. Squeezing the trap one may naively expect the gas just collapsing, but the crossover in the scattering geometry changes the nature of the instability from

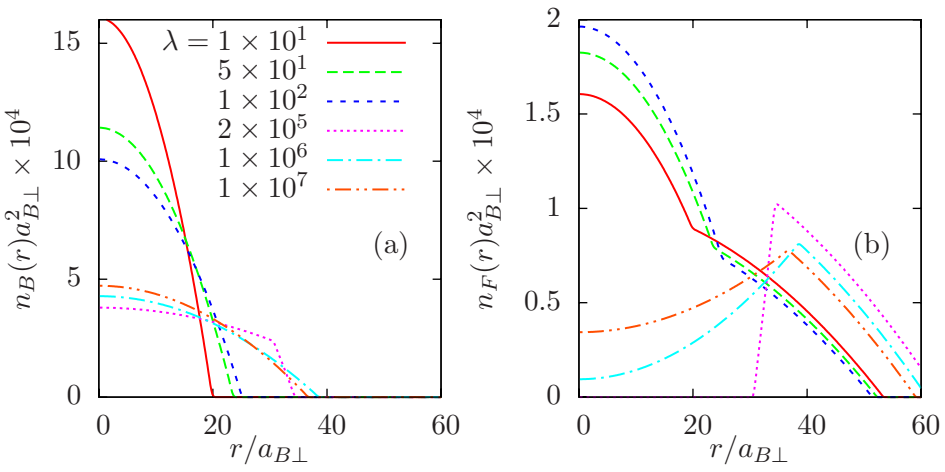

Figure 4.7: Density profiles for the ^{40}K-^{87}Rb mixture calculated with the Q2D model for various values of λ. (Same units as in Fig. 4.1.)

collapse to demixing, and a further squeezing of the trap stabilizes the mixture. All curves shown in this sections correspond to densities that fulfill the diluteness conditions $n_B a_{BB}^2 \ll 1$ and $n_F a_{BF}^2 \ll 1$, even at close to the resonance shown in Fig. 4.8.

4.5 Summary

In summary we have studied the equilibrium properties of a boson-fermion mixture confined in a pancake-shaped trap, in the dimensional crossover from 3D to 2D. The boson-boson and the boson-fermion couplings used are those derived from the two-body T-matrix evaluated (i) at zero energy in 3D, (ii) taking into account the discreteness of the spectrum in the axial direction, in the crossover, (iii) taking into account the many-body energy shift in the strictly 2D limit. The density profiles and the couplings have been evaluated self-consistently using suitable modified coupled Gross-Pitaevskii equations for the bosonic and the fermionic wave functions.

For the case of a positive 3D boson-fermion scattering length, the dimensional

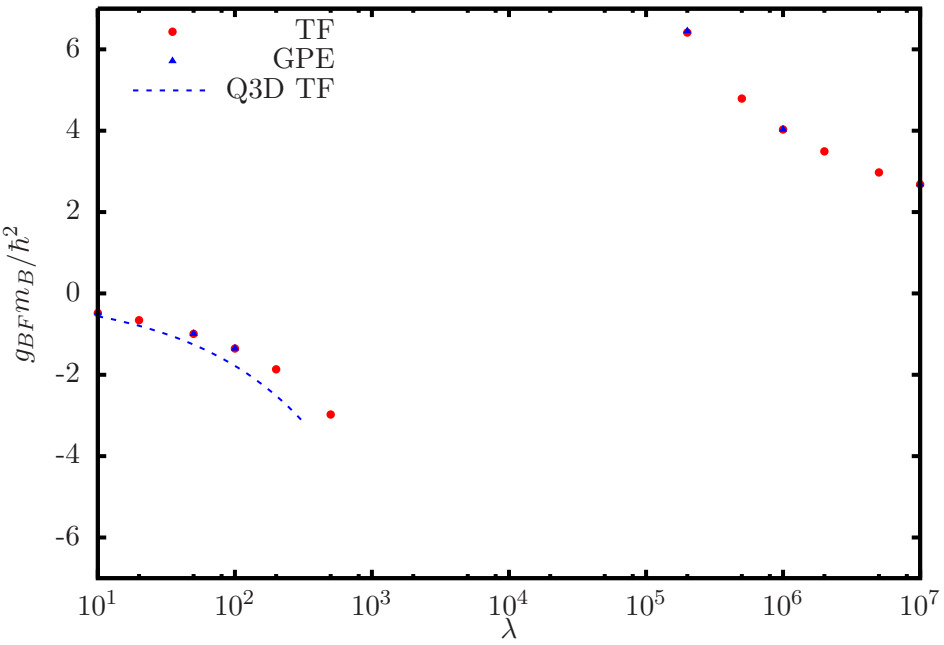

Figure 4.8: Effective BF interaction strength for the ^{40}K-^{87}Rb mixture within the Q2D model as a function of the anisotropy parameter λ. Dots refer to the numerical calculation performed in the Thomas-Fermi (TF) approximation, namely neglecting the Laplacian terms in Eqs. (4.5) and (4.6), while triangles refer to the full solution of the same equations (GPE). The dashed line shows the Q3D coupling within the validity of the TF approximation.

crossover softens the repulsion, so that the components of a demixed boson-fermion mixture in 3D can mix in the 2D limit. For the case of a negative 3D boson-fermion scattering length, the dimensional crossover is more dramatic and plays the role of a Feshbach resonance. Our study shows that the squeezing of the pancake-shaped trap may drive a strong-attractive unstable mixture towards a stable mixed two component mixture passing through a demixed phase. This numerical study may be reproduced in the actual experiments with BF mixtures. The goal being to reach a regime where the modulus of the scattering lengths is comparable or greater than the mixture axial size, one may exploit Feschbach resonances to increase the magnitude of the 3D scattering lengths, or one may

engineer very flat traps as already done in the context of experiments with a single BEC component.

A possibility in these systems is to rotate atomic clouds. It would therefore be interesting to look at vortex states, critical rotation frequency and the dimensional scattering effects for rotating mixtures. It would also be interesting to study similar effects in two species fermion mixtures along the BCS-BEC crossover by changing the inter-species interaction with possible population imbalance.

Appendix

In the rest of this chapter we provide details of the solution of the Gross-Pitaevskii equation. We briefly describe the numerical implementation and the TF calculation. A short discussion on scattering length and effective interaction is followed by the numerical values for the scaled quantities used in the calculations at the end.

4.6 Numerical Solution of Gross-Pitaevskii Equation

At $T = 0$, the total energy functional for a Bose-Fermi mixture in the mean-field approximation can be written as

$$\begin{aligned} E = &\int \mathrm{d}^2 r \left\{ \frac{\hbar^2}{2m_B} |\nabla \psi_B|^2 + V_B(\mathbf{r}) |\psi_B|^2 + \frac{1}{2} g_{BB} |\psi_B|^4 \right\} \\ &+ \int \mathrm{d}^2 r \left\{ T_F + V_F(\mathbf{r}) |\psi_F|^2 \right\} + \int \mathrm{d}^2 r \, g_{BF} |\psi_B|^2 |\psi_F|^2, \end{aligned} \tag{4.16}$$

where $V_{B,F} = \frac{1}{2} m_{B,F} \omega_{B,F}^2 r^2$ are harmonic trapping potentials for bosons and fermions and $g_{BB,BF}$ are boson-boson and boson-fermion interaction strengths respectively. In the dilute limit where only s-wave scattering is considered there is no fermion-fermion interaction for a spin polarized gas due to Pauli exclusion principle. T_F is the kinetic energy density for spin polarized fermions in 2D. From general considerations we take the kinetic energy functional for spin species σ to be

$$T_\sigma = A n_\sigma^2 + \frac{B}{4} \frac{|\nabla n_\sigma|^2}{n_\sigma} \tag{4.17}$$

where A and B are unknown coefficients. For $n_\uparrow = n_\downarrow = n/2$, we should get the result used by van Zyl and Zaremba [155] (for electrons)

$$T = \frac{\pi}{2} n^2 + \frac{\lambda_W}{8} \frac{|\nabla n|^2}{n} \tag{4.18}$$

in atomic units where $e^2/\varepsilon = \hbar = m = 1$. Now,

$$T_\uparrow = \frac{A}{4} n^2 + \frac{B}{8} \frac{|\nabla n|^2}{n}$$

and

$$T = 2T_\uparrow = \frac{A}{2}n^2 + \frac{B}{4}\frac{|\nabla n|^2}{n}$$

Comparing with the van Zyl-Zaremba expression we obtain the coefficients

$$A = \pi \qquad \text{and} \qquad B = \lambda_W/2 \tag{4.19}$$

Therefore

$$T_\sigma = \pi n_\sigma^2 + \frac{\lambda_W}{8}\frac{|\nabla n_\sigma|^2}{n_\sigma} \tag{4.20}$$

In the case of a fully spin-polarized gas, $n_\uparrow = n$, $n_\downarrow = 0$, so the kinetic energy functional becomes

$$T = \pi n^2 + \frac{\lambda_W}{8}\frac{|\nabla n|^2}{n} \tag{4.21}$$

Introducing back the dimension full quantities we obtain our Thomas-Fermi-Weizsacker (TFW) approximation

$$T_F = \frac{\hbar^2}{m_F}\left(\pi n_F^2 + \frac{\lambda_W}{8}\frac{|\nabla n_F|^2}{n_F}\right), \tag{4.22}$$

where $n_F = |\psi_F|^2$ is the fermion density. In the TFW expression the first term is the simple Thomas-Fermi (TF) result, whereas the second term is the Weizsacker correction. The Weizsacker constant λ_W is suggested to take the value 1/4. Normalization conditions for N_B bosons and N_F fermions read $N_B = \int d^2r|\psi_B|^2$ and $N_F = \int d^2r|\psi_F|^2$.

Total energy functional of the boson and fermion wave functions with this approximation becomes

$$\begin{aligned} E = &\int \mathrm{d}^2r \left\{\frac{\hbar^2}{2m_B}|\nabla\psi_B|^2 + V_B(\mathbf{r})|\psi_B|^2 + \frac{1}{2}g_{BB}|\psi_B|^4\right\} \\ &+ \int \mathrm{d}^2r \left\{\frac{\hbar^2}{m_F}\frac{\lambda_W}{2}|\nabla\psi_F|^2 + \frac{\hbar^2}{m_F}\pi|\psi_F|^4 + V_F(\mathbf{r})|\psi_F|^2\right\} \\ &+ \int \mathrm{d}^2r\, g_{BF}|\psi_B|^2|\psi_F|^2. \end{aligned} \tag{4.23}$$

Identifying the energy density $\mathcal{E}$

$$E = \int \mathrm{d}^2r\mathcal{E}, \tag{4.24}$$

we obtain the Euler-Lagrange equations from

$$\frac{\partial \mathcal{F}}{\partial \psi_B} - \nabla \frac{\partial \mathcal{F}}{\partial(\nabla \psi_B)} = 0 \quad \text{and} \quad \frac{\partial \mathcal{F}}{\partial \psi_F} - \nabla \frac{\partial \mathcal{F}}{\partial(\nabla \psi_F)} = 0, \tag{4.25}$$

where $\mathcal{F} = \mathcal{E} - \mu_B|\psi_B|^2 - \mu_F|\psi_F|^2$ with μ_B and μ_F, the boson and fermion chemical potential entering as Lagrange multipliers to satisfy the particle number equations. The explicit form of the equations of motion are

$$\left\{ -\frac{\hbar^2}{2m_B}\nabla^2 + V_B + g_{BB}|\psi_B|^2 + g_{BF}|\psi_F|^2 - \mu_B \right\} \psi_B = 0 \tag{4.26}$$

$$\left\{ -\frac{\hbar^2}{2m_F}\lambda_W \nabla^2 + V_F + \frac{\hbar^2}{m_F} 2\pi|\psi_F|^2 + g_{BF}|\psi_B|^2 - \mu_F \right\} \psi_F = 0 \tag{4.27}$$

If the Weizsacker term in the fermion kinetic energy density is omitted, our equations go over to the more widely used coupled Gross-Pitaevski and Thomas-Fermi equations for bosons and fermions, respectively. If TF approximation is adopted both for bosons and fermions the above equations simplify to a coupled algebraic equations

$$g_{BB}|\psi_B|^2 + g_{BF}|\psi_F|^2 + V_B = \mu_B \tag{4.28}$$

$$\frac{\hbar^2}{m_F} 2\pi|\psi_F|^2 + g_{BF}|\psi_B|^2 + V_F = \mu_F \tag{4.29}$$

from which we can identify $2\pi\hbar^2/m_F \equiv g_{FF}$ to be the effective fermion-fermion interaction. This simplification is due to the fact that in 2D the kinetic energy of non-interacting fermions is proportional to the density.

As we shall see in the next section, for the models g_{BB} and g_{BF} depend on the chemical potentials μ_B and μ_F which must be determined self-consistently. The chemical potentials are given by the following expressions.

$$\begin{aligned} \mu_B = \frac{1}{N_B} \int d^2r \Bigg\{ & \frac{\hbar^2}{2m_B}|\nabla\psi_B|^2 + \frac{1}{2}m_B\omega_B^2 r^2|\psi_B|^2 \\ & + g_{BB}|\psi_B|^4 + g_{BF}|\psi_F|^2|\psi_B|^2 \Bigg\} \end{aligned} \tag{4.30}$$

and

$$\begin{aligned} \mu_F = \frac{1}{N_F} \int d^2r \Bigg\{ & \frac{\hbar^2}{2m_F}\lambda_W|\nabla\psi_F|^2 + \frac{1}{2}m_F\omega_F^2 r^2|\psi_F|^2 \\ & + \frac{\hbar^2}{m_F} 2\pi|\psi_F|^4 + g_{BF}|\psi_F|^2|\psi_B|^2 \Bigg\} \end{aligned} \tag{4.31}$$

4.6.1 Scaling

In order to solve the coupled equations on computer (and to simplify them) we scale length and energy by the typical length and energy of the harmonic oscillator potential. We introduce

$$a_\perp = \left(\frac{\hbar}{m_B\omega_B}\right)^{1/2}, \quad a_z = \left(\frac{\hbar}{m_B\omega_{Bz}}\right)^{1/2} \tag{4.32}$$

where ω_{Bz} is the trapping frequency for bosons in the third direction. The ratio $\omega_{Bz}/\omega_B = \lambda = a_\perp^2/a_z^2$ is called the asymmetry parameter and is assumed to be $\lambda > 1$ for a pancake-shaped condensate which we model as being two dimensional. We furthermore introduce the following ratios

$$k_m = \frac{m_F}{m_B}, \quad k_\omega = \frac{\omega_F}{\omega_B}, \quad k_N = \frac{N_F}{N_B}, \tag{4.33}$$

and dimensionless coupling constants

$$g'_{BB} = g_{BB}\frac{N_B}{a_\perp^2\hbar\omega_B}, \quad g'_{BF} = g_{BF}\frac{N_B}{a_\perp^2\hbar\omega_B}, \tag{4.34}$$

$$g'_{FF} = g_{FF}\frac{N_B}{a_\perp^2\hbar\omega_B} = \frac{2\pi\hbar^2}{m_F}\frac{N_B}{a_\perp^2\hbar\omega_B} = 2\pi\frac{N_B}{k_m}. \tag{4.35}$$

We rewrite the equations in terms of dimensionless variables $\mathbf{r}' = \mathbf{r}/a_\perp$, $E' = E/\hbar\omega_B$, $\psi'_B = \psi_B a_\perp/\sqrt{N_B}$, $\psi'_F = \psi_F a_\perp/\sqrt{N_B}$ etc. and immediately dropping the redundant prime, we obtain

$$\begin{aligned}\frac{E}{N_B} = &\int \mathrm{d}^2r \left\{\frac{1}{2}|\nabla\psi_B|^2 + \frac{r^2}{2}|\psi_B|^2 + \frac{1}{2}g_{BB}|\psi_B|^4\right\} \\ &+ \int \mathrm{d}^2r \left\{\frac{\lambda_W}{2}\frac{1}{k_m}|\nabla\psi_F|^2 + \frac{1}{2}g_{FF}|\psi_F|^4 + \frac{r^2}{2}k_m k_\omega^2|\psi_F|^2\right\} \\ &+ \int \mathrm{d}^2r\, g_{BF}|\psi_B|^2|\psi_F|^2.\end{aligned} \tag{4.36}$$

which we want to minimize subject to the conditions

$$\int \mathrm{d}^2r|\psi_B|^2 = 1\,, \tag{4.37}$$

and

$$\int \mathrm{d}^2 r |\psi_F|^2 = k_N \,. \tag{4.38}$$

Similarly, the EL equations take the following form

$$\left\{ -\frac{1}{2}\nabla^2 + \frac{r^2}{2} + g_{BB}|\psi_B|^2 + g_{BF}|\psi_F|^2 \right\} \psi_B = \mu_B \psi_B \tag{4.39}$$

$$\left\{ -\frac{\lambda_W}{k_\omega}\frac{1}{2}\nabla^2 + k_m k_\omega^2 \frac{r^2}{2} + g_{FF}|\psi_F|^2 + g_{BF}|\psi_B|^2 \right\} \psi_F = \mu_F \psi_F \tag{4.40}$$

where μ_B, μ_F are scaled by $\hbar\omega_\perp$.

4.6.2 Virial

In equilibrium, we can find from the spatial scaling properties of the boson and fermion wave functions under a coordinate transformation $r \to cr$, a relation that is the virial theorem for this problem [167]. We find that in the energy expression the terms form two groups scaling as c^{-2} and c^2. The desired relation is obtained after differentiating with respect to c and setting $c = 1$

$$\begin{aligned} \int \mathrm{d}^2 r \left\{ \frac{1}{2}|\nabla\psi_B|^2 + \frac{1}{2}g_{BB}|\psi_B|^4 + \frac{\lambda_W}{2}\frac{1}{k_m}|\nabla\psi_F|^2 + \frac{1}{2}g_{FF}|\psi_F|^4 + g_{BF}|\psi_B|^2|\psi_F|^2 \right\} \\ - \int \mathrm{d}^2 r \left\{ \frac{r^2}{2}|\psi_B|^2 + \frac{r^2}{2}k_m k_\omega^2 |\psi_F|^2 \right\} = 0 \end{aligned} \tag{4.41}$$

We use this equation as a check that the numerical solution has to satisfy. Typically, we find that our solutions have virial less than 0.1 except when there is demixing. Spatial separation requires wave functions to change rapidly at the boson-fermion boundary and numerically kinetic energy calculations are not accurate.

4.6.3 Thomas-Fermi (TF) Approximation

We have already written the GP equation when the kinetic energy terms are neglected.

$$g_{BB}|\psi_B|^2 + g_{BF}|\psi_F|^2 + V_B = \mu_B \tag{4.42}$$

$$g_{FF}|\psi_F|^2 + g_{BF}|\psi_B|^2 + V_F = \mu_F \tag{4.43}$$

Obviously, $|\psi_B|^2, |\psi_F|^2 \geq 0$. So by defining the TF radii R_B, R_F where boson and fermion wave functions go to zero respectively through $|\psi_B(R_B)|^2 = 0$ and $|\psi_F(R_F)|^2 = 0$, we obtain two equations. Imposing normalization conditions

$$1 = \int_0^{R_B} 2\pi r \mathrm{d}r |\psi_B|^2 \tag{4.44}$$

$$k_N = \int_0^{R_F} 2\pi r \mathrm{d}r |\psi_F|^2 \tag{4.45}$$

which give two more equations for the chemical potential values μ_B, μ_F in this description.

Assuming $R_F \geq R_B$ (since $g_{FF} \gg g_{BB}$, fermions are pushed out further) we have from the second TF equation

$$|\psi_F|^2 = \frac{1}{g_{FF}} \left(\mu_F - \frac{1}{2} k_m k_\omega^2 r^2 - g_{BF}|\psi_B|^2 \right) \tag{4.46}$$

and substituting this into the first

$$|\psi_B|^2 = \frac{1/g_{BB}}{1 - g_{BF}^2/g_{BB}g_{FF}} \left(\mu_B - \frac{1}{2} r^2 - \frac{g_{BF}}{g_{FF}} \mu_F + \frac{g_{BF}}{g_{FF}} \frac{1}{2} k_m k_\omega^2 r^2 \right) \tag{4.47}$$

Now, from $|\psi_B(R_B)|^2 = 0$

$$\mu_B - \frac{g_{BF}}{g_{FF}} \mu_F - \frac{1}{2} \left(1 - \frac{g_{BF}}{g_{FF}} k_m k_\omega^2 \right) R_B^2 = 0 \tag{4.48}$$

and from $|\psi_F(R_F)|^2 = 0$

$$\mu_F - \frac{1}{2} k_m k_\omega^2 R_F^2 = 0 \tag{4.49}$$

since $|\psi_B(R_F)|^2 = 0$ when $R_F \geq R_B$. Next, imposing $1 = \int_0^{R_B} 2\pi r \mathrm{d}r |\psi_B|^2$ we get

$$1 = \frac{2\pi/g_{BB}}{1 - g_{BF}^2/g_{BB}g_{FF}} \left[\left(\mu_B - \frac{g_{BF}}{g_{FF}} \mu_F \right) \frac{R_B^2}{2} - \left(1 - \frac{g_{BF}}{g_{FF}} k_m k_\omega^2 \right) \frac{R_B^4}{8} \right] \tag{4.50}$$

and from $k_N = \int_0^{R_F} 2\pi r \mathrm{d}r |\psi_F|^2$

$$\begin{aligned} k_N &= \frac{2\pi}{g_{FF}} \left[\mu_F \frac{R_F^2}{2} - \frac{1}{2} k_m k_\omega^2 \frac{R_F^4}{4} \right. \\ &\quad \left. - \frac{g_{BF}/g_{BB}}{1 - g_{BF}^2/g_{BB}g_{FF}} \left\{ \left(\mu_B - \frac{g_{BF}}{g_{FF}} \mu_F \right) \frac{R_B^2}{2} - \left(1 - \frac{g_{BF}}{g_{FF}} k_\omega^2 \right) \frac{R_B^4}{8} \right\} \right] \\ k_N &= \frac{2\pi}{g_{FF}} \left(\mu_F \frac{R_F^2}{2} - k_m k_\omega^2 \frac{R_F^4}{8} - \frac{g_{BF}}{2\pi} \right) \end{aligned} \tag{4.51}$$

We have obtained a similar set of equations for the case when $R_B > R_F$. We solve this system of equations for the four unknowns: the chemical potentials μ_B, μ_F and the TF radii R_B, R_F.

Actually, these equations can be solved analytically. After some algebra we get

$$\mu_F^2 = \frac{k_m k_w^2}{\pi} (g_{BF} + g_{FF} k_N) \tag{4.52}$$

$$R_F^2 = \frac{2\mu_F}{k_m k_\omega^2} \tag{4.53}$$

$$\mu_B = \left(g_{BF}\mu_F + \sqrt{(g_{BB}g_{FF} - g_{BF}^2)(g_{FF} - g_{BF}k_m k_\omega^2)/\pi} \right) / g_{FF} \tag{4.54}$$

$$R_B^2 = 2 \frac{g_{FF}\mu_B - g_{BF}\mu_F}{g_{FF} - g_{BF}k_m k_\omega^2} \tag{4.55}$$

For Q3D model, interaction strengths are given and this is the final answer. For Q2D and 2D models the first and the third equation form a set of coupled equations for μ_B and μ_F. We use a non-linear equation solver for two unknowns.

This method will not work when $g_{BB}g_{FF} - g_{BF}^2 < 0$. We identify this as demixing for repulsive and collapse for attractive BF interactions [168].

4.6.4 Gaussian Variational Wave Function for Bosons

Another approximate solution to the problem is provided by considering a Gaussian variational function for bosons and the TF approximation for fermions.

We use the same energy expression except the Weizsacker term,

$$\begin{aligned}\frac{E}{N_B} &= \frac{1}{2}\int \mathrm{d}^2 r \left\{|\nabla\psi_B|^2 + r^2|\psi_B|^2 + g_{BB}|\psi_B|^4\right\} \\ &+ \frac{1}{2}\int \mathrm{d}^2 r \left\{g_{FF}|\psi_F|^4 + r^2 k_m k_\omega^2 |\psi_F|^2\right\} \\ &+ \int \mathrm{d}^2 r\, g_{BF}|\psi_B|^2|\psi_F|^2.\end{aligned} \tag{4.56}$$

and choose the trial wave function for bosons as

$$\psi_B = \sqrt{\frac{2\alpha}{\pi}}\exp[-\alpha r^2] \tag{4.57}$$

where r is scaled by $a_\perp$. We use the TF approximation and the Euler Lagrange equation to obtain the fermion density

$$|\psi_F|^2 = \frac{1}{g_{FF}}\left[\mu_F - k_m k_\omega^2 \frac{r^2}{2} - g_{BF}|\psi_B|^2\right]. \tag{4.58}$$

We find the unknown parameters of this solution, namely the value of α for the boson wave function, the fermion chemical potential μ_F and the TF radius R_F through the following three equations. Note that the boson wave function is properly normalized and we don't introduce a boson chemical potential.

Using the TF radius definition for fermions; $|\psi_F(R_F)|^2 = 0$, we obtain the first equation

$$\mu_F - k_m k_\omega^2 \frac{R_F^2}{2} - g_{BF}\frac{2\alpha}{\pi}\exp[-2\alpha R_F^2] = 0 \tag{4.59}$$

and using the normalization condition $k_N = \int_0^{R_F} 2\pi r \mathrm{d}r|\psi_F|^2$, we get a second equation.

$$1 - \frac{\pi}{k_N g_{FF}}\left(\mu_F - k_m k_\omega^2 \frac{R_F^2}{4}\right)R_F^2 + \frac{g_{BF}}{k_N g_{FF}}(1 - \exp[-2\alpha R_F^2]) = 0 \tag{4.60}$$

Energy as a function of variational parameter α can be calculated as

$$\begin{aligned}\frac{E}{N_B} &= \alpha + \frac{1}{4\alpha} + \frac{g_{BB}}{2\pi}\alpha + \frac{\pi}{2g_{FF}}\mu_F^2 R_F^2 - \frac{\pi k_m k_\omega^2}{24 g_{FF}}R_F^6 \\ &- \frac{g_{BF}^2\alpha}{2\pi g_{FF}}(1 - \exp[-4\alpha R_F^2]) - \frac{g_{BF}k_m k_\omega^2}{4 g_{FF}\alpha}(1 - (1 + 2\alpha R_F^2)\exp[-2\alpha R_F^2])\end{aligned} \tag{4.61}$$

The last equation is obtained by imposing

$$\frac{\partial E}{\partial \alpha} = 0. \tag{4.62}$$

for the energy minimum. This gives

$$\begin{aligned} & 1 - \frac{1}{4\alpha} + \frac{g_{BB}}{2\pi} \\ & - \frac{g_{BF}^2}{2\pi g_{FF}} \left[1 - (1 - 4\alpha R_F^2)\exp(-4\alpha R_F^2)\right] \\ & + \frac{1}{4\alpha^2}\frac{g_{BF}}{g_{FF}} k_m k_\omega^2 \left[1 - (1 + 2\alpha R_F^2 + 4\alpha^2 R_F^4)\exp(-2\alpha R_F^2)\right] = 0 \end{aligned} \tag{4.63}$$

Since the first equation can easily be solved for μ_F, we solve just two equations for R_F and α numerically.

For Q2D and 2D models the interaction strengths must be determined self-consistently with chemical potentials. This can be done by calculating the chemical potential and solving equations for chemical potentials. Since we have a full numerical solution, we have not proceeded along this direction.

4.6.5 Steepest Descent

In the steepest descend algorithm initial trial states are taken and evolved in a direction to minimize the energy. This propagation can be described as an evolution in an imaginary time according to the following equations which evolve the wave functions in the direction of maximum decrease in energy. Time-dependent wave functions $\psi_B(\mathbf{r}, t)$ and $\psi_F(\mathbf{r}, t)$ converge to the ground state as the fictitious time variable t increases. Time evolution is formulated as [169],

$$\frac{\partial}{\partial t}\psi_B(\mathbf{r}, t) = -\frac{\overline{\delta} E}{\overline{\delta}\psi_B(\mathbf{r}, t)} \text{ and } \frac{\partial}{\partial t}\psi_F(\mathbf{r}, t) = -\frac{\overline{\delta} E}{\overline{\delta}\psi_F(\mathbf{r}, t)}, \tag{4.64}$$

where $\overline{\delta}$ is the constrained functional derivative that assures the normalization. By adding the normalization condition to the functional derivative, we get

$$\frac{\delta E}{\delta \psi_B(\mathbf{r}, t)} = H_B \psi_B(\mathbf{r}, t) \text{ and } \frac{\delta E}{\delta \psi_F(\mathbf{r}, t)} = H_F \psi_F(\mathbf{r}, t), \tag{4.65}$$

where H_B and H_F depend non-linearly on ψ_B and ψ_F. Stationary solutions of these equations satisfy the EL equations $H_B\psi_B = \mu_B\psi_B$, $H_F\psi_F = \mu_F\psi_F$.

In practice one chooses an arbitrary time step Δt and iterates the following equations

$$\psi_B(\mathbf{r}, t + \Delta t) \simeq \psi_B(\mathbf{r}, t) - \Delta t H_B\psi_B(\mathbf{r}, t) \tag{4.66}$$

and

$$\psi_F(\mathbf{r}, t + \Delta t) \simeq \psi_F(\mathbf{r}, t) - \Delta t H_F\psi_F(\mathbf{r}, t) \tag{4.67}$$

by normalizing ψ_B and ψ_F at each iteration. This corresponds to linearizing the formal solution to the time derivative. The rate of convergence is controlled by the time step Δt. The virial theorem provides a check for the solutions.

The way we apply this procedure is by representing the wave function on a mesh of N points. This discretization suggests using finite difference formulae for derivatives. Instead we calculate cubic spline coefficients for each interval and thus obtain a representation of the function and its first and second derivatives practically at any point. This functional representation enables one to use available integration subroutines to calculate integrals very easily. Equivalently, we have also used quadrature formulae for each interval [170].

Conjugate Gradient

The representation in the previous section allows one to calculate the energy numerically using the energy functional and numerical integration. One can try to minimize the energy treating the wave function values at N mesh points as unknown variables. Here we use a conjugate gradient subroutine from the program of Werner Krauth [170] using this idea as well. This has the advantage of avoiding the calculation of second derivatives and improves the virial. The differences with steepest descend are usually at the tail of the wave functions or in the case of demixing around the spatial phase boundary where calculation of the derivative is important for the kinetic energy. In general a good representation of the wave function calls for a high number of mesh points, typically $N = 100$. It is also important to start with a good initial guess for the solution. In practice,

we run our program with the steepest algorithm starting from almost arbitrary initial wave functions, e.g. constant non-zero value. The steepest descend is less sensitive to the initial starting point. After steepest descend has converged with reasonable precision (relative change in energy in successive iterations $< 10^{-6}$), we use that solution as an input for the minimization routine which doesn't require the second derivative informations.

4.6.6 2D Interaction Models

Effective Interaction and the Scattering Length

Ultra-cold atomic gas systems have the appealing property that the scattering length a, which characterizes the strength of the interactions, is smaller than the inter-particle separation. When this diluteness condition ($na^3 \ll 1$ in 3D, $na^2 \ll 1$ in 2D) is satisfied the dominant interactions are two-body collisions. Therefore the two-body scattering at low energy is significant in Bose-Einstein condensates.

Two-body interactions at low energies are characterized by their scattering lengths. This is achieved by integrating out the short-wavelength degrees of freedom to obtain an effective interaction among the long-wavelength, low frequency degrees of freedom.

The wave function describing scattering in momentum representation can be written as [167]

$$\psi(\mathbf{k}') = (2\pi)^3\delta(\mathbf{k}' - \mathbf{k}) + \psi_{\rm sc}(\mathbf{k}') \tag{4.68}$$

where $\mathbf{k}, \mathbf{k}'$ are the wave vector on incident and scattered waves. This wave function satisfies the Scrödinger equation

$$\left(\frac{\hbar^2 k^2}{2m_r} - \frac{\hbar^2 k'^2}{2m_r}\right)\psi_{\rm sc}(\mathbf{k}') = U(\mathbf{k}, \mathbf{k}') + \frac{1}{V}\sum_{\mathbf{k}''} U(\mathbf{k}', \mathbf{k}'')\psi_{\rm sc}(\mathbf{k}''). \tag{4.69}$$

with $U(\mathbf{k}, \mathbf{k}')$ being the Fourier transform of the two-body interaction and m_r being the reduced mass of the scattering particles. This equation may be written

as

$$\psi_{\rm sc}(\mathbf{k}') = \left(\frac{\hbar^2 k^2}{2m_r} - \frac{\hbar^2 k'^2}{2m_r} + i\delta\right)^{-1} T(\mathbf{k}', \mathbf{k}; E = \hbar^2 k^2/2m_r) \tag{4.70}$$

where the infinitesimal imaginary part $i\delta$ ensures that only outgoing waves are present and the T matrix satisfies the so-called Lippmann-Schrödinger equation

$$T(\mathbf{k}', \mathbf{k}; E) = U(\mathbf{k}', \mathbf{k}) + \frac{1}{V}\sum_{\mathbf{k}''} U(\mathbf{k}', \mathbf{k}'')\left(E - \frac{\hbar^2 k''^2}{2m_r} + i\delta\right)^{-1} T(\mathbf{k}'', \mathbf{k}; E) \tag{4.71}$$

The scattering length a is related to the asymptotic from of the scattered wave function by

$$\psi_{\rm sc} = 1 - \frac{a}{r} \tag{4.72}$$

and zeroth order phase shift $\delta_0 = -ka$ (s-wave scattering) which dominates the scattering cross section.

From the expression of $\psi_{\rm sc}$ in terms of the T-matrix we can relate the T matrix at zero energy by the expression

$$T(0, 0; 0) = \frac{2\pi\hbar^2}{m_r} a \tag{4.73}$$

In the Born approximation, only the first term is taken in the Lippman-Schwinger equation and we find

$$U(0) = \frac{2\pi\hbar^2}{m_r} a_{\rm Born} \tag{4.74}$$

Thus the T matrix may be regarded as an effective interaction. Born approximation is valid at large distances. The correlation effects at short distances have been implicitly taken into account by replacing $U(0)$ by T. The effective interaction may be used in place of the bare interaction to make precise calculations for dilute systems to obtain energies in mean-field calculations.

The two-body T matrix is still an approximate description of the interaction because the scattering occurs in the presence of the surrounding particles rather than in a vacuum. The collision is properly described by a many-body T-matrix. In 3D the many-body T-matrix leads to a relatively small correction to the two-body T-matrix but in two dimensions the two-body T-matrix vanishes in the zero-energy, zero-momentum limit and many body effects are of greater importance [161].

In practice, a 2D system is created by applying a tight confinement along one direction so that the gas is kinematically 2D and the particles undergo zero point oscillations in the frozen direction. In such a quasi-2D situation, the scattering length depends on the width of the system in the third direction [171].

We provide expressions in dimensionless form for our units for three regimes as discussed before.

Quasi-3D Scattering

In this regime, the effective interaction strengths can be obtained by multiplying the $3D$ values $g_{BB}^{3D} = 4\pi\hbar^2 a/m_B$ with a factor $|\phi(0)|^2 = 1/\sqrt{2\pi}a_z$. This is obtained by assuming that the motion in the z-direction is frozen in the ground state of the harmonic potential with trapping frequency ω_z and integrating the 3D GP equation over z (after multiplying with $\phi^*(z)$ in the spirit of taking an expectation value. The chemical potential μ gets shifted by $\hbar\omega_z/2$). Assuming the profile for fermions we apply the same idea to boson-fermion interaction $g_{BF}^{3D} = 2\pi\hbar^2 a/m_{BF}$, where m_{BF} is the reduced mass for the boson and fermion pair.

$$g_{BB} = \frac{2\sqrt{2\pi}\hbar^2}{m_B}\frac{a_{BB}}{a_z} \text{ and } g_{BF} = \frac{\sqrt{2\pi}\hbar^2}{m_{BF}}\frac{a_{BF}}{a_z}, \tag{4.75}$$

The corresponding dimensionless forms giving the values in our units are

$$g_{BB} = 2\sqrt{2\pi}N_B\frac{a_{BB}}{a_z} \text{ and } g_{BF} = \frac{\sqrt{2\pi}N_B}{m_{BF}}\frac{a_{BF}}{a_z} \tag{4.76}$$

where $m_{BF} = k_m/(1+k_m)$.

Strictly-2D Scattering

In the strictly 2D regime, the interaction strengths do not depend on the parameters in the z-direction but have a logarithmic dependence on density which is approximated here with a constant chemical potential.

$$g_{BB} = \frac{-4\pi\hbar^2}{m_B}\frac{1}{\ln\left[\mu_B m_B a_{BB}^2/4\hbar^2\right]} \tag{4.77}$$

and similarly,

$$g_{BF} = \frac{-2\pi\hbar^2}{m_{BF}} \frac{1}{\ln\left[(\mu_B + \mu_F) m_{BF} a_{BF}^2 / 4\hbar^2\right]} \tag{4.78}$$

where scattering lengths $a_{BB} = a_{BB}^{2D}$ and $a_{BF} = a_{BF}^{2D}$ are in principle 2D scattering lengths. In our approach we take these to be the limiting values of the crossover model discussed in the next section.

In the units we use, i.e. in terms of scaled quantities,

$$g_{BB} = -4\pi N_B \frac{1}{\log(\mu_B a_{BB}^2/4)} \tag{4.79}$$

$$g_{BF} = -2\pi N_B \frac{1}{m_{BF}} \frac{1}{\log((\mu_B + \mu_F) m_{BF} a_{BF}^2/4)} \tag{4.80}$$

where $m_{BF} = k_m/(1 + k_m)$.

In this regime the interaction parameters must be determined self-consistently. The way the equations are written above suggest to solve for wave functions for given values of g_{BB} and g_{BF}, then calculate chemical potentials

$$\mu_B = \int \mathrm{d}^2 r \left\{ \frac{1}{2}|\nabla\psi_B|^2 + \frac{1}{2} r^2 |\psi_B|^2 + g_{BB}|\psi_B|^4 + g_{BF}|\psi_F|^2|\psi_B|^2 \right\}$$

and

$$\mu_F = \frac{1}{k_N} \int \mathrm{d}^2 r \left\{ \frac{\lambda_W}{k_m} \frac{1}{2} |\nabla\psi_F|^2 + k_m k_\omega^2 \frac{1}{2} r^2 |\psi_F|^2 + g_{FF}|\psi_F|^4 + g_{BF}|\psi_F|^2|\psi_B|^2 \right\}$$

and check whether the expressions for g_{BB} and g_{BF} are satisfied. To follow common practice we start with initial chemical potentials, calculate g's and then calculate chemical potentials using the obtained wave functions and require self-consistency. Note that in this regime nothing depends on the value of ω_z, i.e. on the value of λ.

Quasi-2D Scattering

In this crossover regime ($a_z \gtrsim a_{BB}, a_{BF}$) another model for the scattering length expresses the 2D scattering length in terms of the 3D scattering length [165]. Substituting

$$a_{2D} = 2\sqrt{2}\sqrt{\frac{\pi}{B}} a_z e^{-\sqrt{\pi/2}\frac{a_z}{a_{3D}}} \tag{4.81}$$

in the coupling strength expressions for strictly $2D$ regime with $B \approx 0.915$, the coupling strengths now become [161]

$$g_{BB} = \frac{\frac{2\sqrt{2\pi}\hbar^2}{m_B}\frac{a_{BB}}{a_z}}{1 + \frac{1}{\sqrt{2\pi}}\frac{a_{BB}}{a_z}\log(B\hbar^2/2\pi\mu_B m_B a_z^2)} \tag{4.82}$$

and

$$g_{BF} = \frac{\frac{\sqrt{2\pi}\hbar^2}{m_{BF}}\frac{a_{BF}}{a_z}}{1 + \frac{1}{\sqrt{2\pi}}\frac{a_{BF}}{a_z}\log(B\hbar^2/2\pi(\mu_B+\mu_F) m_{BF} a_z^2)} \tag{4.83}$$

In our units

$$g_{BB} = \frac{2\sqrt{2\pi}N_B\frac{a_{BB}}{a_z}}{1 + \frac{1}{\sqrt{2\pi}}\frac{a_{BB}}{a_z}\log(\lambda B/2\pi\mu_B)} \tag{4.84}$$

$$g_{BF} = \frac{\frac{\sqrt{2\pi}}{m_{BF}}N_B\frac{a_{BF}}{a_z}}{1 + \frac{1}{\sqrt{2\pi}}\frac{a_{BF}}{a_z}\log(\lambda B/2\pi(\mu_B+\mu_F) m_{BF})} \tag{4.85}$$

where now $m_{BF} = k_m/(1+k_m)$ etc. are dimensionless.

4.6.7 System Parameters

Li-Li Mixture

For ^{6}Li-^{7}Li mixture, we use the following values $m_B/m_F = 7/6$, $N_B = N_F = 10^4$, $\omega_B/2\pi = 4000\,Hz$, $\omega_F/2\pi = 3520\,Hz$ and the scattering lengths are $a_{BB} = 5.1a_0$ and $a_{BF} = 38a_0$ [143]. a_0 is the Bohr radius. In our program length unit is $a_\perp$. We need the following ratio for conversion.

$$\begin{aligned} \frac{a_\perp}{a_0} &= 0.114 \times 10^5 \\ a_\perp &= 0.60\,\mu m \end{aligned} \tag{4.86}$$

So for $a_z = a_{BF}$ we have

$$\lambda = \frac{\omega_z}{\omega_\perp} = \frac{a_\perp^2}{a_z^2} = \left(\frac{0.114 \times 10^5 a_0}{38 a_0}\right)^2 = 9 \times 10^4 \tag{4.87}$$

$$a_{BB} = 5.1a_0 = 5.1\frac{a_0}{a_\perp}a_\perp = \frac{5.1}{0.114 \times 10^5}a_\perp = 4.473 \times 10^{-4}a_\perp \tag{4.88}$$

$$a_{BF} = 38a_0 = 38\frac{a_0}{a_\perp}a_\perp = \frac{38}{0.114 \times 10^5}a_\perp = 3.333 \times 10^{-3}a_\perp \tag{4.89}$$

We always have

$$a_z = \frac{1}{\sqrt{\lambda}}\, a_\perp \tag{4.90}$$

K-Rb Mixture

For ^{40}K-^{87}Rb mixture we use the same parameters with the experiment of Ospelkaus et al. [166]: $a_{BF} = -284a_0$, $a_{BB} = 110a_0$, $\omega_B/2\pi = 257\,Hz$, $\omega_F/2\pi = 378\,Hz$, $N_B = 10^6, N_F = 5\times 10^5$. We have

$$\begin{aligned} \frac{a_\perp}{a_0} &= 0.1270\times 10^5 \\ a_\perp &= 0.67\,\mu m \end{aligned} \tag{4.91}$$

So with $a_{BF}/a_z = 0.1$ we have

$$\lambda = \frac{\omega_z}{\omega_\perp} = \frac{a_\perp^2}{a_z^2} = \frac{(0.1270\times 10^5)^2}{(284/0.1)^2} \approx 20 \tag{4.92}$$

$$a_{BB} = 110a_0 = 110\frac{a_0}{a_\perp}a_\perp = \frac{110}{0.1270\times 10^5}a_\perp = 8.657\times 10^{-3}a_\perp \tag{4.93}$$

$$a_{BF} = -284a_0 = -284\frac{a_0}{a_\perp}a_\perp = \frac{-284}{0.1270\times 10^5}a_\perp = -2.235\times 10^{-2}a_\perp \tag{4.94}$$

Chapter 5

Concluding Remarks and Outlook

In this thesis we have studied three two-dimensional many-body systems and discussed some effects of the many-body nature of the physical system.

In Chapter 2 the two-dimensional electron gas under an in-plane magnetic field was considered. The parallel field couples only to the spin of the electrons. We calculate the critical magnetic field fully polarizing the electron spins using two expressions for the ground state energy and compare our results with those of approximate theories, namely Hartree-Fock and random phase approximation. The main result is that using the QMC based ground-state energy expression [50] results in a qualitatively different phase transition to the ferromagnetic state at the critical field for a density range corresponding to $7 < r_s < 20$. In this regime the transition is second order whereas HF approximation and RPA predict a first order transition throughout the whole density range. This empasizes that the QMC based parametrization of the correlation energy needs to be checked carefully. The onset of full spin polarization shows also in the compressibility measurement which can be used as an alternative way to determine the critical field. Depending on the nature of the transition, the compressibility displays a kink or jump behavior at the critical field. In order to make contact with experiments one should include effects of the finite thickness of the two-dimensional layer and disorder.

The excitonic condensation in an electron-hole bilayer system composed of a two-dimensional electron layer separated from a similar hole layer by a distance was studied in Chapter 3. We consider a sample system of two layers in GaAs separated by a barrier layer where the electron and hole densities can be controlled independently and study s-wave pairing between electrons and holes as a function of density and population difference using mean-field theory. We ignore the spin degrees of freedom. Solving the relevant energy gap equations we compare the energy of the condensed phase called Sarma phase with that of the normal state which is the sum of the electron and hole Fermi liquids described by the Hartree-Fock solution. We include both inter- and intra-layer interactions generalizing earlier work which did not include in-plane interactions [102]. In this way the phase boundary for the ground state is established in the density - population polarization plane. The local stability of the Sarma phase is checked by calculating the superfluid mass density. We find that with bare Coulomb interactions the Sarma phase is always locally stable due to a logarithmic singularity at zero temperature. Employing a simple model of screening which introduces a finite cut-off to the Coulomb interaction, we find that some regions in the phase space become unstable. We interpret this as an instability towards an FFLO phase. Together with intra-plane interactions, the phase diagram in the crossover regime from the weakly interacting high density BCS limit to the strongly interacting BEC of dilute excitons has room for various phases. The topologically different S1 and S2 Sarma phases and FFLO are present with the inclusion of screening and intra-layer interactions. On the other hand, without any screening there is no instability towards FFLO and turning off intra-plane interactions the phase diagram does not show an S2 state. Currently, the experimental situation allows these systems to be realized and tested. Quantitative comparison would require a more realistic model of screening and inclusion of spin degrees of freedom which may enter non-trivially when there are spin dependent interactions such as spin-orbit coupling.

In Chapter 3 we consider a system of two-dimensional bosonic and fermionic ultra-cold atoms and study the effects of scattering and geometry on the

density profiles and stability of the mixture. The bosons are taken to be in the Bose condensed state and the fermion component is assumed to be spin-polarized. We use a mean-field model for the boson-boson and boson-fermion interactions which is valid at low temperatures and densities. The confinement in the third direction which makes the system kinematically two-dimensional was shown to have an important effect on the energetics of a single BEC with attractive interactions [165]. Motivated by this observation we study the dimensional crossover of a boson-fermion mixture from a quasi-three dimensional situation where the scattering events are still three dimensional to a strictly two-dimensional limit where the collisions essentially take place in the plane. We calculate the density profiles of a ^{6}Li-^{7}Li mixture with positive scattering lengths (repulsive interactions) in 3D and of a ^{40}K-^{87}Rb mixture with a negative boson-fermion scattering length as the trap asymmetry is increased. We observe phase separation and collapse as the interactions change due to increasing confinement. We find that a mixture with attractive boson-fermion interactions can be made stable by going to a two-dimensional limit. It would be interesting to extend this work to Bose-Fermi mixture created from two fermionic species with population imbalance where the minority components can pair to from composite bosons. This system will be analogous to the electron-hole bilayer having unequal densities considered in Chapter 2 with short range interactions. We are planning to study similar effects in rotating traps with vortex states.

Bibliography

[1] G. Giuliani and G. Vignale, *Quantum Theory of the Electron Liquid*. New York : Cambridge University Press, Cambridge, UK, 2005.

[2] T. Ando, A. Fowler, and F. Stern, "Electronic-Properties of Two-Dimensional Systems," *Reviews of Modern Physics* **54**, 437 (1982).

[3] A. H. MacDonald, "Introduction to the physics of the quantum hall regime," 1994. `arXiv.org:cond-mat/9410047`.

[4] H. L. Stormer, D. C. Tsui, and A. C. Gossard, "The fractional quantum hall effect," *Review of Modern Physics* **71**, S298 (1999).

[5] S. M. Girvin, "The quantum hall effect: Novel excitations and broken symmetries," 2000. `arXiv.org:cond-mat/9907002`.

[6] E. Abrahams, S. Kravchenko, and M. Sarachik, "Metallic behavior and related phenomena in two dimensions," *Reviews of Modern Physics* **73**, 251 (2001).

[7] S. Kravchenko and M. Sarachik, "Metal-insulator transition in two-dimensional electron systems," *Reports on Progress in Physics* **67**, 1 (2004).

[8] P. B. Littlewood, *Problems of Condensed Matter Physics: Quantum Coherence Phenomena in Electron-Hole and Coupled Matter-Light Systems*. Oxford University Press, 2008.

[9] J. A. Seamons, C. P. Morath, J. L. Reno, and M. P. Lilly, "Coulomb drag in the exciton regime in electron-hole bilayers," *Physical Review Letters* **102**, 026804 (2009).

[10] A. F. Croxall, K. D. Gupta, C. A. Nicoll, M. Thangaraj, H. E. Beere, I. Farrer, D. A. Ritchie, and M. Pepper, "Anomalous coulomb drag in electron-hole bilayers," *Physical Review Letters* **101**, 246801 (2008).

[11] A. F. Croxall, K. D. Gupta, C. A. Nicoll, H. E. Beere, I. Farrer, D. A. Ritchie, and M. Pepper, "Collective mode driven insulator in an electron-hole bilayer," (2008). `arXiv.org:0812.3319`.

[12] A. L. Subasi and B. Tanatar, "Effects of a parallel magnetic field on the ground-state magnetic properties of a two-dimensional electron gas," *Physical Review B* **78**, 155304 (2008).

[13] A. L. Subasi and B. Tanatar, "Compressibility of a two-dimensional electron gas in a parallel magnetic field," *Solid State Communications* **144**, 521 (2007).

[14] A. L. Subaşi, S. Sevinçli, P. Vignolo, and B. Tanatar, "Two-dimensional boson-fermion mixtures," *Physical Review A* **79**, 063632 (2009).

[15] T. Okamoto, K. Hosoya, S. Kawaji, and A. Yagi, "Spin degree of freedom in a two-dimensional electron liquid," *Physical Review Letters* **82**, 3875 (1999).

[16] A. Shashkin, S. Kravchenko, V. Dolgopolov, and T. Klapwijk, "Indication of the ferromagnetic instability in a dilute two-dimensional electron system," *Physical Review Letters* **87**, 086801 (2001).

[17] V. Pudalov, M. Gershenson, H. Kojima, N. Butch, E. Dizhur, G. Brunthaler, A. Prinz, and G. Bauer, "Low-density spin susceptibility and effective mass of mobile electrons in Si inversion layers," *Physical Review Letters* **88**, 196404 (2002).

[18] S. Vitkalov, M. Sarachik, and T. Klapwijk, "Spin polarization of strongly interacting two-dimensional electrons: The role of disorder," *Physical Review B* **65**, 201106 (2002).

[19] E. Tutuc, S. Melinte, and M. Shayegan, "Spin polarization and g factor of a dilute GaAs two-dimensional electron system," *Physical Review Letters* **88**, 036805 (2002).

[20] E. Tutuc, S. Melinte, E. De Poortere, M. Shayegan, and R. Winkler, "Role of finite layer thickness in spin polarization of GaAs two-dimensional electrons in strong parallel magnetic fields," *Physical Review B* **67**, 241309 (2003).

[21] J. Zhu, H. Stormer, L. Pfeiffer, K. Baldwin, and K. West, "Spin susceptibility of an ultra-low-density two-dimensional electron system," *Physical Review Letters* **90**, 056805 (2003).

[22] K. Vakili, Y. Shkolnikov, E. Tutuc, E. De Poortere, and M. Shayegan, "Spin susceptibility of two-dimensional electrons in narrow AlAs quantum wells," *Physical Review Letters* **92**, 226401 (2004).

[23] Y. Shkolnikov, K. Vakili, E. De Poortere, and M. Shayegan, "Dependence of spin susceptibility of a two-dimensional electron system on the valley degree of freedom," *Physical Review Letters* **92**, 246804 (2004).

[24] Y. Tan, J. Zhu, H. Stormer, L. Pfeiffer, K. Baldwin, and K. West, "Spin susceptibility of a two-dimensional electron system in GaAs towards the weak interaction region," *Physical Review B* **73**, 045334 (2006).

[25] W. Pan, D. Tsui, and B. Draper, "Mass enhancement of two-dimensional electrons in thin-oxide Si-MOSFET's," *Physical Review B* **59**, 10208 (1999).

[26] O. Prus, Y. Yaish, M. Reznikov, U. Sivan, and V. Pudalov, "Thermodynamic spin magnetization of strongly correlated

two-dimensional electrons in a silicon inversion layer," *Physical Review B* **67**, 205407 (2003).

[27] A. Shashkin, S. Anissimova, M. Sakr, S. Kravchenko, V. Dolgopolov, and T. Klapwijk, "Pauli spin susceptibility of a strongly correlated two-dimensional electron liquid," *Physical Review Letters* **96**, 036403 (2006).

[28] S. V. Kravchenko, A. A. Shashkin, S. Anissimova, A. Venkatesan, M. R. Sakr, V. T. Dolgopolov, and T. M. Klapwijk, "Thermodynamic magnetization of a strongly correlated two-dimensional electron system," *Annals of Physics* **321**, 1588 (2006).

[29] H. Boukari, F. Perez, D. Ferrand, P. Kossacki, B. Jusserand, and J. Cibert, "Spin susceptibility enhancement in a two-dimensional hole gas," *Physical Review B* **73**, 115320 (2006).

[30] Y. Zhang and S. Das Sarma, "Nonlinear 2D spin susceptibility in a finite magnetic field: Spin-polarization dependence," *Physical Review Letters* **96**, 196602 (2006).

[31] A. K. Rajagopal and J. C. Kimball, "Correlations in a two-dimensional electron system," *Physical Review B* **15**, 2819 (1977).

[32] A. K. Rajagopal, S. P. Singhal, M. Banerjee, and J. C. Kimball, "Correlations in two-dimensional electron systems. magnetic properties," *Physical Review B* **17**, 2262 (1978).

[33] R. Asgari, B. Davoudi, and M. Tosi, "Analytic theory of correlation energy and spin polarization in the 2D electron gas," *Solid State Communications* **131**, 301 (2004).

[34] B. Davoudi and M. Tosi, "Spin polarization in a two-dimensional electron gas," *Physica B-Condensed Matter* **322**, 124 (2002).

[35] R. Asgari, A. Esmailian, and B. Tanatar, "Effective electron-electron interactions and magnetic phase transition in a two-dimensional electron liquid," *Solid State Communications* **141**, 595 (2007).

[36] F. Perrot and M. Dharma-wardana, "2D electron gas at arbitrary spin polarizations and coupling strengths: Exchange-correlation energies, distribution functions, and spin-polarized phases," *Physical Review Letters* **87**, 206404 (2001).

[37] Y. Zhang and S. Das Sarma, "Exchange instabilities in electron systems: Bloch versus Stoner ferromagnetism," *Physical Review B* **72**, 115317 (2005).

[38] Y. Zhang and S. Das Sarma, "Temperature and magnetization-dependent band-gap renormalization and optical many-body effects in diluted magnetic semiconductors," *Physical Review B* **72**, 125303 (2005).

[39] J. Terada and T. Ando, "Many-body effects in spin-polarized two-dimensional electron gas," *Physica E-Low-Dimensional Systems & Nanostructures* **34**, 367 (2006).

[40] L. Juri and P. Tamborenea, "Spontaneous spin polarization in doped semiconductor quantum wells," *European Physical Journal B* **45**, 9 (2005).

[41] M. W. C. Dharma-wardana, "Coulomb interactions of massless Dirac fermions in graphene; pair-distribution functions and exchange-driven spin-polarized phases," *Solid State Communications* **140**, 4 (2006).

[42] M. W. C. Dharma-wardana, "Ground state of clean and defective graphene: Coulomb interactions, pair-distribution functions, and spin-polarized phases of massless dirac fermions," *Physical Review B* **75**, 075427 (2007).

[43] A. Qaiumzadeh and R. Asgari, "Stoner ferromagnetic phase of a graphene in the presence of an in-plane magnetic field," *arXiv.org:0906.2882* (2009).

[44] S. Ilani, A. Yacoby, D. Mahalu, and H. Shtrikman, "Unexpected behavior of the local compressibility near the B=0 metal-insulator transition," *Physical Review Letters* **84**, 3133 (2000).

[45] S. Dultz and H. Jiang, "Thermodynamic signature of a two-dimensional metal-insulator transition," *Physical Review Letters* **84**, 4689 (2000).

[46] M. Rahimi, M. Sakr, S. Kravchenko, S. Dultz, and H. Jiang, "Compressibility of a two-dimensional hole gas in a tilted magnetic field," *Physical Review B* **67**, 081302 (2003).

[47] G. Allison, E. A. Galaktionov, A. K. Savchenko, S. S. Safonov, M. M. Fogler, M. Y. Simmons, and D. A. Ritchie, "Thermodynamic density of states of two-dimensional GaAs systems near the apparent metal-insulator transition," *Physical Review Letters* **96**, 216407 (2006).

[48] J. Eisenstein, L. Pfeiffer, and K. West, "Negative Compressibility of Interacting 2-Dimensional Electron and Quasi-Particle Gases," *Physical Review Letters* **68**, 674 (1992).

[49] B. Tanatar and D. Ceperley, "Ground-State of The Two-Dimensional Electron-Gas," *Physical Review B* **39**, 5005 (1989).

[50] C. Attaccalite, S. Moroni, P. Gori-Giorgi, and G. Bachelet, "Correlation energy and spin polarization in the 2D electron gas," *Physical Review Letters* **88**, 256601 (2002).

[51] A. Ghosh, C. Ford, M. Pepper, H. Beere, and D. Ritchie, "Possible evidence of a spontaneous spin polarization in mesoscopic two-dimensional electron systems," *Physical Review Letters* **92**, 116601 (2004).

[52] R. Winkler, E. Tutuc, S. Papadakis, S. Melinte, M. Shayegan, D. Wasserman, and S. Lyon, "Anomalous spin polarization of GaAs two-dimensional hole systems," *Physical Review B* **72**, 195321 (2005).

[53] C. Aku-Leh, F. Perez, B. Jusserand, D. Richards, W. Pacuski, P. Kossacki, M. Menant, and G. Karczewski, "Measuring the spin polarization and Zeeman energy of a spin-polarized electron gas: Comparison between Raman scattering and photoluminescence," *Physical Review B* **76**, 155416 (2007).

[54] S. De Palo, M. Botti, S. Moroni, and G. Senatore, "Effects of thickness on the spin susceptibility of the two dimensional electron gas," *Physical Review Letters* **94**, 226405 (2005).

[55] D. Varsano, S. Moroni, and G. Senatore, "Spin-polarization transition in the two-dimensional electron gas," *Europhysics Letters* **53**, 348 (2001).

[56] G. Senatore, S. Moroni, and D. Varsano, "Spin effects in the 2D electron gas," *Solid State Communications* **119**, 333 (2001).

[57] P. Gori-Giorgi, C. Attaccalite, S. Moroni, and G. Bachelet, "Two-dimensional electron gas: Correlation energy versus density and spin polarization," *International Journal of Quantum Chemistry* **91**, 126 (2003).

[58] F. Zong, C. Lin, and D. Ceperley, "Spin polarization of the low-density three-dimensional electron gas," *Physical Review E* **66**, 036703 (2002).

[59] S. Chesi and G. F. Giuliani, "Correlation energy in a spin-polarized two-dimensional electron liquid in the high-density limit," *Physical Review B* **75**, 153306 (2007).

[60] G. Zala, B. Narozhny, I. Aleiner, and V. Fal'ko, "Two-dimensional electron gas near full polarization," *Physical Review B* **69**, 075306 (2004).

[61] J. Bardeen, L. N. Cooper, and J. R. Schrieffer, "Theory of superconductivity," *Phys. Rev.* **108**, 1175 (1957).

[62] D. M. Eagles, "Possible pairing without superconductivity at low carrier concentrations in bulk and thin-film superconducting semiconductors," *Phys. Rev.* **186**, 456 (1969).

[63] A. J. Leggett *Modern Trends in the Theory of Condensed Matter* 13 (1980).

[64] P. Nozieres and S. Schmitt-Rink, "Bose Condensation in an Attractive Fermion Gas - From Weak to Strong Coupling Superconductivity," *Journal of Low Temperature Physics* **59**, 195 (1985).

[65] C. A. R. Sa de Melo, "When fermions become bosons: Pairing in ultracold gases," *Physics Today* (2008).

[66] T. Ho, "Arrival of the fermion superfluid," *Science* **305**, 1114 (2004).

[67] C. Chin, M. Bartenstein, A. Altmeyer, S. Riedl, S. Jochim, J. Denschlag, and R. Grimm, "Observation of the pairing gap in a strongly interacting Fermi gas," *Science* **305**, 1128 (2004).

[68] J. Kinnunen, M. Rodriguez, and P. Torma, "Pairing gap and in-gap excitations in trapped fermionic superfluids," *Science* **305**, 1131 (2004).

[69] Y. Shin, M. W. Zwierlein, C. H. Schunck, A. Schirotzek, and W. Ketterle, "Observation of phase separation in a strongly interacting imbalanced Fermi gas," *Physical Review Letters* **97**, 030401 (2006).

[70] M. Zwierlein, A. Schirotzek, C. Schunck, and W. Ketterle, "Fermionic superfluidity with imbalanced spin populations," *Science* **311**, 492 (2006).

[71] C. H. Schunck, Y. Shin, A. Schirotzek, M. W. Zwierlein, and W. Ketterle, "Pairing without superfluidity: The ground state of an imbalanced Fermi mixture," *Science* **316**, 867 (2007).

[72] W. Li, G. B. Partridge, Y. A. Liao, and R. G. Hulet, "Pairing of a trapped Fermi gas with unequal spin populations," *Nuclear Physics A* **790**, 88C (2007).

[73] G. J. Conduit, P. H. Conlon, and B. D. Simons, "Superfluidity at the BEC-BCS crossover in two-dimensional Fermi gases with population and mass imbalance," *Physical Review A* **77**, 053617 (2008).

[74] M. Iskin and C. A. R. S. de Melo, "Two-species fermion mixtures with population imbalance," *Physical Review Letters* **97**, 100404 (2006).

[75] M. Iskin and C. A. R. S. de Melo, "Mixtures of ultracold fermions with unequal masses," *Physical Review A* **76**, 013601 (2007).

[76] K. B. Gubbels, M. W. J. Romans, and H. T. C. Stoof, "Sarma phase in trapped unbalanced Fermi gases," *Physical Review Letters* **97**, 210402 (2006).

[77] H. Caldas and A. L. Mota, "Temperature effects in a Fermi gas with population imbalance," *Journal of Statistical Mechanics-Theory and Experiment* P08013 (2008).

[78] K. B. Gubbels and H. T. C. Stoof, "Renormalization group theory for the imbalanced fermi gas," *Physical Review Letters* **100**, 140407 (2008).

[79] J. M. Blatt, K. W. Böer, and W. Brandt, "Bose-einstein condensation of excitons," *Phys. Rev.* **126**, 1691 (1962).

[80] D. Jérome, T. M. Rice, and W. Kohn, "Excitonic insulator," *Phys. Rev.* **158**, 462 (1967).

[81] L. V. Keldysh and Y. V. Kopaev *Sov. Phys. Solid State* **6**, 2219 (1965).

[82] L. V. Keldysh and A. N. Kozlov *JETP* **27**, 521 (1968).

[83] C. Comte and P. Nozieres, "Exciton Bose Condensation - The Ground-State of an Electron-Hole Gas 1. Mean Field Description of a Simplified Model," *Journal de Physique* **43**, 1069 (1982).

[84] P. Nozieres and C. Comte, "Exciton Bose Condensation - The Ground-State of an Electron-Hole Gas 2. Spin States, Screening and Band-Structure Effects," *Journal de Physique* **43**, 1083 (1982).

[85] Y. E. Lozovik and V. I. Yudson, "Feasibility of superfluidity of paired spatially separated electrons and holes; a new superconductivity mechanism," *JETP Letters* **22**, 274 (1975).

[86] Y. E. Lozovik and V. I. Yudson *Sov. Phys. JETP* **44**, 389 (1976).

[87] L. Butov, A. Gossard, and D. Chemla, "Macroscopically ordered state in an exciton system," *Nature* **418**, 751 (2002).

[88] A. T. Hammack, M. Griswold, L. V. Butov, L. E. Smallwood, A. L. Ivanov, and A. C. Gossard, "Trapping of cold excitons in quantum well structures with laser light," *Physical Review Letters* **96**, 227402 (2006).

[89] S. Yang, A. T. Hammack, M. M. Fogler, L. V. Butov, and A. C. Gossard, "Coherence length of cold exciton gases in coupled quantum wells," *Physical Review Letters* **97**, 187402 (2006).

[90] M. Kellogg, J. Eisenstein, L. Pfeiffer, and K. West, "Vanishing Hall resistance at high magnetic field in a double-layer two-dimensional electron system," *Physical Review Letters* **93**, 036801 (2004).

[91] E. Tutuc, M. Shayegan, and D. Huse, "Counterflow measurements in strongly correlated GaAs hole bilayers: Evidence for electron-hole pairing," *Physical Review Letters* **93**, 036802 (2004).

[92] J. Eisenstein and A. MacDonald, "Bose-Einstein condensation of excitons in bilayer electron systems," *Nature* **432**, 691 (2004).

[93] J. Eisenstein, "Half full or half empty?," *Science* **305**, 950–951 (2004).

[94] M. Kellogg, J. P. Eisenstein, L. N. Pfeiffer, and K. W. West, "Bilayer quantum hall systems at $\nu t = 1$: Coulomb drag and the transition from weak to strong interlayer coupling," *Phys. Rev. Lett.* **90**, 246801 (2003).

[95] L. V. Butov, A. Zrenner, G. Abstreiter, G. Böhm, and G. Weimann, "Condensation of indirect excitons in coupled alas/gaas quantum wells," *Phys. Rev. Lett.* **73**, 304 (1994).

[96] P. Littlewood, "Condensates Made of Light," *Science* **316**, 989 (2007).

[97] J. Kasprzak, M. Richard, S. Kundermann, A. Baas, P. Jeambrun, J. M. J. Keeling, F. M. Marchetti, M. H. Szymanska, R. Andre, J. L. Staehli, V. Savona, P. B. Littlewood, B. Deveaud, and L. S. Dang, "Bose-Einstein condensation of exciton polaritons," *Nature* **443**, 409 (2006).

[98] R. Balili, V. Hartwell, D. Snoke, L. Pfeiffer, and K. West, "Bose-einstein condensation of microcavity polaritons in a trap," *Science* **316**, 1007 (2007).

[99] X. Zhu, P. Littlewood, M. Hybertsen, and T. Rice, "Exciton Condensate in Semiconductor Quantum-Well Structures," *Physical Review Letters* **74**, 1633 (1995).

[100] P. Littlewood and X. Zhu, "Possibilities for exciton condensation in semiconductor quantum-well structures," *Physica Scripta* **T68**, 56 (1996).

[101] Z. Gortel and L. Swierkowski, "Superfluid ground state in electron-hole double layer systems," *Surface Science* **362**, 146 (1996).

[102] P. Pieri, D. Neilson, and G. C. Strinati, "Effects of density imbalance on the BCS-BEC crossover in semiconductor electron-hole bilayers," *Physical Review B* **75**, 113301 (2007).

[103] G. Sarma, "On the influence of a unifom exchange field acting on the spins of the conduction electrons in a superconductor," *J. Phys. Chem. Solids* **24**, 1029 (1963).

[104] L. H. Ho, A. P. Micolich, A. R. Hamilton, and O. P. Sushkov, "Ground-plane screening of coulomb interactions in 2d systems – how

effectively can one 2d system screen interactions in another?," *arXiv.org:0904.3786* (2009).

[105] C. H. Zhang and Y. N. Joglekar, "Excitonic condensation of massless fermions in graphene bilayers," *Physical Review B* **77**, 233405 (2008).

[106] M. Y. Kharitonov and K. B. Efetov, "Electron screening and excitonic condensation in double-layer graphene systems," *Physical Review B* **78**, 241401 (2008).

[107] Y. E. Lozovik and A. A. Sokolik, "Electron-hole pair condensation in a graphene bilayer," *JETP Letters* **87**, 55 (2008).

[108] R. Bistritzer and A. H. MacDonald, "Influence of Disorder on Electron-Hole Pair Condensation in Graphene Bilayers," *Physical Review Letters* **101**, 256406 (2008).

[109] X. Zhu, M. Hybertsen, and P. Littlewood, "Electron-hole system revisited: A variational quantum Monte Carlo study," *Physical Review B* **54**, 13575 (1996).

[110] S. De Palo, F. Rapisarda, and G. Senatore, "Excitonic condensation in a symmetric electron-hole bilayer," *Physical Review Letters* **88**, 206401 (2002).

[111] G. Senatore and S. De Palo, "Correlation effects in low dimensional electron systems: the electron-hole bilayer," *Contributions to Plasma Physics* **43**, 363 (2003).

[112] J. Shumway and D. Ceperley, "Quantum monte carlo simulations of exciton condensates," *Solid State Communications* **134**, 19 (2005). Spontaneous Coherence in Excitonic Systems.

[113] G. E. Astrakharchik, J. Boronat, J. Casulleras, Giorgini, and S., "Equation of state of a fermi gas in the bec-bcs crossover: A quantum monte carlo study," *Phys. Rev. Lett.* **93**, 200404 (2004).

[114] J. Carlson, S.-Y. Chang, V. R. Pandharipande, and K. E. Schmidt, "Superfluid fermi gases with large scattering length," *Phys. Rev. Lett.* **91**, 050401 (2003).

[115] S. Y. Chang, V. R. Pandharipande, J. Carlson, and K. E. Schmidt, "Quantum monte carlo studies of superfluid fermi gases," *Phys. Rev. A* **70**, 043602(Oct, 2004).

[116] E. Burovski, E. Kozik, N. Prokof'ev, B. Svistunov, and M. Troyer, "Critical temperature curve in bec-bcs crossover," *Physical Review Letters* **101**, 090402 (2008).

[117] A. J. Leggett, *Quantum Liquids, Bose Condensation and Cooper Pairing in Condensed-Matter Systems*. Oxford University Press, 2006.

[118] P. Bedaque, H. Caldas, and G. Rupak, "Phase separation in asymmetrical fermion superfluids," *Physical Review Letters* **91**, 247002 (2003).

[119] H. Caldas, C. Morais, and A. Mota, "Phase transition in asymmetrical superfluids: Equal Fermi surfaces," *Physical Review D* **72**, 045008 (2005).

[120] J. H. Davies, *The Physics of Low-Dimensional Semiconductors, An Introduction*. Cambridge University Press, 1998.

[121] L. Zheng and A. Macdonald, "Correlation in Double-Layer 2-Dimensional Electron-Gas Systems - Singwi-Tosi-Land-Sjolander Theory At B=0," *Physical Review B* **49**, 5522 (1994).

[122] J. A. Seamons, D. R. Tibbetts, J. L. Reno, and M. P. Lilly, "Undoped electron-hole bilayers in a gaas/algaas double quantum well," *Applied Physics Letters* **90**, 052103 (2007). `http://link.aip.org/link/?APL/90/052103/1`.

[123] W. H. Press, B. P. Flannery, S. A. Teukolsky, and W. T. Vetterling, *Numerical Recipes in Fortran*. Cambridge University Press, 1992.

[124] E. Gubankova, W. Liu, and F. Wilczek, "Breached pairing superfluidity: Possible realization in QCD," *Physical Review Letters* **91**, 032001 (2003).

[125] M. Forbes, E. Gubankova, W. Liu, and F. Wilczek, "Stability criteria for breached-pair superfluidity," *Physical Review Letters* **94**, 017001 (2005).

[126] E. Gubankova, A. Schmitt, and F. Wilczek, "Stability conditions and Fermi surface topologies in a superconductor," *Physical Review B* **74**, 064505 (2006).

[127] P. Fulde and R. A. Ferrell, "Superconductivity in a strong spin-exchange field," *Phys. Rev.* **135**, A550 (1964).

[128] A. I. Larkin and Y. N. Ovchinnikov, "Nonuniform state of superconductors," *JETP* **20**, 762 (1965).

[129] A. Truscott, K. Strecker, W. McAlexander, G. Partridge, and R. Hulet, "Observation of Fermi pressure in a gas of trapped atoms," *Science* **291**, 2570 (2001).

[130] F. Schreck, L. Khaykovich, K. Corwin, G. Ferrari, T. Bourdel, J. Cubizolles, and C. Salomon, "Quasipure Bose-Einstein condensate immersed in a Fermi sea," *Physical Review Letters* **87**, 080403 (2001).

[131] Z. Hadzibabic, C. Stan, K. Dieckmann, S. Gupta, M. Zwierlein, A. Gorlitz, and W. Ketterle, "Two-species mixture of quantum degenerate Bose and Fermi gases," *Physical Review Letters* **88**, 160401 (2002).

[132] J. Goldwin, S. Papp, B. DeMarco, and D. Jin, "Two-species magneto-optical trap with K-40 and Rb-87," *Physical Review A* **65**, 021402 (2002).

[133] G. Roati, F. Riboli, G. Modugno, and M. Inguscio, "Fermi-Bose quantum degenerate K-40-Rb-87 mixture with attractive interaction," *Physical Review Letters* **89**, 150403 (2002).

[134] G. Modugno, G. Roati, F. Riboli, F. Ferlaino, R. Brecha, and M. Inguscio, "Collapse of a degenerate Fermi gas," *Science* **297**, 2240 (2002).

[135] T. Fukuhara, S. Sugawa, Y. Takasu, and Y. Takahashi, "All-optical formation of quantum degenerate mixtures," *Physical Review A* **79**, 021601 (2009).

[136] G. Partridge, W. Li, R. Kamar, Y. Liao, and R. Hulet, "Pairing and phase separation in a polarized fermi gas," *Science* **311**, 503 (2006).

[137] C. Ospelkaus, S. Ospelkaus, K. Sengstock, and K. Bongs, "Interaction-driven dynamics of K-40-Rb-87 fermion-boson gas mixtures in the large-particle-number limit," *Physical Review Letters* **96**, 020401 (2006).

[138] M. Zaccanti, C. D'Errico, F. Ferlaino, G. Roati, M. Inguscio, and G. Modugno, "Control of the interaction in a Fermi-Bose mixture," *Physical Review A* **74**, 041605 (2006).

[139] K. Molmer, "Bose condensates and Fermi gases at zero temperature," *Physical Review Letters* **80**, 1804 (1998).

[140] Z. Akdeniz, P. Vignolo, A. Minguzzi, and M. Tosi, "Phase separation in a boson-fermion mixture of lithium atoms," *Journal of Physics B-Atomic Molecular and Optical Physics* **35**, L105–L111(FEB 28, 2002).

[141] R. Roth, "Structure and stability of trapped atomic boson-fermion mixtures," *Physical Review A* **66**, 013614 (2002).

[142] S. Roethel and A. Pelster, "Density and stability in ultracold dilute boson-fermion mixtures," *European Physical Journal B* **59**, 343 (2007).

[143] Z. Akdeniz, P. Vignolo, and M. Tosi, "Boson-fermion demixing in a cloud of lithium atoms in a pancake trap," *Physics Letters A* **331**, 258 (2004).

[144] A. Gorlitz, J. Vogels, A. Leanhardt, C. Raman, T. Gustavson, J. Abo-Shaeer, A. Chikkatur, S. Gupta, S. Inouye, T. Rosenband, and W. Ketterle, "Realization of Bose-Einstein condensates in lower dimensions," *Physical Review Letters* **87**, 130402 (2001).

[145] V. Schweikhard, I. Coddington, P. Engels, V. Mogendorff, and E. Cornell, "Rapidly rotating Bose-Einstein condensates in and near the lowest Landau level," *Physical Review Letters* **92**, 040404 (2004).

[146] D. Rychtarik, B. Engeser, H. Nagerl, and R. Grimm, "Two-dimensional Bose-Einstein condensate in an optical surface trap," *Physical Review Letters* **92**, 173003 (2004).

[147] Y. Colombe, E. Knyazchyan, O. Morizot, B. Mercier, V. Lorent, and H. Perrin, "Ultracold atoms confined in rf-induced two-dimensional trapping potentials," *Europhysics Letters* **67**, 593 (2004).

[148] S. Stock, Z. Hadzibabic, B. Battelier, M. Cheneau, and J. Dalibard, "Observation of phase defects in quasi-two-dimensional Bose-Einstein condensates," *Physical Review Letters* **95**, 190403 (2005).

[149] M. Schick, "Two-dimensional system of hard-core bosons," *Physical Review A* **3**, 1067 (1971).

[150] V. N. Popov, *Functional Integrals in Quantum Field Theory and Statistical Physics*. Dordrecht c1983, Boston, 1966.

[151] U. Al Khawaja, J. Andersen, N. Proukakis, and H. Stoof, "Low dimensional Bose gases," *Physical Review A* **66**, 013615 (2002).

[152] M. Lee, S. Morgan, M. Davis, and K. Burnett, "Energy-dependent scattering and the Gross-Pitaevskii equation in two-dimensional Bose-Einstein condensates," *Physical Review A* **65**, 043617 (2002).

[153] B. Tanatar, A. Minguzzi, P. Vignolo, and M. Tosi, "Density profile of a Bose-Einstein condensate inside a pancake-shaped trap: observational

consequences of the dimensional cross-over in the scattering properties," *Physics Letters A* **302**, 131 (2002).

[154] O. Hosten, P. Vignolo, A. Minguzzi, B. Tanatar, and M. Tosi, "Free expansion of two-dimensional condensates with a vortex," *Journal of Physics B-Atomic Molecular and Optical Physics* **36**, 2455 (2003).

[155] B. van Zyl and E. Zaremba, "Thomas-Fermi-Dirac-von Weizsacker hydrodynamics in laterally modulated electronic systems," *Physical Review B* **59**, 2079 (1999).

[156] D. Jezek, M. Barranco, M. Guilleumas, R. Mayol, and M. Pi, "K-Rb Fermi-Bose mixtures: Vortex states and asag," *Physical Review A* **70**, 043630 (2004).

[157] M. Tasgin, A. Subasi, M. Oktel, and B. Tanatar, "Vortices in trapped boson-fermion mixtures," *Journal of Low Temperature Physics* **138**, 611 (2005).

[158] C. Gies, B. van Zyl, S. Morgan, and D. Hutchinson, "Finite-temperature theory of the trapped two-dimensional Bose gas," *Physical Review A* **69**, 023616 (2004).

[159] B. van Zyl, R. Bhaduri, and J. Sigetich, "Dilute Bose gas in a quasi-two-dimensional trap," *Journal of Physics B-Atomic Molecular and Optical Physics* **35**, 1251 (2002).

[160] M. Holzmann and W. Krauth, "Kosterlitz-Thouless transition of the quasi-two-dimensional trapped Bose gas," *Physical Review Letters* **100**, 190402 (2008).

[161] M. Lee and S. Morgan, "Solutions of the Gross-Pitaevskii equation in two dimensions," *Journal of Physics B-Atomic Molecular and Optical Physics* **35**, 3009 (2002).

[162] C. Gies, M. Lee, and D. Hutchinson, "Many-body T-matrix of a two-dimensional Bose-Einstein condensate within the Hartree-Fock-Bogoliubov formalism," *Journal of Physics B-Atomic Molecular and Optical Physics* **38**, 1797 (2005).

[163] J. Mur-Petit, A. Polls, M. Baldo, and H. Schulze, "Pairing in two-dimensional boson-fermion mixtures," *Physical Review A* **69**, 023606 (2004).

[164] J. Mur-Petit, A. Polls, M. Baldo, and H. Schulze, "Pairing in cold Fermi gases and Fermi-Bose mixtures," *Journal of Physics B-Atomic Molecular and Optical Physics* **37**, S165 (2004).

[165] D. Petrov and G. Shlyapnikov, "Interatomic collisions in a tightly confined Bose gas," *Physical Review A* **64**, 012706 (2001).

[166] S. Ospelkaus, C. Ospelkaus, L. Humbert, K. Sengstock, and K. Bongs, "Tuning of heteronuclear interactions in a degenerate Fermi-Bose mixture," *Physical Review Letters* **97**, 120403 (2006).

[167] C. J. Pethick and H. Smith, *Bose-Einstein Condensation in Dilute Gases*. Cambridge University Press, 1st edition ed., 2002.

[168] Z. Akdeniz, P. Vignolo, P. Capuzzi, and M. P. Tosi, "Boson-fermion demixing and collapse in low dimensions," *Laser Physics* **16**, 1005 (2006).

[169] F. Dalfovo and S. Stringari, "Bosons in anisotropic traps: Ground state and vortices," *Physical Review A* **53**, 2477 (1996).

[170] W. Krauth, "Quantum Monte Carlo calculations for a large number of bosons in a harmonic trap," *Physical Review Letters* **77**, 3695 (1996).

[171] D. Petrov, M. Holzmann, and G. Shlyapnikov, "Bose-Einstein condensation in quasi-2D trapped gases," *Physical Review Letters* **84**, 2551 (2000).